Investigation on Heusler alloys Co_2FeSi and $Co_2FeAl_{0.5}Si_{0.5}$

Nga Tung Chris Yu

PhD

University of York

Physics

March 2017

Abstract

Giant magnetoresistance (GMR), tunnelling magnetoresistance (TMR) and spin-transfer torque (STT) MRAM relies on spin polarisation. Furthermore, exchange coupling is also part of the read/write head in storage devices. Heusler alloys are one of the leading candidate materials not only for having high spin polarisation but also their magnetic properties such as high saturation magnetisation and low Gilbert damping which are all essential for developing memory storage devices. To further investigate this material, its magnetic and structural properties must be fully understood.

The main goal of this study was to increase the design flexibility for Co-based Heusler spintronic devices by understanding the material's properties. By applying a dual Cr/Ag seed layer, the saturation magnetisation and squareness ratio were both found to be increased. It has been found that Cr provides a smooth and flat surface for the following layers which gives rise to good structural ordering of the films. This finding was then applied to an exchange bias system and achieved a loop shift which was five times larger than that reported in a previous study.

Table of Contents

List of Publications

J. Sagar, C. Yu, C. Pelter, J. Wood, L. Lari, A. Hirohata and K. O'Grady, "Effect of Seed Layers on Polycrystalline Co_2FeSi Thin Films", IEEE Transactions on Magnetics, vol. 48, no. 11, pp. 4006-4009, 2012.

J. Sagar, C. N. T. Yu, L. Lari, and A. Hirohata, "Growth of polycrystalline Heusler alloys for spintronic devices," Journal of Physics D: Applied Physics, vol. 47, no. 26, p. 265002, 2014.

L. M. Loong, J. H. Kwon, P. Deorani, C. N. T. Yu, A. Hirohata and H. Yang,
"Investigation of the temperature-dependence of ferromagnetic resonance and spin waves in $Co_2FeAl_{0.5}Si_{0.5}$,"Applied Physics Letters 104, 232409, 2014.

T. F. Alhuwaymel, R. Carpenter, C. N. T. Yu, B. Kuerbanjiang, R. M. Abdullah, V. K. Lazarov, M. El-Gomati and A. Hirohata,
"Direct band-gap measurement on epitaxial $Co_2FeAl_{0.5}Si_{0.5}$ Heusler-alloy films," Journal Applied Physics 117, 17D131, 2015.

C. N. T. Yu. A. J. Vick, N. Inami, K. Ono, W. Frost and A. Hirohata ''Exchange bias induced at a $Co_2FeAl_{0.5}Si_{0.5}$/Cr interface'', Journal of Physics D: Applied Physics, 50, 12, 2017.

List of Abbreviations

ACPWs	Asymmetric coplanar wave guides
AGFM	Alternating gradient force magnetometer
AMR	Anisotropic magnetoresistance
AF	Antiferromagnetic
CGS	Centimetre-gram-seconds
CIP	Current in the plane
CPP	Current perpendicular to the plane
DOS	Density of states
DRAM	Dynamic random access memory
F	Ferromagnetic
FMR	Ferromagnetic resonance
GMR	Giant magnetoresistance
HDD	Hard disk drives
HMF	Half-metallic ferromagnet
HiTUS	High target utilisation sputtering
MBE	Molecular beam epitaxy
MR	Magnetoresistance
MRAM	Magnetic random access memory
MTJ	Magnetic tunnel junction
NM	Non-magnetic
Pd	Palladium
RHEED	Reflection high-energy electron diffraction
RKKY	Ruderman-Kittel-Kasuya-Yosida
SAED	Selected area electron diffraction
TEM	Transmission electron microscopy
TMR	Tunnelling magnetoresistance
UHV	Ultrahigh vacuum
VNA	Vector network analyzer
VSM	Vibrating sample magnetometer
XMCD	Magnetic circular dichroism
XRD	X-ray diffraction

List of symbols

μ_B/f.u.	Bohr magneton / formula unit
α	Gilbert damping coefficient
a	Lattice constant
E_F	Fermi level
E_g	Band-gap
e_g	Degenerate antibonding states
H	Magnetic field
h	Planck's constant
H_c	Coercivity
$k_B T$	Thermal stability
m	Magnetic moment
M	Magnetisation
M_s	Saturation magnetisation
M_t	Magnetic moment
$N\uparrow$ ($N\downarrow$)	Densities of the majority and (minority) electrons
P	Spin polarisation
R	Resistance
R_{max}	Maximum resistance
R_{min}	Minimum resistance
t_{2g}	Degenerate bonding states
T_C	Curie temperature
Z_t	Valence electrons
ϕ_m	Magnetic flux

List of Figures

Acknowledgements

I would like to thank all who have contributed in a way or another to this thesis.

In particular, I would first like to acknowledge my supervisors Prof. K. O'Grady and Prof. A. Hirohata for giving me the opportunity to work on this project. Without their guidance, continued support and excellent humour the last five years would have not have been possible. And this thesis would not be possible without their insight in Physics and careful proof-reading of this thesis.

During this PhD I was very fortunate to visit the laboratory in Hong Kong University. I would like to thank Dr Philip Pong for allowing me access to the laboratory and Dr Mitch Li for giving help in the lab.

I would also like to thank Dr. Balati Kuerbanjiang and Dr. Jame Sagar from University of York for generating transmission electron microscopy images on this collaborated work. And Dr. Loong Li Ming from University of Singapore for carried out ferromagnetic resonance measurements.

I also wish to thank the staff in the workshops in the Electronics and Physics Departments especially Mr. Dave Coulthard and Mr. Andy White.

I have to thank all of the students and visitors to SO20/A012, past and present, for all of your kindness and joyfulness. There are too many people to name but I must give special mentions to Rob Carpenter, Ben Murphy and Kelvin Elphick for being such good friends.

Most of all I want to thank my parents who have continuously giving me their support, patient and encouragement throughout these years. It was them whom continuously show me the right path to walk on and keep going.

Thank you very much.

Declaration

I declare that the work presented in this thesis is based purely on my own research, unless otherwise stated, and has not been submitted for a degree in either this or any other university. Some of the research presented in this thesis has resulted in the following publications:

C.N.T. Yu. A. J. Vick, N. Inami, K. Ono, W. Frost and A. Hirohata ''Exchange bias induced at a $Co_2FeAl_{0.5}Si_{0.5}$/Cr interface'', Journal of Physics D: Applied Physics, 50, 12, 2017.

Signed

Nga Tung Chris Yu
2017

Chapter 1

Introduction

1.1 Spintronics

Information processing devices and information storage devices are based on semiconductor and/or magnetic materials respectively. The origins of these devices are based on manipulating the motion of electric charges and controlling the orientation of the magnetic moments respectively. Figure 1.1 demonstrates the difference between charge current and spin current. The electron charge is the origin of electricity and the electron spin is the main origin of magnetism. Both flow of charge and the movement of spin can carry information between devices but unlike the flow of charge, the movement of spin can be manipulated easily by applying an external magnetic field. The spin current is one of the building blocks of spintronics. There are many advantages of using spintronics over conventional electronics such as less power consumption, higher transfer speed and more compact in size.

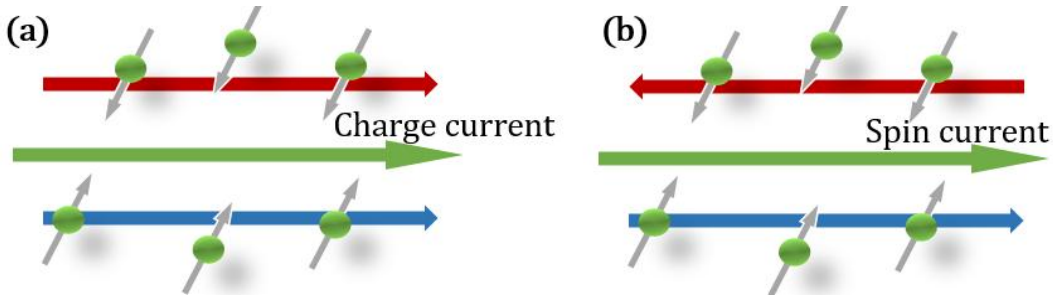

Figure 1.1 (a) Electric current: equal number of up- and down- spin electrons; (b) Spin current: counter flow of up- and down- spins.

Moore's Law states that the number of transistors on a single chip would double every 1.5 years [1]. However, we are approaching the physical limit. Spintronic devices utilise the intrinsic magnetic moment of the electrons due to their spin. In order to utilise this phenomena and introduce it to applications, a current of spin polarised electrons is needed. The current read heads in hard disk technology are based on either tunnelling magnetoresistance (TMR) or giant magnetoresistance (GMR) structures. GMR read heads were first introduced to the

hard disk industry in the late 1980s [2, 3]. A schematic diagram of a GMR structure is shown in Figure 1.2, two ferromagnetic (F) layers are sandwiched with a non-magnetic (NM) material layer. By aligning or anti-aligning the magnetisation of the two F layers low resistance or high resistance states can be manipulated. The current highest intrinsic magnetoresistance (MR) ratio at room temperature is 82% and 285% at 10K for a $Co_2FeGa_{0.5}Ge_{0.5}$ /Ag/$Co_2Fe\ Ga_{0.5}Ge_{0.5}$ pseudo spin-valve [4].

The structure of TMR is similar to that of GMR, where the NM layer is replaced by an insulator. TMR was first discovered by Julliere in 1975 [5] using an amorphous insulating layer with a 14% of resistance change at 4.2K, which is also called a tunnel barrier. The first TMR ratio measurement at room temperature was taken in the early 1990s by Miyazaki [6]. GMR and TMR are discussed in more detail in chapter 2.

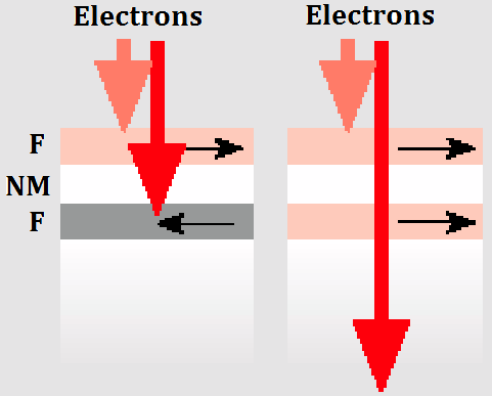

Figure 1.2 A schematic diagram of a GMR structure.

Since it is the electron spin which carries information in spintronic devices, the spin polarisation of the current and spin scattering are very important for improving the efficiency of the TMR devices. Half-metallic ferromagnets (HMF) have been a field of significant research interest in developing spintronic devices due to their unique band structure which are expected to generate 100% spin polarisation which was reported by Galanakis et *al.* in 2002 [7]. Among all HMFs, Co-based Heusler alloys have been attracting great interest due to a large TMR (35%) observed at room temperature in a 1 kore magnetic field using a $Co_2Fe_{0.4}Cr_{0.6}Al$ electrode in magnetic tunnel junctions (MTJs) [8].

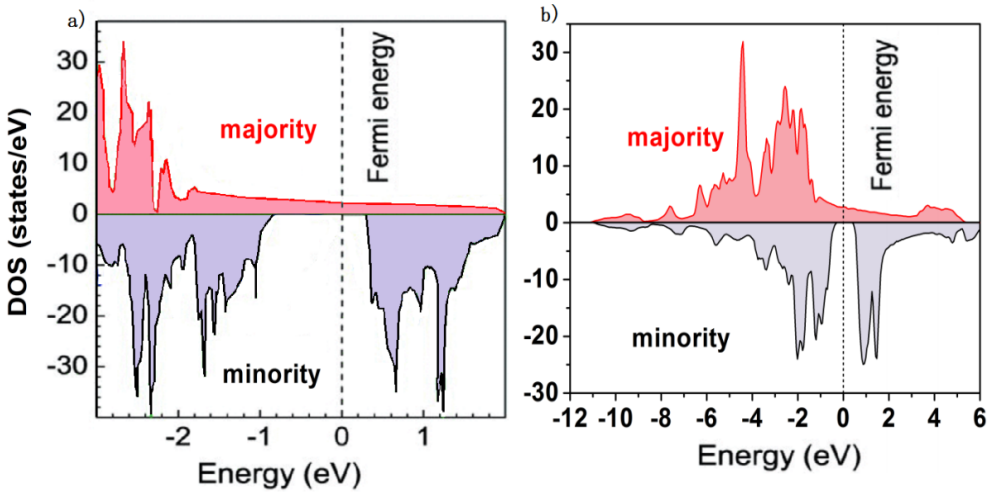

Figure 1.3 Density of states of a) Co_2FeSi and b) $Co_2FeAl_{0.5}Si_{0.5}$. [7].

Co-based Heusler alloy of Co_2FeSi and $Co_2FeAl_{0.5}Si_{0.5}$ were chosen in this study. The electronic structures of the $Co_2FeAl_{0.5}Si_{0.5}$ alloys were calculated and reported by Fecher and Felser in 2007 by using *ab-initio* calculations as shown in Figure 1.3 [7]. It was shown that the Fermi level lies at the centre of the minority band for $Co_2FeAl_{0.5}Si_{0.5}$ while the Fermi level of Co_2FeSi is near the edge of the conduction band gap. Fecher and Felser reported that alloys with a Fermi level near the edge of the conduction or valence bands can lead to unstable electronic properties and an unstable lattice structure with increased temperature. For alloys with the Fermi level (E_F) at the centre of the gap, their half-metallic properties may be robust with increased temperature [9]. $Co_2FeAl_{0.5}Si_{0.5}$ was first introduced in current perpendicular to plane (CPP)-GMR in 2008 by Furubayashi *et al.* with a Ag under-layer [10]. The Ag under-layer is investigated as a seed layer with Cr in this study using high target utilisation sputtering (HiTUS) to grow the films and an alternating gradient force magnetometer (AGFM) to measure the magnetic properties. The Cr/Ag dual seed layer is then introduced to $Co_2FeAl_{0.5}Si_{0.5}$/Cr multilayer structures for further investigation on exchange coupling by using molecular beam epitaxy (MBE) to grow the sample and a vibrating sample magnetometer (VSM) to measure the magnetic properties.

1.2 Magnetoresistance

MR was first discovered by W. Thomson in 1857 [11]. He observed the ferromagnetic material resistivity changes while the direction of its magnetisation

with respect to that of the current flow changes which is known as the anisotropic magnetoresistance (AMR) effect [11]. Following the discovery of AMR, GMR was discovered in 1988 by Grünberg and Fert through an electrical magneto-transport measurement on Fe/Cr/Fe structure where Fe is the ferromagnetic material and Cr is the NM material [2, 12, 13]. An MR ratio of ~15% was observed [13] which is much larger than that in an AMR film of 2.5% at room temperature [11]. The GMR effect has attracted much attention since then and has been observed in various structures such as CIP-GMR and CPP-GMR.

When the NM layer is replaced by a non-metallic layer between the two F layers, the phenomenon which can be observed is known as TMR. Although a TMR effect with ratio of 14% at 4K was observed in 1975 by Julliere [5], it did not attract much attention until late the 90s when this effect was able to be observed at room temperature [6]. The largest difference between GMR and TMR is that TMR not only depends on the spin scattering but depends primarily on the availability of conduction states for tunnelling. TMR ratio has now been found to exceed 600% [14] at room temperature which can be applied to read heads in HDD products.

All MR structures essentially display the same characteristic of changing their electrical resistance with respect to an external field. Since the different mechanisms govern the resistance change, certain MR structures exhibit higher sensitivity than others enabling them to be candidates for device applications. MR is mostly used in the field of magnetic recording, where TMR sensors are used as magnetic read heads and storage devices [15]. The impact that GMR has on society resulted in A. Fert and P. Grünberg winning the Nobel Prize in Physics in 2007 for their discovery of giant magnetoresistance. Detailed discussion of MR can be found in chapter 2.

1.3 Exchange Interaction

A wide range of magnetic properties were investigated in this study. In order to explain these properties, it is important to understand the physical principles. Exchange interactions are essential to antiferromagnetic (AF) coupling. Since the structure of Fe/Cr/Fe AF coupling was first observed by Grünberg *et al.* in 1986 [16], interlayer exchange interaction with either non-magnetic, non-metallic or metal spacer sandwiched with ferromagnetic layers has been a subject of intense research.

Two main interlayer exchange interactions are discussed in this study which are direct exchange and indirect exchange which is also known as Ruderman and Kittel [17], Kasuya [18] and Yosida [19] (RKKY) interaction.

Direct exchange occurs when the neighbouring moments are close enough to have overlapping wave functions, where the atoms can exchange electrons in this overlapping region [20]. The RKKY interaction occurs when moments are at a distance where there is little or no direct overlap between neighbouring electrons [17, 18, 19]. A detailed discussion of exchange interactions can be found in Chapter 3.

1.4 Heusler Alloy

Heusler alloy compositions of XYZ and X_2YZ, where X and Y are transition metals and Z is a main group element, have over 2000 known compositions and can be semi-conductors, ferromagnets, shape memory alloys, etc. The X_2YZ Heusler alloy compositions have been known for more than a hundred of years, yet still attract great interest because of their diverse magnetic properties, *i.e.*, ferromagnetism, antiferromagnetism, localised magnetism, etc. Their half metallic properties make them a potential candidate for spintronic device applications.

The efficiency of spintronic devices depends on the spin polarisation (P) and it is defined as,

$$\mathrm{P} = \frac{N_{\uparrow}(E_{\mathrm{F}}) - N_{\downarrow}(E_F)}{N_{\uparrow}(E_{\mathrm{F}}) + N_{\downarrow}(E_{\mathrm{F}})} \tag{1.1}$$

where $N_{\uparrow}$ and $N_{\downarrow}$ are the densities of the majority and minority electrons at the E_{F} respectively. As predicted by *ab-initio* calculations many X_2YZ compositions exhibit a 100% spin polarisation at the Fermi level [7]. The majority spin band exhibits metallic behaviour and the minority band exhibits semiconducting behaviour which can be seen in the schematic density of states curve as shown in Figure 1.4. The band structure and electronic properties of the Heusler alloy material are discussed in chapter 3.

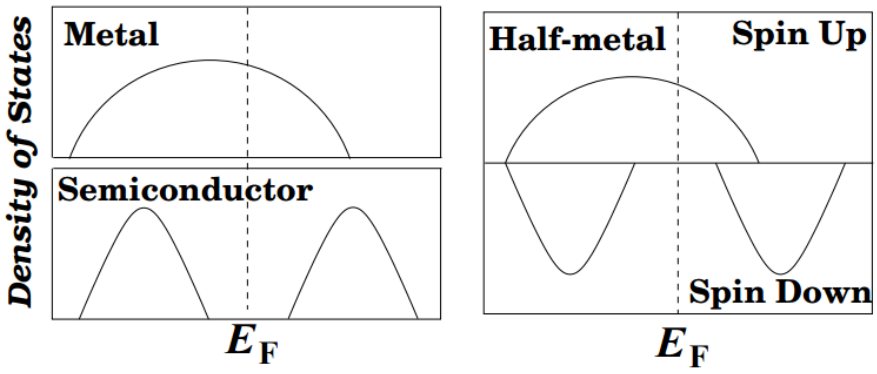

Figure 1.4 A schematic diagram of the density of states of metal and half metal.

In addition to the predicted 100% spin polarisation, a high Curie temperature (T_c) up to 1100K [21] is another attractive physical property which would allow devices to be operated above room temperature. The Heusler alloy with the highest T_c is from the Co-based alloys group with Y being a transition metal and Z an element from the III-V groups. This group of Heusler alloys ideally crystallises with a $L2_1$ structure. The atomic order of the material has a significant impact on the properties of the Heusler alloy and the three types of crystal structures are the ordered structure ($L2_1$) and disordered structures, $B2$ and $A2$ which are as shown in Figure 1.5. All properties and crystal structures of the selected Heusler alloy are discussed in chapter 3.

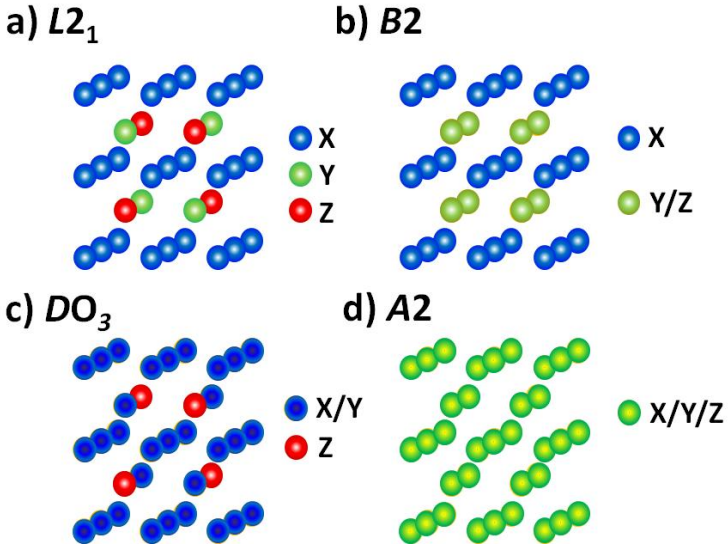

Figure 1.5 Types of disorder in Heusler alloy structure [22].

1.5 Aim of This Study

The aim of this study is to conduct a systematic study of the structural and magnetic properties in a multilayer structure consisting of the $Co_2FeAl_{0.5}Si_{0.5}$ Heusler alloy grown epitaxially on MgO(001) and to investigate the exchange bias for the designed multilayered structure. For this purpose, studies of thin films consisting $Co_2FeAl_{0.5}Si_{0.5}$ layers are carried out by X-ray diffraction (XRD), X-ray magnetic circular dichroism (XMCD), transmission electron microscopy (TEM), AGFM and VSM. By introducing a dual seed layer, varying film thickness, annealing temperature and time, the film structural and magnetic properties can be optimised. The investigations are performed with the aim of revealing the dependence of thickness of the F layer and AF layer on both the structural and magnetic properties of the Heusler alloy.

1.6 Units and Errors

In this study, the centimetre-gram-seconds (cgs) unit system has been used as it is the unit system which is used by the magnetic recording society. Where possible the numerical data in graphs and tables is quoted with its error. These errors have been calculated using standard Gaussian error techniques [23], unless otherwise stated in the following text. Values quoted from the literature which are without error, as these errors are unknown.

Chapter 2

Background Concepts

2.1 Spin Transport

In the early 1920s, Stern and Garlach discovered silver atoms have spin angular momentum which is the first time that the electron's spin nature was revealed [24]. The spin quantum number (s) of electrons is

$$s = \frac{1}{2} \tag{2.1}$$

and the projection of the electron spin for up and down states are

$$s_z = +\frac{1}{2} \quad or \quad s_z = -\frac{1}{2} \tag{2.2}$$

where z is a chosen quantisation axis $+\frac{1}{2}$ and $-\frac{1}{2}$ are representing electron spin up and spin down state respectively [25].

The importance of 'spin' in magnetism was not revealed until the 1930s. In 1936, Mott and Jones revealed the importance of controlling electron spin transport in their two-current model from which the schematic diagram is shown in Figure 2.1 [26]. Their model was then applied into current perpendicular to plane GMR (CPP-GMR) by Valet and Fert in 1993 [27].

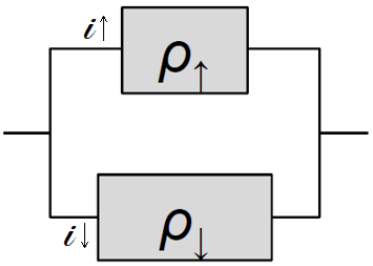

Figure 2.1 Mott and Jones's two-current model considers electron conduction in ferromagnetic transition metals as a parallel circuit with resistivity from two types of carriers (spin-up and spin-down). [27].

The two-current model is still the basis of spintronics today. Spintronic device applications demand high P, high T_c and high magnetisation saturation (M_s). The spin polarisation of the current of a material at the Fermi level is defined as

$$P = \frac{N_\uparrow - N_\downarrow}{N_\uparrow + N_\downarrow} \tag{2.3}$$

where $N_\uparrow$ and $N_\downarrow$ are the numbers of the up (majority band) and down (minority band) spin electrons at E_F respectively [5]. Elementary ferromagnetic transition metals are also called *3d* metals as their *3d* orbital are unfilled which is essential for spin generation. This imbalance of spin originates from the spin split density of states of the 3d bands at E_F. This spin split density of states is induced by the exchange interactions between electron spins [22, 28]. Therefore, in a F material such as Co, the spin up and spin down electrons at E_F are not balanced. This imbalance band leads to a magnetic moment (m) in the F material [22],

$$m = \mu_B(N_\uparrow - N_\downarrow) \tag{2.4}$$

where μ_B is the Bohr magneton.

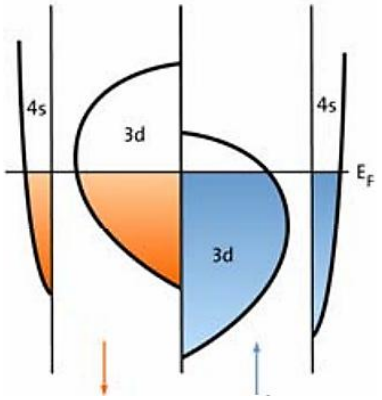

Figure 2.2 Schematic diagram of density of state of a ferromagnetic material [22].

The density of states of the ferromagnetic materials which is relevant for Co and Fe is shown in Figure 2.2. This unique character is the key of the GMR effect which is discussed in the next section.

2.2 Magnetoresistance

Magnetoresistance (MR) refers to the change in electrical resistance, ΔR of a material when a magnetic field is applied. The MR ratio is defined as,

$$\mathrm{MR} = \frac{\mathrm{R(B)-R(0)}}{\mathrm{R(0)}} \times 100\% \tag{2.5}$$

where $R(B)$ is the resistance at magnetic field B and $R(0)$ the resistance at zero field. A material that has a larger resistance in the presence of a field is defined as having a positive MR, whereas if the field reduces the resistance, the MR is negative. MR materials are incorporated in a number of commercially available technologies such as magnetic recording (read heads) and magnetic memories (MRAM).

2.2.1 Giant Magnetoresistance (GMR)

GMR was observed in multilayers consisting of F and NM metals in 1988 by Grünberg *et al.* and Fert *et al.* [16, 27]. GMR depends on the relative orientation of the magnetic moments of the F layers. The resistance of a GMR device can be simply understood by consideration of Figure 2.3. The resistance is largest when the magnetic moments of the two ferromagnetic layers F1 and F2 are oppositely aligned and the resistance is smallest when an external field forced F1 and F2 to align parallel. There are two GMR geometries where the current flows either in the plane (CIP) of the film or perpendicular to it (CPP). Although they have different geometries the underlying physical mechanism is the same.

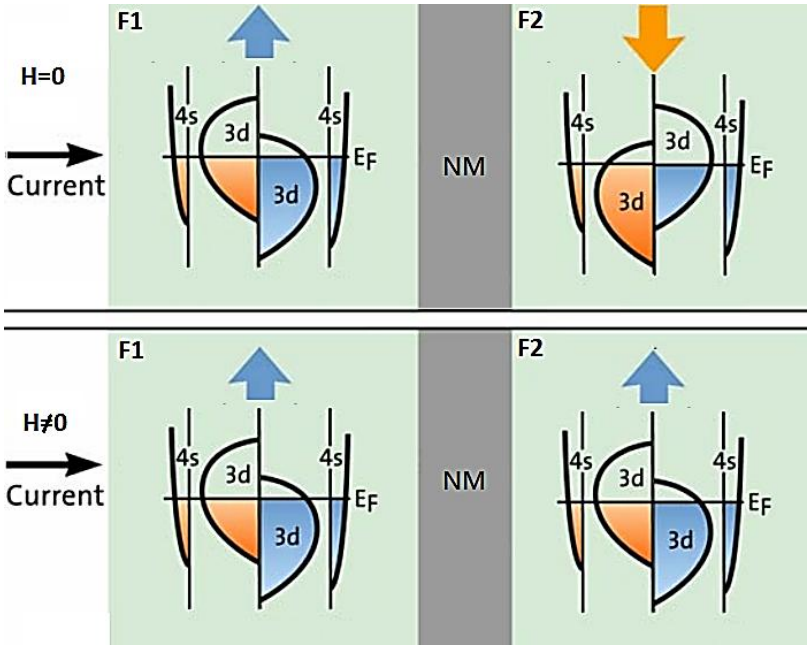

Figure 2.3 Illustration of a trilayer, F/NM/F, GMR system [27].

2.2.1.1 Current in-the-plane GMR

A GMR structure consists of two F layers separates by a NM layer with both magnetic configurations, CIP and CPP, as shown in Figure 2.4. Electron scattering occurs at the interface of F/NM layers. The NM layer provides a coupling mechanism between the F layers and this interlayer exchange coupling mechanism is discussed in detail in section 2.5.

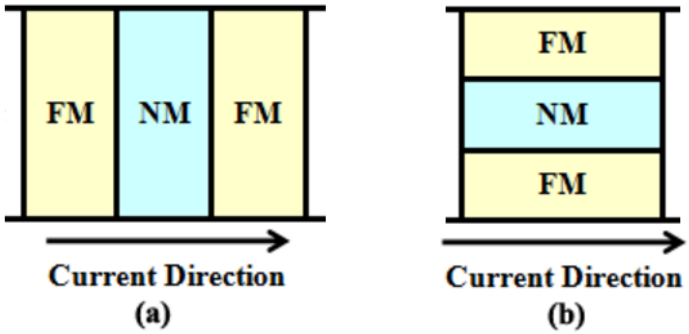

Figure 2.4 Schematic diagrams of (a) CPP and (b) CIP GMR [20].

The first GMR sensor with a spin-valve structure used in HDD read heads was commercialised by IBM in 1997 [29]. However, CIP-GMR has a size limitation which cannot satisfy the demand of downscaling of hard disk drive (HDD) read heads. CIP GMR sensor has a planer geometry which is the main reason that limits downscaling of the HDD read heads. And the other reason is that CPP-GMR gives a larger value than that of CIP-GMR. Therefore, the CPP-GMR structure has been introduced which is discussed in more detail in the next section. By applying a sensing current in two different directions as shown in Figure 2.5, both CIP-GMR and CPP-GMR can be detected. In the CIP configuration, a sensing current is applied parallel to the surface layer [30].

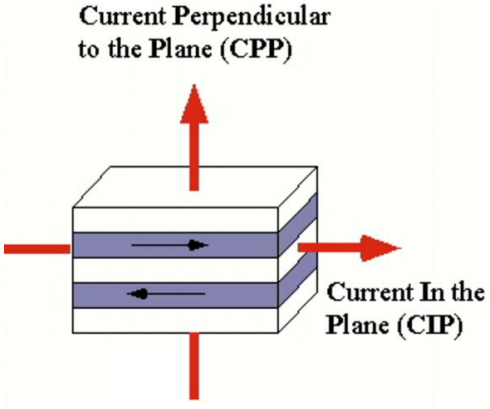

Figure 2.5 The red arrows representing the sensing current flow direction [7].

The scattering rate of electrons in ferromagnetic materials depends on the spin direction, and results in different resistivities $\rho\uparrow$ and $\rho\downarrow$ [31]. By assuming there is no spin mixing between the up and down spins in the F/NM multilayer, the total resistivity of the F/NM multilayer in the parallel magnetisation state (ρ_P) is

$$\rho_P = \left(\frac{1}{\rho_\uparrow} + \frac{1}{\rho_\downarrow}\right)^{-1} \tag{2.6}$$

In the antiparallel magnetisation state, electrons with one spin direction (up or down) are scattered as the majority and minority electrons alternately in the multilayer. Therefore, the multilayer shows different resistances between the P and AP states. This theory on spin scattering can be used in both scattering in the bulk of the ferromagnetic layer and at the interface between the ferromagnetic and nonmagnetic layers.

However, the origin of CIP-GMR is believed to be mainly the spin-dependent scattering at the F/N interface rather than that in the bulk of the F layers which is supported by the experimental evidence reported by Parkin at 1993 [12]. He fabricated spin-valves with NiFe/Cu/NiFe and Co/Cu/Co sandwiches and studied the effect of insertions of very thin Co or NiFe layers at the NiFe/Cu or Co/Cu interfaces, respectively. The results clearly indicate that the bulk scattering of the NiFe layers and of the inserted Co layer do not contribute significants to GMR, and that the enhancement of GMR is due to the larger interfacial scattering at Co/Cu than that at NiFe/Cu [12].

2.2.1.2 Current-perpendicular-to-plane GMR

Therefore, the origin of CIP-GMR is mostly contributed to the spin-dependent scattering at the F/NM interface. On the other hand, the origin of CPP-GMR is the spin accumulation at the F/NM interface. CPP-GMR is the basis of GMR devices. The resistivity for parallel and antiparallel CPP-GMR is given by

$$\rho_P = \frac{2(\rho_\uparrow \rho_\downarrow)}{\rho_\uparrow + \rho_\downarrow} \tag{2.9}$$

$$\rho_{AP} = \frac{(\rho_\uparrow + \rho_\downarrow)}{2} \tag{2.10}$$

And the GMR ratio is given by

$$GMR = \frac{\Delta R}{R_P} = \frac{R_{AP} - R_P}{R_P} \tag{2.11}$$

The biggest advantage of CPP-GMR is that the output of CPP-GMR is intrinsically larger than that of CIP-GMR at room temperature which has been proved by Bass *et al.* and Holody *et al.* [32, 33]. This is mostly because there is no shunting of the current through NM layers in CPP geometry and all the current undergoes spin scattering at every interface to traverse the layered structure.

2.2.2 Tunnelling Magnetoresistance

The TMR effect can be observed in a MTJ. An MTJ consists of two ferromagnets separated by a tunnel barrier and changes its resistance depending on the relative orientation of the two magnetization directions of the two magnets due to spin-dependent tunnelling involved in the transport between the majority and minority spin states. This resistance change is called TMR. The difference between GMR and TMR is that the NM layer is replaced by an insulator layer which is a few atomic layers thick.

In 2001 a crystalline junction with a MgO barrier was proposed by Butler, it was predicted that the TMR ratio would reach 1000% [34]. Three years later in 2004 Parkin and Yuasa experimentally observed a TMR ratio of 250% in the Fe/MgO/Fe tunnelling junction [35, 36]. To date, the TMR ratio has been reported in Co/MgO/Co (410%) [37], CoFe/MgO/CoFe (290%) [36] and CoFeB/MgO/CoFeB (1144% at low temperature and 604% at RT) [38] in MTJs with the current perpendicular to plane. MTJs can be used as non-volatile magnetic random access memories (MRAMs) and are used in all read heads for HDD [39].

2.3 Exchange Interactions

Both Co_2FeSi and $Co_2FeAl_{0.5}Si_{0.5}$ are ferromagnets. To understand the ferromagnetism in Heusler alloys, fundamental exchange interactions have to be investigated. The ferromagnetism of Co_2MnSi originates from the Mn atoms and the ferromagnetic coupling between the Co and Mn moments [40, 41]. There are no

detailed studies of exchange interactions reported in the literature for the Heusler alloys Co_2FeSi and $Co_2FeAl_{0.5}Si_{0.5}$. However, these materials are expected to exhibit the same mechanisms due to their similar structural and electronic properties [42].

Exchange interactions determine the magnetism of the material, *i.e.*, ferromagnetic or antiferromagnetic. Furthermore, since exchange bias is a phenomenon of the exchange interaction, it is essential to understand the mechanism of exchange interactions in Heulser alloys. Two mechanisms, direct exchange and indirect exchange interactions are introduced in the following sections.

2.3.1 Direct Exchange

Magnetic moments in X_2YZ Heusler alloys are mainly derived from the Y or the X and Y atoms. Direct exchange interaction occurs in the X and Y atoms or indirect exchange interactions occurs between Y atoms. The origin of the direct exchange interaction arises from the spins of the electrons associated with neighbouring atoms which interact when their quantum mechanical wave functions overlap. Thus the atoms in the overlapped region can exchange electrons and the energy associated with this exchange is

$$E_{ex} = -2J_{ex}S_iS_j \tag{2.12}$$

where J_{ex} is the exchange integral, S_i and S_j are the spin angular momentum vectors of two atoms i and j respectively. The alignment of spins is described by the sign of J_{ex}, which can be explained by the Bethe-Slater curve as shown in Figure 2.6. When J_{ex} is negative, antiparallel alignment occurs (antiferromagnetic) whilst a positive value gives parallel alignment (ferromagnetic) [20].

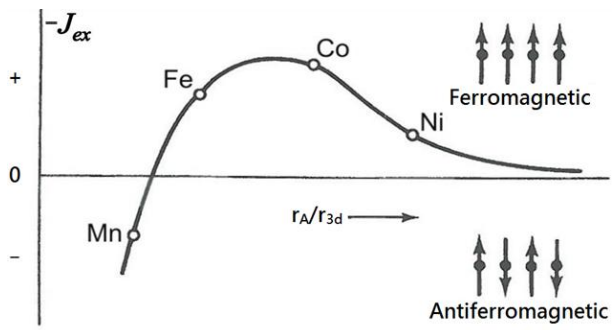

Figure 2.6 A Bethe-Slater curve [20].

Therefore, according to Figure 2.6, the value of J_{ex} of Co, Ni and Fe are positive. Hence, the spins for Co, Ni and Fe are held in parallel alignment which exhibit ferromagnetism. This means that Co, Ni and Fe are coupled ferromagnetically to each other by direct exchange coupling.

2.3.2 RKKY Interaction

The indirect exchange interaction is also known as the RKKY interaction [17, 18, 19] which is an oscillating and long range indirect exchange interaction. This mechanism has been used to explain magnetic phenomena such as coupling between rare-earth metals and other alloys, inter-granular exchange coupling in polycrystalline thin films and coupling between separated magnetic layers. In this case, it is responsible for the exchange coupling in the multilayer structure of $Co_2FeAl_{0.5}Si_{0.5}$ and Cr system discussed in chapter 5.

The origin of this mechanism is that the local magnetic moment polarises the conduction electrons of the material which can then align nearby moments across grain boundaries in solid materials and interlayers in stacks. An oscillatory behaviour of the exchange integral (J_{ex}) occurs when the up- and down-spin electrons align to the neighbouring electron. This oscillatory behaviour depends on the separation between the atoms or localised moments in the F/AF layered system and thus J_{ex} oscillates between positive and negative values as shown in Figure 2.7.

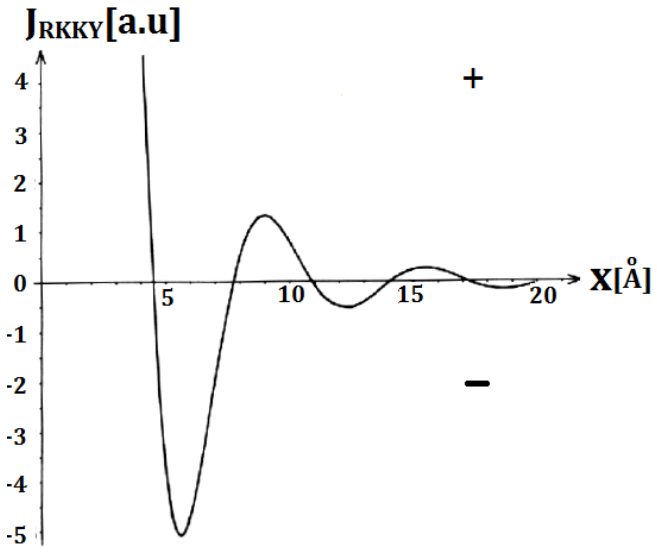

Figure 2.7 A modified RKKY exchange energy plotted as a function of the interatomic distance [43].

There were several studies on Fe/Cr and Co/Cr layers system just before the 21st century. The first single crystal multilayer structure containing Fe layer coupled through >20 Å Cr layer was reported in 1988 by Baibich *et*. al., however no oscillatory coupling was shown [44]. Not long after that, Pescia *et*. al. investigated Co/Cu/Co single crystal multilayer structures, it was shown that the Co layer separated by Cu layer was coupled via an oscillatory interaction of the RKKY-type [45].

The first oscillatory magnetic exchange coupling in sputtered polycrystalline film was first reported by Parkin *et*. al. in 1990 [46]. Three different metallic superlattices of F/NM layers samples were investigated: Fe/Cr, Co/Ru and Co/Cr. Figure 2. 8 shows the dependence of the saturation magnetoresistance and the saturation field on the thickness of the Ru layer. It was found that Co/Cr exhibits similar behaviour to Co/Ru with a larger oscillation period of ~21 Å but with smaller values of $\Delta R/R$ and H_S. It was shown that all three samples exhibit similar oscillatory magnetic exchange coupling which suggests that it is a common phenomenon of such F/NM layers system. Furthermore, it was found that the coupling extends to a range of about 4 nm so that the coupling can occur across grain boundaries making the RKKY interaction particularly important in granular thin films [46].

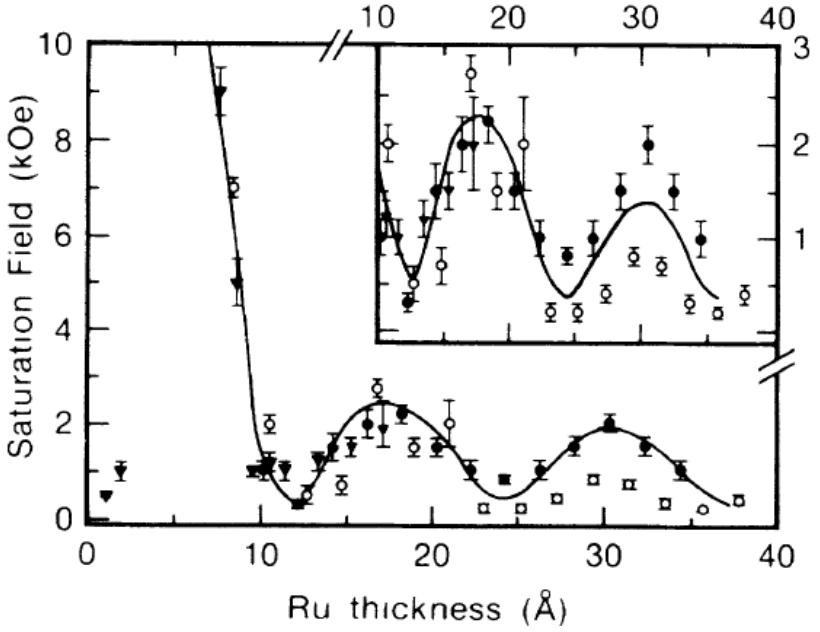

Figure 2. 8 Saturation field versus thickness of Ru layer deposited at temperatures of ⧫ 40 °C, ⧲ 125 °C and × 200 °C [46].

2.4 Magnetic Domains

The origin of magnetic domains is the minimisation of the magnetostatic energy (E_{ms}) and it is associated with the existence of the demagnetising field of the material. E_{ms} is given by [20]

$$E_{ms} = \frac{1}{8\pi}\int H_D^2\, dV \tag{2.17}$$

where H_D is the demagnetising field which depends on the orientation of the domain and its shape and V is the volume. However, for a long cylinder like shape, $H_D = -4\pi M_s$ and equation (2.17) becomes

$$E_{ms} = \frac{1}{2} N_D M_s^2 \tag{2.18}$$

where N_D is the shape demagnetising factor and M_s is the saturation magnetisation. For a single cubic crystal where N_D is $4\pi/3$ equation (2.18) becomes

$$E_{ms} = \frac{2}{3}\pi l M_s^2 \tag{2.19}$$

where l is the length of the domain. When there is no external applied field, the magnetic moments in each domain align parallel to each other with preferential directions set by the magnetic anisotropy. There are several domain patterns due to different properties of ferromagnetic material shown in Figure 2.9. E_{ms} can be reduced by splitting a single domain into several domains as shown in Figure 2.9. However the domains cannot split indefinitely due to the energy associated with the domain walls. Domain walls are transition regions which separate the domains. There are two types of domain walls: Bloch wall and Néel wall which are discussed in more detail in the next section.

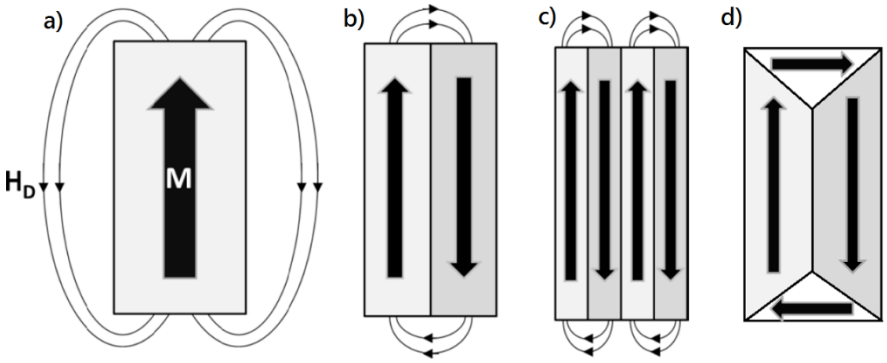

Figure 2.9 Examples of domain patterns (a) uniformly magnetised single domain, (b) two domains, (c) four domains and (d) four domains in a Landau state [20].

2.4.1 Domain Wall

Bloch walls are usually observed in bulk materials or thick films, and Néel walls occur in thin films. Figure 2.9 (b) and (c) show 180° Bloch walls and Figure 2.9 (d) shows 90° and 180° Bloch walls. As shown in Figure 2.10 (a), Bloch walls are simply transition region for magnetic moments to orientate their directions in thick films. When Bloch walls occur in thin films, they create free poles at the film surface which leads to the creation of a large magnetostatic energy. In this case the magnetic moments rotate in-plane so that no free poles are created at the film surface as shown in Figure 2.10 (b).

The width of the domain walls is determined by competition between the exchange interaction between the spins within the wall and the anisotropy of the system. The domain wall energy (E_{wall}) per unit area of a cubic crystal is

$$E_{wall} = \frac{D_w}{l}\sigma_w \tag{2.20}$$

where σ_w is the domain wall energy per unit area and D_w is the wall width [20].

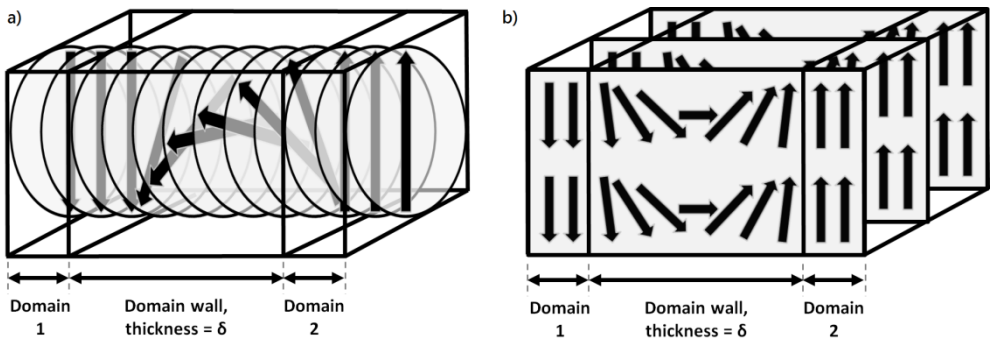

Figure 2.10 Schematic diagrams of a) Bloch and b) Néel domain walls [20].

In Néel walls in a thin film as shown in Figure 2.10 (b) the moments rotate in the plane of the film, resulting in a lower energy. Therefore, in thin films the magnetisation is generally in plane because the magnetostatic energy is much lower. Néel walls do not occur in bulk specimens because they generate higher magnetostatic energy than that in a thin film [20].

2.4.2 Magnetisation Curves

A magnetisation curve or hysteresis loop expresses the response of a magnetic material to an external magnetic field. An example of typical hysteresis loops for a Heusler alloy thin film are shown in Figure 2.11. A hysteresis loop is characterised by the saturation magnetisation (M_S), the remanence (M_r) and the coercivity (H_C). H_C strongly depends on the detail of the reversal mechanism. If a uniform rotation of the magnetisation occurs, as is assumed in the Stoner-Wohlfarth model [20], H_C is equal to the anisotropy field. The nucleation of domains plays an important role in the magnetisation reversal process particularly in Heusler alloy films and the coercivity is smaller than the anisotropy field either by domain wall motion or domain rotation. When the external field is large enough to saturate the material, the domains align with the direction of the field. For domain walls, defects act as pinning centres which increases the stability of the domain walls against externally applied fields. This results in higher values of H_c.

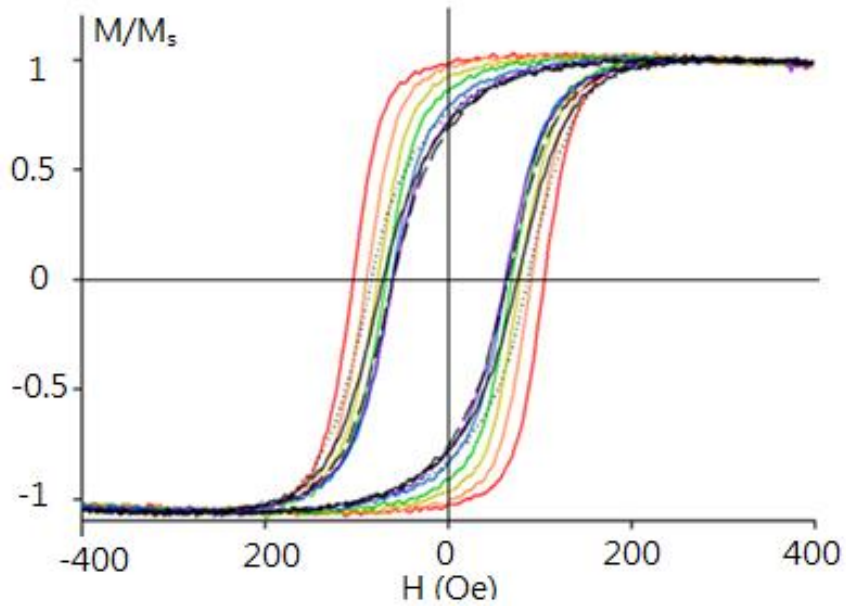

Figure 2.11 Typical hysteresis loops for Co_2FeSi with respect to 0°-90° of the easy axis.

In Figure 2.11, different squareness of hysteresis loops are presented. The squareness of a hysteresis loop depends on the pinning of the domain walls. This domain wall motion is further discussed in section 2.5.

2.5 Magnetisation Reversal in Magnetic Thin Films

Magnetisation reversal in a magnetic thin film depends on the structure of the sample. Magnetisation reversal can also depend on the use of seed layer(s) and multiple magnetic layers. All three types of structures have been grown and measured in this work.

For the case of single crystal films, reversal proceeds by domain wall motion which is impeded by domain wall pins arising from defects and impurities in the films and the effect of non-uniformities on the surface of the substrate e.g. atomic steps. In the case of reversal from the saturated state, some degree of nucleation of reverse domains is controlled by the anisotropy of the film. Therefore the anisotropy of the film also influences the process.

Generally, nucleation is driven by the applied field and thermal activation. The demagnetising field (H_D) can also contribute to the magnetostatic energy. In the plane of a thin film the demagnetising factor is zero and the effect of the demagnetising field can only occur at the edges of the sample particularly at the corners of a square sample or defects, eg. substrate asperities.

For the case of polycrystalline films, two situations arise. The first is where the grain size is larger than the critical size for single domain behaviour. There is a domain structure within each grain. Due to RKKY interactions, the local magnetic moment can align nearby moments even across grain boundaries leading to multi-grain domains. However there will be domain wall pinning especially when there are impurities at grain boundaries.

However in most thin films studied in this work, the grain sizes are less than 40 nm and generally have a mean value between 10 and 20 nm such that grains are almost certainly single domain. Hence the magnetic anisotropy plays a significant role in reversal. However, the films are very dense typically >90% of the bulk value. Hence significant inter-granular RKKY coupling occurs leading to domain wall processes.

In the case of superlattice films, the above processes also occur. Of course with many interfaces the possibility of increased pinning occurs. However, there is now also the possibility of interlayer exchange interaction in the RKKY mechanism which depends on the thickness of the interlayer [44].

2.5.1 Single Crystal Thin Films

Single crystal films rely on the use of single crystal substrates for their preparation. When all conditions are correctly set, the magnetic film grows on the substrate epitaxially with one or a series of very large crystallites with very slight or no disorientation or imperfections.

The formation of domains during magnetization reversal is the outcome of a competition of the exchange, anisotropy, magnetostatic and Zeeman energies. The reversal mechanism in the single crystal films in this study is domain formation. Domain forms as discussed in session 2.4. Domain formations may be expected until the energy required to establish a domain wall is greater than the reduction in magnetostatic energy in the entire domain pattern.

In the case of reversal process, it is usually initiated by nucleation of a reverse domain by coherent rotation as in the case of Stoner-Wohlfarth model, until switching or multiple switching processes occur which is triggered by domain nucleation. Due to the exchange coupling, domain wall motion is now very rapid leading to a square loop unless there is significant substrate roughness giving significant domain wall pinning.

2.5.2 Polycrystalline Thin Films

Most of the thin films studied in this work have a thickness of < 10nm, and have a cubic structure and hence cubic anisotropy. Reversal in single domain particles with cubic anisotropy is highly complex due to the multiplicity of easy axes. The magnetisation process at T=0 was first described by Joffe and Henberger in 1974 [47] and a more comprehensive model including a particle size distribution and the effects of thermal activation was provided by Walker et al. [48]. However in practice cubic anisotropy is very weak typically $\sim 10^5$ emu/cm^3 so that in real systems and in particular metallic polycrystalline films, the irregular shape of the grains leads to dominant shape anisotropy for an axial ratio of $>10\%$ giving uniaxial behaviour following the Stoner-Wohlfarth model.

In polycrystalline films the easy axes of the grains are randomly orientated. Because the density of the film is large ($>90\%$) and the typical M_s of the metallic grains is $\sim$ 1000 emu/cm^3, there are strong RKKY interactions so that reversal

proceeds via domain nucleation and wall motion. However because the films are not 100% dense and the occurrence of impurities at grain boundaries there are significantly more and stronger domain wall pins than for single crystal films. Generally this increases the coercivity above that of single crystal films and the loop is less square. The ferromagnetic domains in polycrystalline materials generally do not coincide with the grains. This is due to the limited dimensions of the grains and the interaction between neighbouring grains. As a result, a ferromagnetic domain in a polycrystalline material often consists of several interacting grains

2.5.3 Superlattices

The behaviour of superlattices follows the same behaviours as other magnetic films as discussed above and depend on the method of thin film growth. However the presence of multiple interfaces between the ferromagnetic layers and the non-magnetic layers gives rise to a possibility of an increase number of domain wall pins. In particular for polycrystalline thin films there can also be an increase of the strength of the pin arising from interface roughness. Similarly for single crystal superlattices lattice mismatch between the magnetic and non-magnetic layers can also generate domain wall pins.

The major difference between a superlattice and a single crystal film is the possibility of strong interlayer coupling. The ferromagnetic layer has a spin-density wave which induces a spin polarisation between the layers. The orientation of the spin polarisation with respect to each layer depends on multiple quantum interference effects, which due to the reflection of the electrons from internal interfaces causes an oscillatory coupling as demonstrated by Parkin [49] and illustrated in Figure 2. 12 [50]. It has clearly shown that the saturation field can be up to 10 kOe for antiferromagnetic exchange coupling superlattice samples.

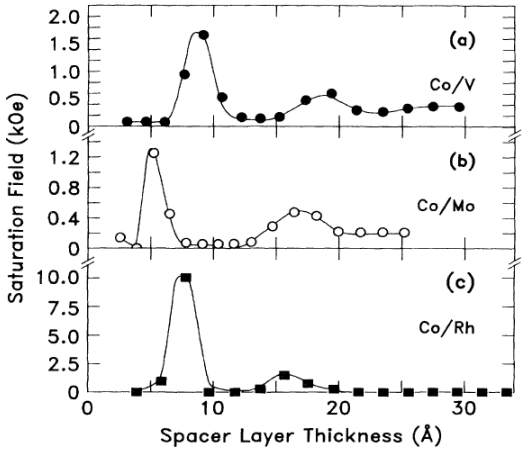

Figure 2. 12 The oscillation of exchange coupling between Co layers across different spacer layers by Parkin et al [49]

2.6 Magnetic Anisotropy

Magnetic anisotropy can be divided into magnetocrystalline anisotropy, shape anisotropy, exchange anisotropy and magnetoelastic energy [20]. Magnetic anisotropy is used to describe the dependence of the internal energy on the direction of the spontaneous magnetisation. When there is no magnetic field, the magnetisation (M) of a ferromagnet tends to align preferentially along the direction(s) of minimum energy known as easy axes. The easy axes depend on the crystalline structure or the shape of the sample [20].

In particular, magnetocrystalline anisotropy, stress anisotropy, shape anisotropy and strain anisotropy induced by the growth process contribute most to the magnetic anisotropy in the samples grown in this study. However, the effect of shape anisotropy is not taken into account but an interfacial strain effect can occur which gives rise to interfacial anisotropy.

2.6.1 Magnetocrystalline Anisotropy

In this studies, polycrystalline films and single crystal films are discussed. For the films are single crystal, they also have the magnetocrystalline anisotropy characteristic of single crystals. This will be superimposed on the uniaxial anisotropy normally present in polycrystalline films.

The origin of magnetocrystalline anisotropy arises from the spin-orbit (L-S) interaction of the electrons. For this anisotropy, the preferred directions of the moments depend on the crystallographic direction of the crystal [20]. The moment

of each crystallographic direction saturates at a different field and the one which saturates with the lowest energy is known as the easy axis of the magnetisation. When the moments are aligned along the hard axis the highest energy is reached. The energy difference between the minimum and the maximum is the magnetocrystalline anisotropy energy. Therefore, the magnetocrystalline anisotropy energy (E_K) depends on the angle with respect to the easy axis defined as [20],

$$E_K = K_0 + f(\alpha_1\alpha_2\alpha_3) \tag{2.13}$$

where K_0 is the anisotropy constant, f is a function determined by the symmetry of the crystalline system, $\alpha_1, \alpha_2, \alpha_3$ are the direction of cosines of the magnetic moment with respect to the crystal edge. Both cubic and uniaxial system are considered in this study. For the cubic case, equation (2.13) becomes,

$$E = K_0 + K_1(\alpha_1{}^2\alpha_2{}^2 + \alpha_2{}^2\alpha_3{}^2 + \alpha_3{}^2\alpha_1{}^2) + K_2(\alpha_1{}^2\alpha_2{}^2\alpha_3{}^2) + \cdots \tag{2.14}$$

where K_0, K_1 and K_2 are the anisotropy constants of the material.

$$E/V = K_0 + K_1 sin^2\theta + K_2 sin^4\theta + \cdots \tag{2.15}$$

where θ is the angle between the magnetic moment and the easy axis.

The anisotropy of the other Heusler alloy Co_2FeSi and $Co_2FeAl_{0.5}Si_{0.5}$ are discussed in the next chapter.

2.6.2 Shape Anisotropy

The shape anisotropy effect is important for the case of segregated polycrystalline films. In the previous section, the dominant magnetic anisotropies in epitaxially grown single crystal films are introduced. In some polycrystalline films, shape anisotropy can be the dominant anisotropy. The origin of this anisotropy is the demagnetising field of a non-spherical particle. With a non-spherical particle, the demagnetising field decreases if the magnetisation is along the long axis rather than along one of the short axes. Thus an easy axis of magnetisation is produced along the long axis. According to Trudel *et al*, a prolate spheroid of Co_2FeSi with no magnetocrystalline anisotropy exhibits the same uniaxial anisotropy as a spherical

particle of Co_2FeSi [51]. For a prolate spheroid, the shape anisotropy constant (K_s) is [20],

$$K_s = \frac{1}{2}\left(N_{short} - N_{long}\right)M_s^2 \tag{2.16}$$

where N_{short} and N_{long} are the shape demagnetising factors along the short and long axes respectively.

Chapter 3

Magnetism in Heusler Alloy Thin Films

Fritz Heusler discovered the first Heusler alloy, Cu_2MnAl, in 1903 when he was studying the ferromagnetism of different combinations of metals in alloys [52]. Heusler alloys can be composed of almost every metallic and semiconducting element in the periodic table. With different compositions of Heusler alloys, they can exhibit a wide range of properties that can be half-metallic ferromagnets, semiconductors, superconductors, topological insulators and many more [53-56]. Most of the Heusler alloys that are being studied are ternary compounds but quaternary compounds such as $Co_2FeAl_{0.5}Si_{0.5}$ [57, 58] are also being studied for spintronic applications. Heusler alloys can be divided into two groups, half Heusler alloys which have a 1:1:1 stoichiometry and full Heusler alloys with 2:1:1 stoichiometry which are also known as XYZ half Heusler alloys and X_2YZ full Heusler alloys respectively. Co-based full Heusler alloys attract significant research interest due to their unique properties. They exhibit metallic and ferromagnetic properties above room temperature and have high T_c as well as a good lattice match with widely used III-V semiconductors [59]. Not all Heusler alloys exhibit half-metallic properties above room temperature, therefore Co-based full Heusler alloys attract great interest for spintronic applications. The crystallographic, electronic and magnetic properties of the full Heusler compounds will be discussed in this chapter

3.1 Half-metallic Ferromagnets

Half-metallic ferromagnets can be understood by looking at the density of states (DOS) illustrated schematically in Figure 3.1. There are two bands: a majority spin band and a minority spin band. The majority band is filled with electron states up to the Fermi level giving metallic conduction while the minority states have a band gap resembling a semiconductor. The degree of spin polarisation in ferromagnets is important for the efficiency of spin dependent effects such as magnetoresistance or spin-transfer torque. As shown in equation (3.1), the spin polarisation is defined as the ratio of the density of states of up and down spin electrons at the Fermi level.

$$P = \frac{(D_{up} - D_{down})}{(D_{up} + D_{down})} \tag{3.1}$$

The value P = 0 corresponds to paramagnetic materials, P<1 corresponds to ferromagnetic materials and P = 1 corresponds to materials with perfectly spin-polarised conduction electrons which correspond to Figure 3.1. This implies that the energy band in either the up- or down-spin channel presents a gap at Fermi energy.

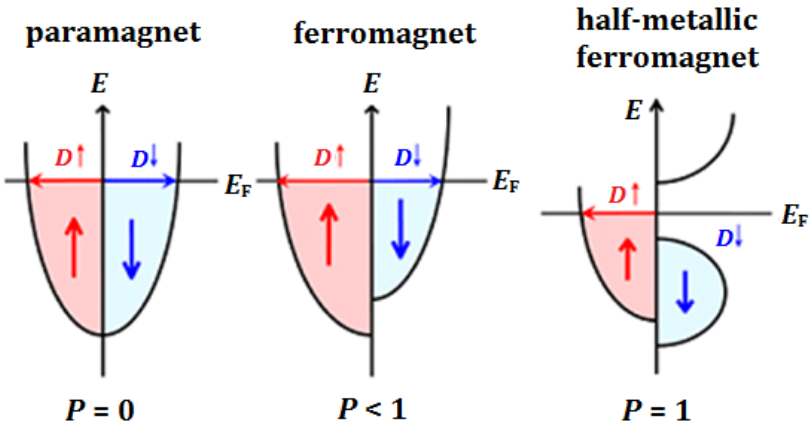

Figure 3.1 Density of states of paramagnetic, ferromagnetic and half-metallic ferromagnet and the definition of the electron spin polarisation [22].

Not all ferromagnetic Heusler alloys have half-metallic properties. By knowing the long range ordering of the atomic moments of the materials, their magnetic properties can be determined. However, these properties vanish at T_c. T_c is the critical temperature at which a ferromagnetic material becomes paramagnetic

and the natural ordering with alignment of the spins is no longer maintained [22]. This can be understood via the magnetic moments of the domains of the material. Below T_c, in a ferromagnetic material, each domain is magnetised due to the strong magnetic exchange interaction in the domain which tends to align the individual magnetic moments within the domain and gives rise to spontaneous magnetisation. [20].

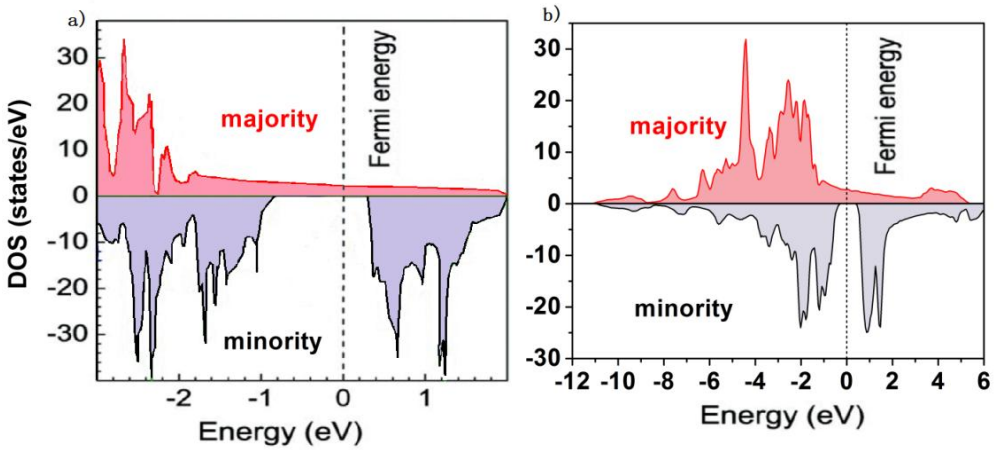

Figure 3.2 Density of states of a) Co_2FeSi [60] and b) $Co_2FeAl_{0.5}Si_{0.5}$ [7]. Reproduction of Figure 1.3.

A DOS diagram of two specific materials, Co_2FeSi and $Co_2FeAl_{0.5}Si_{0.5}$, are shown in Figure 3.2. There is only one spin channel in the density of states that is metallic but the other is insulating when there is a gap at E_F. This phenomenon gives theoretically 100% spin polarisation to the conduction electrons. This property of half-metallic ferromagnetism makes them ideal spintronic materials since a source of high spin polarised electrons is essential for spin transport. In recent years, a large sub-family of Heusler alloys have been investigated and have been shown to be half-metallic ferromagnets. Both Co_2FeSi [60] and $Co_2FeAl_{0.5}Si_{0.5}$ [61] are half-metallic ferromagnets and exhibit both metallic and semiconducting behaviour. Moreover, $Co_2FeAl_{0.5}Si_{0.5}$ was found to have P~91% at room temperature and it exhibits the smallest temperature dependence in its spin polarisation near room temperature [61].

At room temperature, the direction of the magnetic moments of the material can be altered by an external magnetic field. All these properties are very useful for developing spintronic devices, such as read heads as discussed in section 3.8.1. The selected Heusler alloys, Co_2FeSi and $Co_2FeAl_{0.5}Si_{0.5}$, for this study are discussed in more detail in the following sections.

3.2 Origins of Half-metallic Behaviour in Heusler Alloys

The first half-metallic Heusler alloy, NiMnSb, was predicted by de Groot *et al.* in 1983 on the basis of band structure calculations [62] and was verified in the 1990s by other researchers [63, 64]. Furthermore, the full Heusler alloys, *i.e.*, Co_2MnZ (Z= Si, Ge) were proposed by Ishida *et al.* as a half-metallic ferromagnet [65] and described in detail by Galanakis *et al.* in 2002 [66].

In order to explain the gap in the minority spin channel of the band structure, *spd*- orbitals are introduced. All elements X, Y and Z have *spd*- orbitals where all four *sp*- orbitals sit below the Fermi level. Therefore, only the *d*- orbital contributes to the formation of the gap in the band structure of this material. The hybridisation of *d* electrons between Co and Mn and the Co –Co atoms sitting on the second nearest neighbour positions lead to the gap in the minority spin channel of the Heusler alloy material as described by Galanakis *et al.* [66].

Due to the requirements of ordering of 3*d* and 4*s* bands in the band structure, single elemental half-metallic ferromagnets do not exist and at least binary alloys or compounds are required. In ternary or quintenary Heusler alloys, for instance the half Heusler NiMnSb alloy, all Mn atoms are surrounded by six Sb atoms, where Sb *p* states split the Mn 3*d* states into a low-lying triplet of t_{2g} states. On the other hand, Ni has the lower energy *d* states of a high valent transition metal and Mn has higher energy *d* states of a lower valent transition metal which leads to the formation of bonding and anti-bonding bands as shown in Figure 3.3 [66]. This formation originates from covalent hybridisation between Ni and Mn.

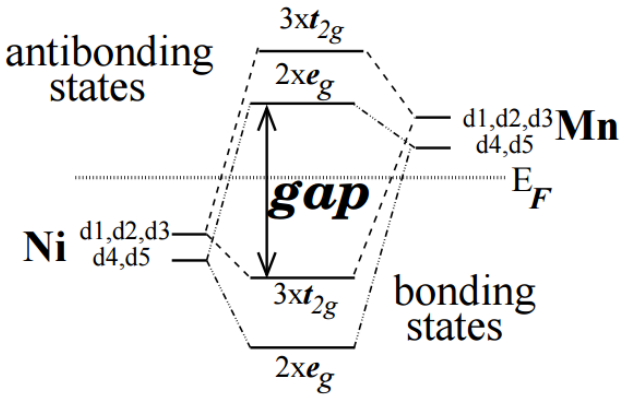

Figure 3.3 Schematic diagram of the origin of the gap in the minority band in NiMnSb [66].

However, it is more difficult to describe the origin of half-metallicity in

Co-based full Heusler alloys. Galanakis *et al.* first calculated the Co-Co interaction which is shown in Figure 3.4 [66]. This detailed study was on $Co_2Mn(Z)$, (Z= Si or Ge), but Co_2FeSi is expected to have the same hybridisation in *d* orbitals. This is because the two Heusler alloys have similar structural and electronic properties. Figure 3.4 shows a possible hybridisation between *d* orbitals for minority states of Co_2MnGe by considering the Co-Co interaction and Mn-(Co-Co) interaction. It shows that the Mn atoms hybridise in a similar way as in Co-Co. The *d*-orbitals are divided into five degenerate states; three-fold degenerate (t_{2g}) bonding states and two-fold degenerate (e_g) anti-bonding states. The bandgap is formed between the higher t_{2g} bonding hybridised states in the valence band and the lower e_g anti-bonding states in the conduction band of the Co-Co and the Mn *d*-orbitals as shown in Figure 3.4. Galanakis *et al.* explained that this interaction with the Mn leaves five hybridised orbitals from the Co-Co interaction free. The three t_{1u} orbitals sit just below E_F while the two e_u orbitals sit just above [67]. As a result, there is a gap at E_F for the minority spin channel which gives the half-metallic properties.

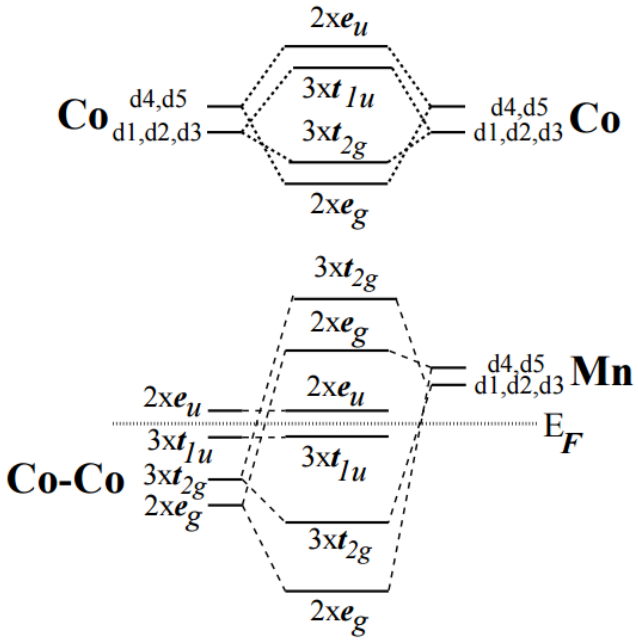

Figure 3.4 Possible hybridisation between d orbitals for minority states for the compound Co_2MnGe by considering a) the Co-Co interaction and b) the Mn-(Co-Co) interaction [66]

3.3 Slater-Pauling Behaviour

The origin of the half-metallic property of ferromagnetic Heusler alloys has been discussed in the previous sections but not the origin of ferromagnetism of Heusler alloys. The origin of ferromagnetism was first studied by Slater [68] and Pauling [69] in the 1930s, they both found that the ferromagnetism originated from the spin on the electrons in the $3d$ orbital. They discovered that the magnetic moment of a $3d$ metal can be estimated by knowing the total number of valence electrons (Z_t) per atom. The $3d$ orbital in ferromagnetic transition materials is the only orbital shell which is not filled with equal numbers of spin up and spin down electrons. With different numbers of unpaired electrons and positive exchange energy with neighbouring atoms leads to ferromagnetism and/or half-metallic behaviour which was discussed in the previous section.

It is well known that the total magnetic moment (M_t) in a unit cell is proportional to the value of Z_t (total number of valence electrons) of the material according to the generalised Slater-Pauling theory. Full Heusler alloys follow the Slater Pauling 24-electron-rule [66]:

$$M_t = Z_t - 24 \tag{3.2}$$

The 24 means that there are 12 occupied spin-down states, which is the number of uncompensated spins, is given by the total number of valence electrons Z_t minus 2 times the number of minority electrons. The generalised Slater-Pauling theory is essential to understand and explain the magnetic properties of the materials. Furthermore, by applying the Slater-Pauling rules, the spin DOS at E_F can be controlled and the material can be engineered to provide specific magnetic properties. Since X, Y and/or Z atoms can be substituted with desired elements which match the value of Z_t, Figure 3.5 shows how Slater-Pauling rules can be applied for some commonly used Co-based Heusler alloys. It clearly shows that with $Z_t<9$ materials are in the localised region of the curve and are most likely to exhibit a bcc structure.

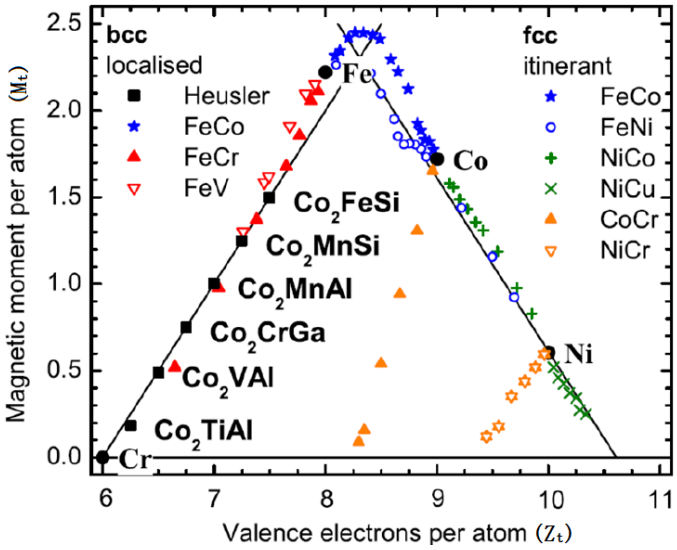

Figure 3.5 The dependence of the M_t on Z_t for 3d elements by applying generalised Slater-Pauling rules [66].

By substituting X, Y and/or Z with other elements and applying the generalised Slater-Pauling rules, the properties of the Heusler alloy can be engineered. It has been proven that the generalised Slater-Pauling rule can also apply to quaternary materials such as $Co_2FeMn_xSi_{1-x}$ [70] and $Co_2FeAl_xSi_{1-x}$ [67] which have shown an improvement in their half-metallic properties.

3.4 Heusler Alloy Structure and Disorder

As mentioned, there are half and full Heusler alloys and the difference between them is that the half Heusler consists three fcc sub-lattices and the full Heusler consists of four. Generally, half Heusler alloys have a $C1_b$ structure in which two fcc sub-lattices remain unoccupied. Full Heusler alloys have an $L2_1$ structure and have two X atoms which occupy all sub-lattice sites as shown in Figure 3.6 [71]. The first half-metallic $L2_1$ Heusler alloy was proposed by Groot in 1983 [62].

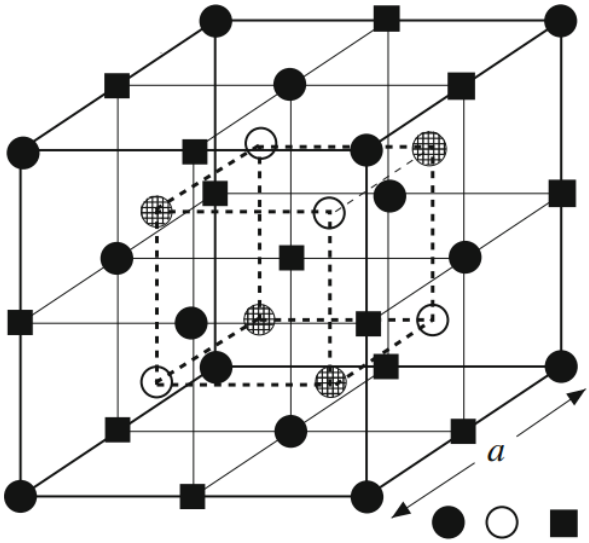

	A	B	C	D
Semi–Heuslers ($C1_b$) : XYZ	X	Y		Z
Full–Heuslers ($L2_1$) : X_2YZ	X	Y	X	Z
Quaternary Heuslers : (XX')YZ	X	Y	X'	Z
Inverse Heuslers (XA) : X_2YZ	X	X	Y	Z

Figure 3.6 Schematic diagram of various Heusler structures [71].

Co-based Heusler alloys with an $L2_1$ structure have potential to enhance the quality of spintronic devices due to the fact that they are predicted to have 100% spin polarisation at E_F. With high spin polarisation, more effective spin dependent scattering can be achieved and so spintronic devices can have better signal-to-noise ratios and a more robust readout.

Since the first Heusler alloy Cu_2MnAl was discovered in 1903 [52], scientists have been investigating these materials for over a hundred years and over 2400 Heusler alloy compounds have been studied [72, 73]. Based on previous studies, Co-based Heulser alloys have many attractive properties which are the large value of M_s, low value of H_c and large ratio of M_r/M_s (where M_r is the remanent magnetisation), high T_c and many other physical properties which can be manipulated by magnetic [36, 74, 75] or electric fields [76, 77]. These are important factors for optimising thin film devices. These factors can help to reduce the energy losses associated with the reversing field and to improve the efficiency of spintronic devices.

As mentioned full Heusler alloys tend to crystallise in the $L2_1$ structure, this structure gives a high T_c (>1000K) and large intrinsic magnetic moment [$>5\mu_B$/f.u. (formula unit)] [78] making them more useful for practical applications. In single

crystal $Co_2FeAl_{0.5}Si_{0.5}$ films, long range $L2_1$ ordering was observed, the extent of which increases monotonically with annealing temperature.

In Figure 3.7, different Heusler alloy sturcture are shown. For some disordered phases, a small degree of half-metallic properties are maintained such as for the $B2$ disordered structure. However, $A2$ and DO_3 disorder structures give no half-metallic properties [79].

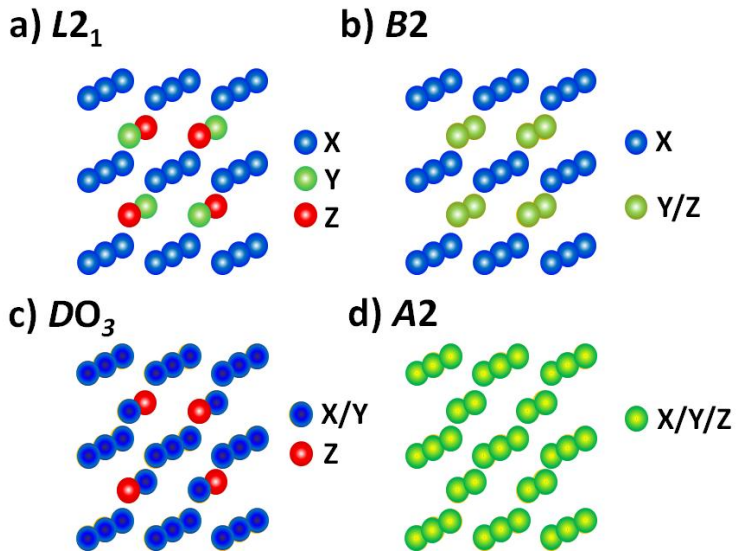

Figure 3.7 Diagrams of possible disordered phases within Heusler compounds [71]. Reproduction of Figure 1.5.

This spin polarisation can be applied to a magnetoresistive effect such as TMR. According to the Julliere model,

$$\mathrm{TMR} = \frac{\Delta \mathrm{R}}{\mathrm{R}} = \frac{2\mathrm{P}_1\mathrm{P}_2}{1 - \mathrm{P}_1\mathrm{P}_2} \tag{3.3}$$

where P_1 and P_2 are the value of the spin polarisation of the top and bottom electrodes respectively [5]. Thus, high spin polarisation of the materials is essential for realizing a large TMR ratio and developing efficient spintronic devices.

3.5 Structural Properties of Heusler Alloys

Heusler alloys are ternary intermetallic compounds. Full Heusler X_2YZ alloys crystallise in the $L2_1$ structure sometimes with a mixture of a $B2$ structure at the stoichiometric composition. The elements associated with X and Y are atoms with large magnetic moments which is transition metal with *s*, *p* valence electrons. The atom denoted Z is a non-magnetic and a non-transition metal. In the $L2_1$ structure,

the unit cell consists of four interpenetrating fcc sub-lattices with the positions (0, 0, 0) and (½, ½, ½), (¼, ¼, ¼) and (¾, ¾, ¾) for X, Y and Z atoms respectively [72]. Some properties of a few well known Heusler alloy with different compositions are listed in Table 3.1. Only $L2_1$ /$B2$ structure Heusler alloys are favourable due to better lattice matching with single crystal silicon. From Table 3.1, it is clear that Co_2FeSi and $Co_2FeAlSi$ have the highest T_c and magnetic moment.

Heusler ally	Crystal structure	Magnetic moment at 5K (emu/cm^3)	Curie temperature (K)
Co_2FeSi	$L2_1/B2$	5.97±0.05 [60]	1185±20 [73]
$Co_2FeAlSi$	$L2_1/B2$	5.5 [80]	1150±50 [81]
Co_2MnSi	$L2_1/B2$	5.10±0.04 [82]	985[83]
$Co_2Cr_{0.6}Fe_{0.4}Al$	$A2/B2$	3.2 [84]	760 [84]

Table 3.1 List of Co-based Heusler alloy

The electronic structure and physical properties of Co_2YZ Heusler alloys can be manipulated by replacing either the Y or Z atom with a fourth element which allows the engineering of desired characteristics. For instance, $Co_2FeAl_{0.5}Si_{0.5}$, Fe and (Al,Si) are surrounded by eight Co atoms as shown in Figure 3.8. The $L2_1$ structure is required due to its high degree of ordering as the half-metallicity is very sensitive to the atomic disorder in the crystal structure [77].

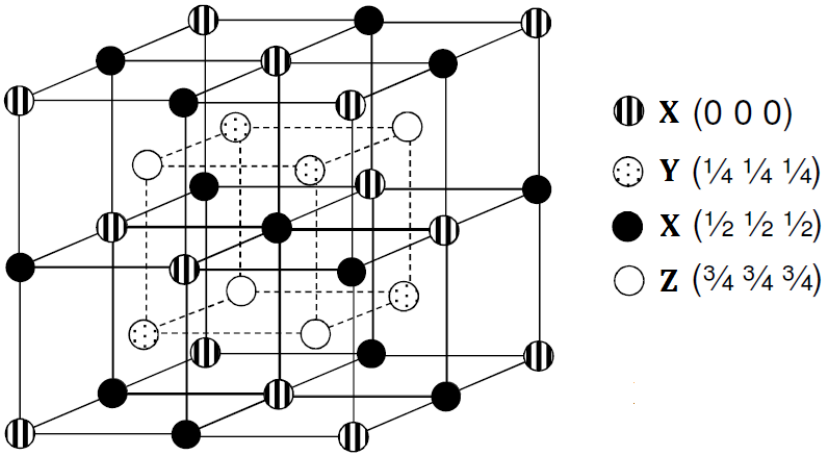

Figure 3.8 Crystal lattice of $L2_1$ structure

However, at the stoichiometric composition, disorder can exist in the form of partial interchange of atoms in different sub-lattices. $Co_2FeAl_{0.5}Si_{0.5}$ has been shown to exhibit partial mixtures of the $L2_1$ and $B2$ structures. Some alloys, such as Co_2FeSi [44, 60], crystallise easily in the $L2_1$ structure while others, like Co_2FeAl [85], tend to

form the *B*2 structure rather than $L2_1$. Even though in principle the degree of ordering can be modified by annealing but in the case of $Co_2FeAl_{0.5}Si_{0.5}$ the annealing temperature for $L2_1$ ordering is very high >600 °C [86] and Cr interlayer diffusion is also an obstacle for annealing [87]. The magnetic and electronic properties are in general sensitive to the degree of disorder in the alloys.

3.6 Effect of Structure on the Magnetic Properties

As discussed in sessions 3.2 and 3.3, the magnetic moments in Co-based Heusler alloys come from spin moments of valance electrons localised to the *d* orbitals of the Co atoms. The magnetic moment of the Heusler alloys originates from the complex hybridisation of these atomic orbitals of the material. When there is any variation in the local hydridisation, the band structure of the material changes. Therefore, it is very important to understand the effect of changing the inter-atomic spacing of these atoms as the moment of the material can be changed if the lattice constant is different. It is well known that disorder has a significant influence on the moment of these materials [42, 71]. The disorder effect discussed in this section can be applied to both Co_2FeSi and $Co_2FeAl_{0.5}Si_{0.5}$.

For instance, the moment of a unit cell of fully ordered $L2_1$ Co_2FeSi was experimentally measured to be 6 μ_B/f.u. [88]. There are three types of disordered $L2_1$ structure which are *B*2, DO_3 and *A*2 as shown in Figure 3.7.

By using density functional theory, the effect of these atomic swaps can be calculated [89]. According to Li *et al.*, Co-Fe swaps with just 10% atomic disorder reduces the moment per formula unit to 5.5 μ_B [90]. This is due to the lowering in M_t of the Fe atom and the increase in M_t of the Co atom. The Co-Si swaps with the same amount of disorder are surprisingly predicted to cause an increase in the moment, which increases to 6.05 μ_B/f.u. The increase in moment is because of the inter-atomic bond changes as discussed in session 3.2 [90]. The Fe-Si swaps forming *B*2 disordered structures were found to retain the 6 μ_B/f.u moment predicted for the $L2_1$ structure up to 10% disorder. By swapping Fe and Si, there is a change in the crystal field symmetry at the Co and Fe sites which leads to an additional splitting in the *d*- orbital similar to that discussed in section 3.2. This does not affect the magnetic moment as is the case for the other disordered structures, and therefore the moment per formula unit remain at 6 μ_B/f.u. The above disorders are all at a low

disorder level since when the disorder level increases the half-metallic property of the alloy will be destroyed which is not the desired result for both Co_2FeSi and $Co_2FeAl_{0.5}Si_{0.5}$.

3.7 Co_2FeSi and $Co2FeAl_{0.5}Si_{0.5}$ Heusler Alloys

Co_2FeSi and $Co_2FeAl_{0.5}Si_{0.5}$ are well-established half-metallic Heusler alloys and promising candidates for spintronic devices. First of all, Co_2FeSi was chosen for study as it has the highest reported T_c >1100K [60], and the reported $L2_1$ structure can be easily achieved by post annealing [84]. It has a large magnetic moment of 6 μ_B/f.u. [88]. On the other hand, $Co_2FeAl_{0.5}Si_{0.5}$ also has high T_c of ~1150K [81], high spin polarisation of 70% [89] and 81% for $B2$ and $L2_1$ [81] structures at room temperature and large magnetisation of 1200 emu/cm^3 [81]. Both alloys have a large band gap with E_F in the middle of the minority gap which is required for spintronic applications [7, 60]. By adjusting the concentration ratio of Al and Si, the Fermi level can be tuned to achieve a full band gap for minority spin energy as a half metal.

The highest TMR ratio for Co_2FeSi based MTJ structure was found to be 167% at 15K [92] and for a $Co_2FeAl_{0.5}Si_{0.5}$ based MTJ structure the TMR ratio was found to be 386% at room temperature [93] and 832% at 9K [94] which is much larger than that for a Co_2FeSi based structure. The disadvantage of $Co_2FeAl_{0.5}Si_{0.5}$ is that it is not stable in the $L2_1$ structure but a mixture of $B2$ and $L2_1$ ordering which is discussed in the chapter 5. As discussed in the previous chapter, the half-metallic properties are highly dependent on the structure of the material. Therefore, $Co_2FeAl_{0.5}Si_{0.5}$ was chosen to be grown epitaxially in this study. And $Co_2FeAl_{0.5}Si_{0.5}$ was theoretically predicted [7] to be a half metal which is the main focus of this work.

A seed layer has been introduced to Co_2FeSi polycrystalline films to study the effect on the physical and magnetic properties. The optimised structure with a seed layer was then applied to the epitaxial growth of $Co_2FeAl_{0.5}Si_{0.5}$ films.

3.8 Applications of Magnetoresistance Effect with Heusler Alloys

By manipulating the spin polarised electrons, the performance of spintronic devices can be optimised, *e.g.* increasing areal density in hard disk drive (HDD), lower power consumption of the devices and miniaturisation. To date, spintronics is

a part of our daily life and it has been applied to storage devices. It is also been applied to daily used vehicles and future robotics. Two applications are discussed in the following sections.

3.8.1 Read Heads in Hard Disk Drives

In spintronics, half-metallic Heusler alloys are considered to be ideal materials for device applications due to their magnetic properties and electronic structures [7, 60]. Large MR ratios are always desired for devices and a direct method to enhance this effect using a high spin polarisation material makes Heusler alloys potential candidates. Since IBM introduced the first MR read head in HDD in 1991 [29], the areal density has increased tremendously as shown in Figure 3.9. Since the areal density development is steady, researchers started to look into improving scalability. However, the first MR read head used the anisotropic magnetoresistive (AMR) effect in which the efficiency is thickness-signal strength dependent. By lowering the thickness of the AMR based devices, the output signal amplitude is

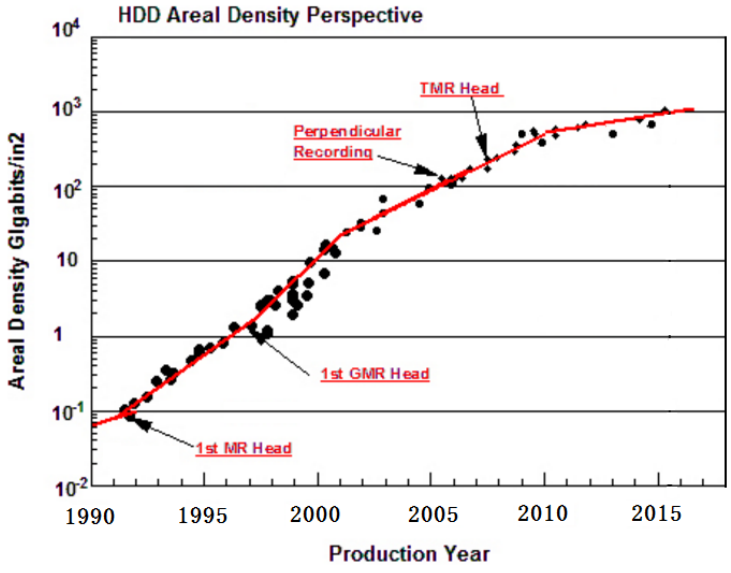

Figure 3.9 A diagram of areal density perspective between 1990-2016 [92].

lowered proportionally. The first observed trilayer spin-valve GMR effect was in 1991 with the structure shown in Figure 3.10. In the following years, IBM researched on the scalability factor and introduced the first CIP GMR read head in 1997 to fulfil the scalability desired [29].

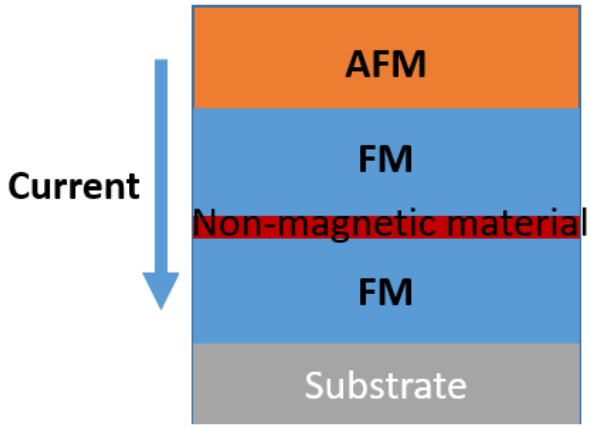

Figure 3.10 Schematic diagram of a spin-valve CPP-GMR stack.

The quality of digital devices such as cameras, videos and graphical resolution demands large storage capabilities. However, the areal density was not more than 1 Gbit/in^2 before 1997 [29]. There was a great impact on the magnetic recording industry when IBM introduced the GMR based read head, and by 2000 100% HDD production included GMR read heads. Furthermore, the areal density has increased to 300 Gbit/in^2 within 10 years with this evolution. This technological leap has completely changed the recording media market.

As high density and smaller scale of HDD is in demand, CIP GMR spin vavle sensor is inadequate. According to simulation by Takagishi *et al.*, a MgO based GMR read head can achieve a 2 Tbit/in^2 areal density [95]. CPP GMR was then used in the industry as the RA requirement is less restricted.

The first Co-based Heusler CPP GMR spin-valve sensor was achieved in 2006 but the MR ratio was only 2.4% with no specific lattice structure and 5.2% with an $L2_1$ ordered lattice structure [32] at room temperature. An MR ratio of 34% was achieved with $Co_2FeAl_{0.5}Si_{0.5}$/Ag/$Co_2FeAl_{0.5}Si_{0.5}$ trilayer structure [96] and the largest intrinsic MR ratio of 82% at room temperature (182% at 4K) was reported for a $Co_2FeGa_{0.5}Ge_{0.5}$/Ag/$Co_2FeGa_{0.5}Ge_{0.5}$ pseudo spin-valve [4]. This proves that Heusler alloys are strong candidates for the development of spintronic devices.

As mentioned in previous section, CIP GMR has size limitation due to its planar geometry. To further reduce the dimensions of read head and meanwhile increase the storage density of HDD data storage, MTJ sensors were introduced which is based on the phenomenon of TMR [97]. In theory, TMR ratio can reach 1000% [34] with a MTJ sensor but in reality the largest TMR ratio has reported is

604% [14]. This suggests that the TMR ratio can still be improved which one method is to use high spin polarisation ferromagnetic materials in MTJ.

3.8.2 Magnetoresistive Random Access Memory

Apart from HDD, the TMR effect is also applied to the other devices such as magnetic random access memories (MRAM). Increasingly, storage used nowadays is volatile random access memory (RAM) which means if the device is shut down, anything which is not saved is lost.

Type of RAM	DRAM	Flash	MRAM (STT)
Density	8 Gb/chip	64 Gb/chip	64 Mb/chip
Energy consumption per bit	2 pJ	10 nJ	0.02 pJ
Non-volatility	No	Yes	Yes

Table 3.1 Summary of three types of RAM technology [95, 96].

MRAM requires the lowest energy per bit among all current RAM technologies as shown in Table 3.1. MRAM is a non-volatile memory and all information is retained if the device is shut down [97, 98]. Other than the main advantage of non-volatilility, MRAM has many other unique qualities. For example high speed operation (10^{-9} s), radiation hardness and it can operate at extreme temperatures (-40˚C to 125˚C) [99]. With all these unique advantages, MRAM is expected to replace flash memory and the current dynamic random access memory (DRAM) [97, 98]. MRAM consists a series of MTJs to store data and a metal oxide semiconductor transistor which acts as a switch to select data location to read as shown in Figure 3.11. An MTJ structure is similar to the GMR spin-valve, in both case electron spins align with the magnetic moment inside a ferromagnet but the difference is that in an MTJ current passes perpendicular to the plane through an insulating barrier instead of non-magnetic material. In MRAM, data stores as a magnetisation state in an F layer in an MTJ. Data is stored in the direction of magnetisation in F1 free layer and the pinned F2 layer remains with its predetermined direction.

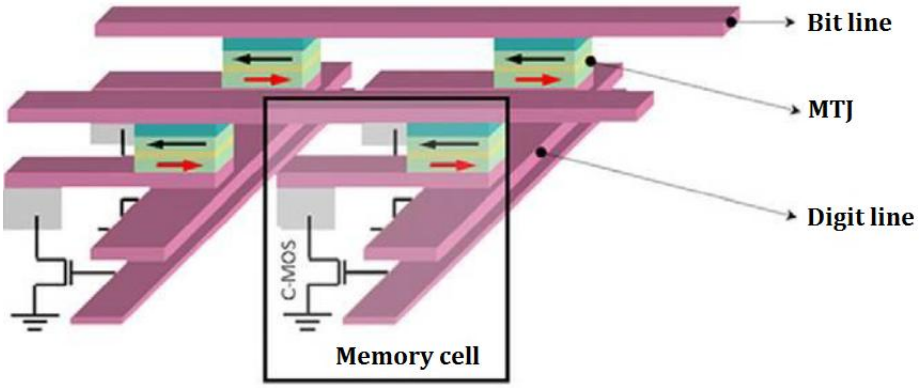

Figure 3.11 A schematic diagram of a MTJ MRAM device [100].

The state of the art MRAM is the spin-transfer-torque (STT) MRAM. A STT-MTJ consists of two F layers separated by a thin NM layer. The first F layer is the reference layer which polarises the current then passes through the NM layer with no change in the polarisation and interacts with the second F layer which is the free layer. For STT-TMR, there is a transfer of spin angular momentum from the polarised current which act as a torque on the free layer. When the polarised current density is large enough, the spin torque will induce magnetisation reversal in the free layer [97]. Therefore, information is recorded by inducing magnetisation reversal in the free layer. In STT-MRAM, recently a newly designed 5-Gbit STT-MRAM test chip was presented in 2017 Intermag Conference which enables the memory cell area to be smaller without degrading the electric and magnetic properties. The size of MRAM has downscaled to a new level based on the recent presented work [101] which makes STT-MRAM more favourable. Apart from the reduction in size, STT-MRAM is more favourable because of its outstanding high operating speed, high reliability, long endurance, non-volatility and low writing energy.

Chapter4

Deposition of Thin Films

4.1 Physical Vapour Deposition

There are a number of ways to grow thin films, such as ion beam deposition (IBD), pulsed laser deposition (PLD), magnetron sputtering (MS) and molecular beam epitaxy (MBE) [102]. In this study a high target utilisation sputtering (HiTUS) system and an MBE system have been used. Other methods were not used due to the production of high average particle energies, growth conditions which do not meet the requirements for epitaxial growth Heusler thin film.

Pulsed laser deposition also has its advantages and disadvantages. The pulsed laser deposition process is flexible and can be carried out in any environment. It can easily control the growth by changing the laser properties, such as laser energy. On the downside films produced by pulsed laser deposition can have a high level of defects, *i.e.*, creation of small droplet or particulates and uneven coverage of the substrate [104]. Film roughness and texture are important for thin film deposition. In order to gain full control of deposition a high vacuum environment is crucial.

Preliminary thin film samples were produced by a sputtering system. Sputtering was first described by Grove in 1852 [105]. Since the discovery this phenomenon has been used widely in industry for coating metals, thin film production, etc. A basic sputtering mechanism is shown in Figure 4.2. Argon (Ar^+) ions are typically used to generate plasma for sputtering. The Ar ions are accelerated towards a cathode target with which they collide. Target atoms/ions and secondary electrons are extracted from the target after the collision and the target atoms/ions are deposited onto a substrate. The sputtering system used in this project is described in detail in the next section.

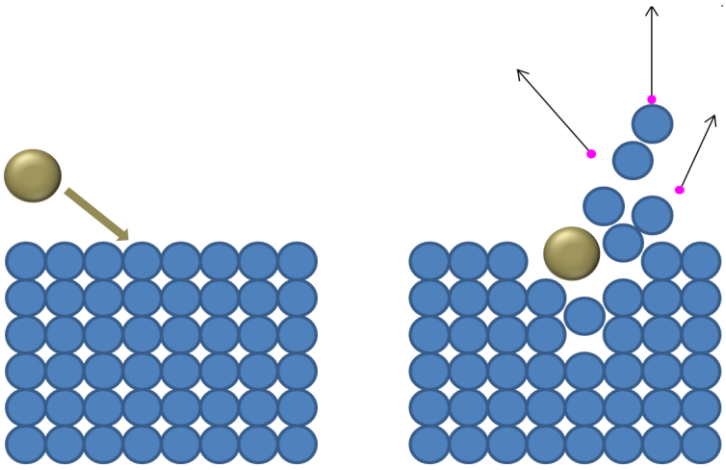

Figure 4.1 Schematic diagrams of the basic sputtering mechanism. Gold: Ar ions, blue: target atoms/ions and purple: secondary electrons.

MBE is the other growth technique which has been used throughout this project. It provides ordered growth on a crystal surface by slow evaporation of a metal or alloy in ultrahigh vacuum (UHV). Development of the MBE system started in late 1960s. In 1969, A. Y. Cho advanced the development of molecular beam sources. The first controlled epitaxial growth was done in 1970s [106]. The MBE system continued to be developed in the late 1980s and became widely available. Real-time growth monitoring system was also introduced in the same period [107]. In-situ annealing and in-situ reflection high-energy electron diffraction (RHEED) can be carried out in the MBE system in York. With the UHV environment ($<10^{-8}$ Pa) in the MBE chamber, high quality epitaxial growth is guaranteed. The MBE system used in this project is described in detail in section 4.3.

4.2 High Target Utilisation Sputtering (HiTUS)

Sputtering can be used to remove contaminants and to polish surfaces but the most important and useful application is to deposit thin films on a substrate. In order to achieve a high degree of grain size control in Heusler alloy thin films, conventional magnetron sputtering is not adequate. Racetrack target source formation is common in conventional magnetron sputtering and it is uncontrollable. The thin films investigated in this work were initially prepared using a Plasma Quest Ltd HiTUS deposition system whose basic set up is shown in Figure 4.3, later in the work films were grown using MBE.

The HiTUS system can control the thickness, grain size, morphology and other characteristics of the films. The HiTUS system eliminates the magnetron and the

whole surface of the target can be used uniformly improving the target utilization 90–95% [108]. Also the target to substrate separation of ~30 cm prevents resputtering.

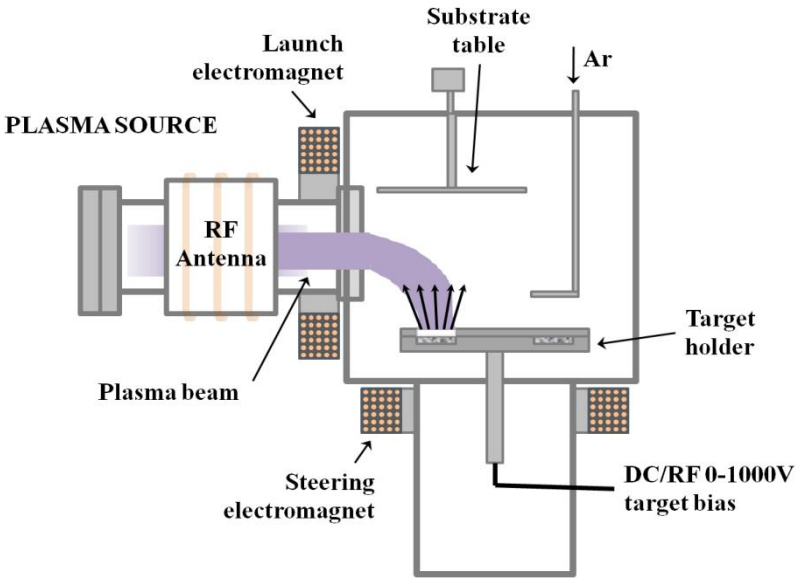

Figure 4.2 Schematic diagram of the HiTUS system [106].

A high density plasma is generated in a quartz tube outside the chamber as shown in Figure 4.3. This plasma is injected into the chamber with a power of up to 2.4 kW at 13.56 MHz radio frequency (RF). The plasma is then launched into the chamber via a static magnetic field from a launch electromagnet and localised by a steering electromagnet onto a water cooled target surface. The applied fields of the launch and steering electromagnets are 50 Oe and 500 Oe respectively. The energy of the ions in the plasma is between 30 eV and 50 eV which is insufficient to sputter material from the target directly [109]. A DC bias voltage of up to 1000 V is applied to accelerate the Argon ions for sputtering. The quality of the film is dependent on multiple factors: The DC bias voltage controls the Ar^+ energy and hence the growth rate which varies the size of the grains in the film and hence the surface or interface roughness. The distance between the substrate and the target also affects the quality of the film. An optimised distance (28 cm) is used to eliminate the interaction between the plasma and the substrate. This ensures uniform deposition across the substrates and the TEM grids. It has been found that the grids have films with the same grain size as the substrates allowing for TEM analysis that sample thinning is not needed.

The rotational target carousel holds eight different targets as shown in Figure

4.3 (b). The rotational substrate holder holds two substrates as shown in Figure 4.3 (a). This allows six samples to be sputtered in a single run without breaking the vacuum in the chamber. The design of the sample holder is also different from a conventional sample holder in a sputtering system. This sample holder can hold two 5x5 mm^2 square Si substrates for magnetic measurements and two 3.05 mm diameter carbon coated TEM grids for TEM studies. The deposition of multilayers is performed using an automatically controlled shutter and the rotation of the target carousel which can hold up to 8 targets.

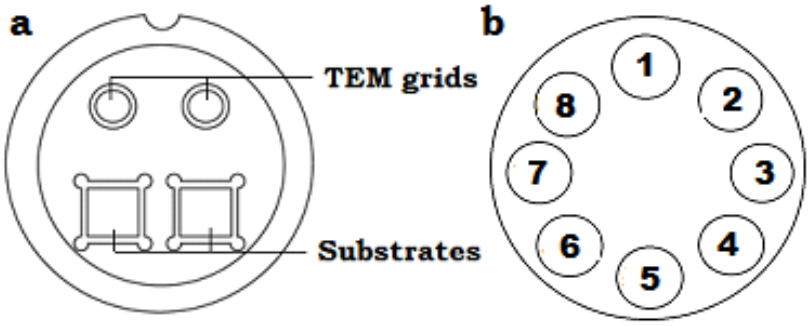

Figure 4.3 Diagrams of (a) the sample holder and (b) the rotational target holder.

The base pressure of the system was ~10^{-5} Pa achieved by a combination of a rotary/turbo pump system and a cryo pump. During deposition the pressure was ~1 Pa. This pressure allowed only materials sputtered from the target to reach the substrates during the growth process. Before deposition, the targets and substrates were cleaned using the Ar plasma to improve adhesion and to remove any SiO_2 and other contaminations. Turning off the electromagnet placed beneath the target caused the plasma beam with low energy (30 eV) to impinge on the substrates.

The system allows fine control of the deposition rate of materials by varying the Ar^+ flow rate, the RF power or the applied bias voltage (V_B) [109]. In this study the growth rate was controlled via V_B and the deposition rate and film thickness were measured by a 弓 Inficon XTM/2 deposition monitor. For changing the flow rate of Ar gas, the RF ionisation field and the Ar gas pressure are needed to be changed respectively. The monitor operates based on a piezoelectric quartz crystal oscillator. When applying an alternating voltage across the crystal, it oscillates with a periodic motion and mechanical resonance occurs when the natural frequency of the crystal and the frequency are identical. The monitor measures the crystal

oscillation frequency during the deposition. A reduced resonant frequency occurs during film deposition,

$$\frac{M_f}{M_q} = \frac{(\Delta F)}{F_q} \tag{4.1}$$

where M_f is the mass difference after deposition, M_q is the original mass of the crystal, ΔF is the change in frequency and F_q is the original quartz crystal frequency. In order to measure the thickness, the material's density and atomic number are required. The final factor to obtain accurate thickness of deposition is the tooling factor,

$$TF(\%) = TF_I\left(\frac{t_a}{t_c}\right) \tag{4.2}$$

where TF (%) is the tooling factor, TF_I is the initial tooling factor, t_a is the actual deposited thickness and t_c is the thickness displayed on the monitor. The accuracy of the monitor is $\pm 5\%$. To change the applied bias voltages simply change the input on the controller screen [109].

The control of deposition process is simple in this system. Samples can be prepared within 30 mins and confirmed to be highly reproducible. Therefore all the polycrystalline films were grown by the HiTUS system.

According to Hirohata et *al.*, annealing time and applied bias voltage can control the Si-segregation for Co_2MnSi sample. In order to set an optimal applied voltage for sample growth, a preliminary measurement is performed and discussed in chapter 5.

4.3 Molecular Beam Epitaxy

Epitaxial growth of thin films is crucial for developing nanotechnology and spintronic devices. Epitaxial growth means highly-ordered growth of crystalline film on a single crystal substrate. MBE is a deposition method which utilises well-defined thermal beams of molecules. In order to achieve an epitaxial (*i.e.*, single crystal like layer), a slow deposition rate, typically 0.01 nm/s, is required allowing materials to grow atomic layer by layer [110].

The MBE system in York (Eiko, HDH-10000) consists of two units, a load-lock chamber and a main chamber, as shown in Figure 4.5. The base pressure of the

load-lock chamber is 5.0×10^{-6} Pa and that of the main chamber is 2.0×10^{-8} Pa. Pressure lower than $\sim 10^{-8}$ Pa is called ultrahigh vacuum (UHV). There is a gate valve between the load-lock and main chamber, which is only opened while transferring a substrate holder to maintain the UHV in the main chamber. Under the UHV environment, the interactions between evaporated materials and atmospheric gases can be reduced to minimal [111].

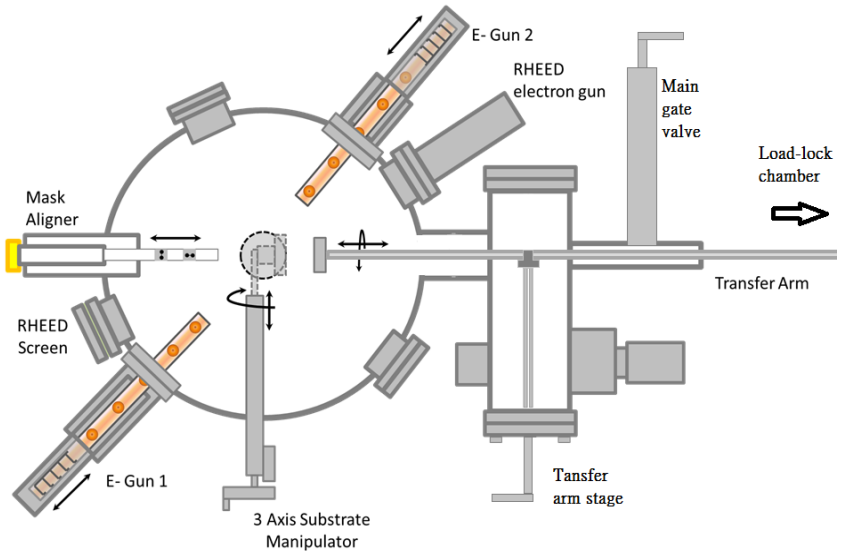

Figure 4.4 Schematic diagram of the MBE system.

In this MBE system, there are two different types of deposition methods which are a Knudsen cell (K-cell) and two electron guns (e-guns). The K-cell is situated at the bottom of the main chamber where low partial pressure materials are heated by a filament. Moreover, the cell has a self-contained cooling system and heat shield to ensure slow deposition rates. The other method to heat the target sources is by using the electron guns. The two e-guns in this system have five sources each. Including the Al source in the K-cell, there are a total number of 11 different target sources. The system hence allows complex multilayer films to be grown. A reflected high energy electron diffraction (RHEED) system is integrated with the MBE main chamber, which is used to monitor the epitaxial growth of the crystalline layers. For micro-scale device fabrication, three *in-situ* masks can be used to make desired patterns. The masks create shadowed area with steps or structures on the film.

Before the deposition, a single crystal MgO(001) substrate was cleaned in an ultrasonic bath in acetone and isopropanol alcohol for a few minutes respectively,

then rinsed with ionised water. The substrate was placed on a sample holder and was loaded into the load-lock chamber. After the pressure recovered to at least $1.0x10^{-5}$ Pa, the sample holder was transferred to the main chamber. *In-situ* substrate annealing was then performed at 600°C for 1 hour. All these procedures were employed to minimise any residual contaminations and impurities on the substrate, which prevent epitaxial growth.

In the main MBE chamber, multiple materials were deposited on the substrate in this project. Both e-guns were used to grow the desired multilayers. A filament of an e-gun was used to heat one source in a crucible at one time. When the source was heated to its molten state, source material was evaporated. The deposition rate was monitored by a calibrated thickness monitor. Evaporated molecules were deposited on the substrate held above the source to form a film. The growth process was carried under a vacuum between $4x10^{-7}$ Pa and $4x10^{-8}$ Pa. Growth conditions of each layer were dependent strongly on molecule size, lattice constants and texture of the substrate and the layer underneath. During the deposition, RHEED was used to observe whether the growth of the film was epitaxial, polycrystalline or amorphous. The crystalline nature of a multilayer structure depends on the matching of the lattices between the two layers and is enhanced when they match precisely. A mismatch between lattices results in strain between the layers and can lead to dislocations [112].

4.4 Film Details

The Heusler alloy Co_2FeSi was first selected for study as it has been found to exhibit exchange coupling with Ir/Mn. However, island growth was observed in the samples which will be discussed in a later chapter, the Heusler alloy $Co_2FeAl_{0.5}Si_{0.5}$ was then selected. $Co_2FeAl_{0.5}Si_{0.5}$ film has been found to have large TMR ratio in an MTJ at room temperature. Tezuka *et al*. reported a tunnel magnetoresistance (TMR) ratio 76% at room temperature using *B*2 ordered $Co_2FeAl_{0.5}Si_{0.5}$ films for the bottom electrode and AlO_x amorphous barrier where the films were deposited using MBE from a single stoichiometrically optimised target [112].

Both the HiTUS and MBE systems used in York were used for $Co_2FeAl_{0.5}Si_{0.5}$ film deposition using a Heusler alloy target with optimised composition. Films grown by HiTUS exhibited little or no structural ordering before annealing, and

those by MBE exhibited a mixed structure of the *B*2 and $L2_1$ phases. After annealing, higher crystalline ordering was achieved as detailed in section 5.8.

After ordered structures were formed, HiTUS grown films were observed to have a large variation in crystallographic orientation with [100], [111] and [112] projections out of plane of the film. This is due to the initial nano-crystalline nucleation sites in the as-deposited matrix [113]. With a layer-by-layer crystallisation mechanism the films are expected to have preferential crystalline planes which were found to be the [112] surface orientation.

Co_2FeSi and $Co_2FeAl_{0.5}Si_{0.5}$ were deposited on a MgO substrates using the HiTUS and annealed at 600°C for 1 hour. To check the ordering of the films, XRD 2θ scans were performed and the scan results are shown in Figure 4. 5. The *B*2 structure was observed in both samples, however some $L2_1$ structure only observed in Co_2FeSi sample. From Figure 4.5 it clearly shows the principle peaks for both Co_2FeSi and $Co_2FeAl_{0.5}Si_{0.5}$ are at ~45°. However the $L2_1$ ordering which should appears at ~28° does not show with $Co_2FeAl_{0.5}Si_{0.5}$ film, moreover the $L2_1$ peak for Co_2FeSi film is weak which means there are only some $L2_1$ ordering formed in the Co_2FeSi film. In contrary, *B*2 ordering appears ~32° and further confirm the *B*2 ordering at ~65°. In conclusion, the Co_2FeSi film have mainly *B*2 and some $L2_1$ ordering and $Co_2FeAl_{0.5}Si_{0.5}$ film has only *B*2 ordering.

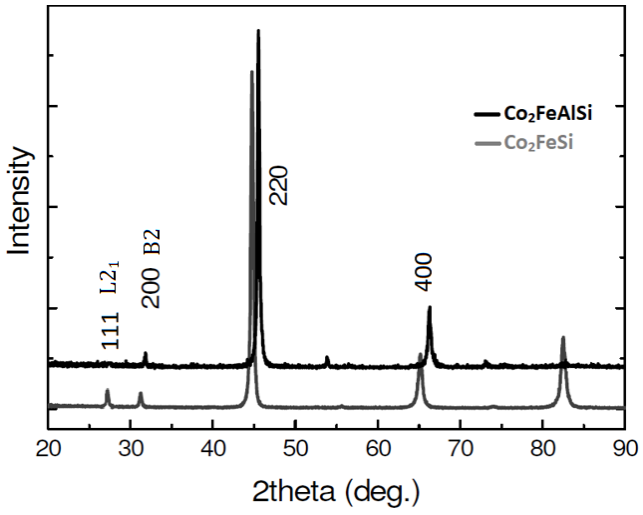

Figure 4. 5 XRD 2**θ** scan for $L2_1$ ordered $Co_2FeAl_{0.5}Si_{0.5}$ and *B*2 ordered Co_2FeSil Heusler alloys.

SEM with EDX was then used to check the samples' composition. The EDX full scale counts are shown in Table 4. **1**. It clearly shows that the HiTUS growth $Co_2FeAl_{0.5}Si_{0.5}$ sample has no Al element. It may because the Al sinks while the target is at molten state. Therefore, MBE was introduced and used to grow $Co_2FeAl_{0.5}Si_{0.5}$

samples in the later part of this study.

	Co	Fe	Al	Si
Co_2FeSi	157	133	0	56
$Co_2FeAl_{0.5}Si_{0.5}$	153	131	0	20

Table 4. 1 EDX composition counts for Co_2FeSi and $Co_2FeAl_{0.5}Si_{0.5}$ sample.

From Figure 4. 6, it is clear that the $Co_2FeAl_{0.5}Si_{0.5}$ source has a higher count of Si than that of Al. Surprisingly, the MBE grown $Co_2FeAl_{0.5}Si_{0.5}$ sample shows a similar count of Al and Si. This could be due to a phase segregation of $Co_2FeAl_{0.5}Si_{0.5}$ in the crucible due to cycles of melting.

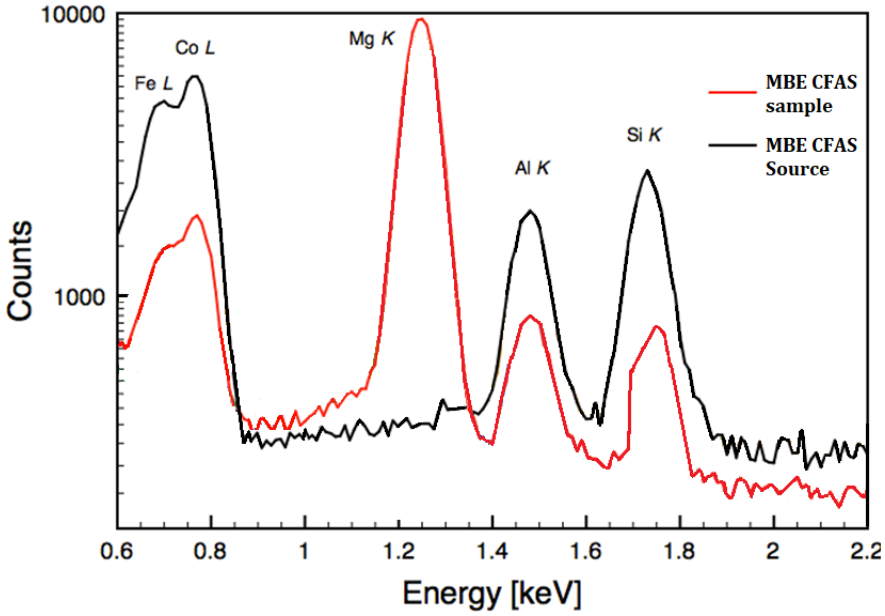

Figure 4. 6 EDX of MBE $Co_2FeAl_{0.5}Si_{0.5}$ source and MBE growth $Co_2FeAl_{0.5}Si_{0.5}$ film.

Buffer layer/ under-layer is needed for GMR devices, therefore the Cr/Ag dual seed layer is introduced. The reasons of choosing Cr/Ag dual seed layer is as follow.

Cr is aimed to provide a very smooth interface and surface which is also known to grow epitaxially on MgO substrate. However, the resistivity of Cr is 13μΩcm which is not low enough for acting as a lead electrode in GMR devices. Thus, Ag is introduced.

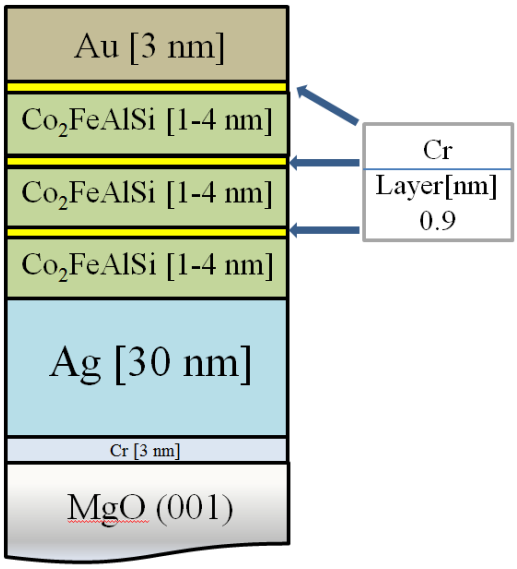

Figure 4.7 Schematic diagram of film structure.

The resistivity of Ag is 1.6μΩcm which is low enough for acting as the lead electrode [10]. Moreover, Ag has good lattice matching with $Co_2FeAl_{0.5}Si_{0.5}$ (<1.5%) which provides a smooth interface and surface for the $Co_2FeAl_{0.5}Si_{0.5}$ layer. Thus, it is easier to grow layers epitaxially, e.g. (100)[100] $Co_2FeAl_{0.5}Si_{0.5}$/(100)[100] Ag/(100)[100] Cr/(100)[100] MgO substrate. The thickness of Ag is required to be ≥30 nm since Cr tends to diffuse through the Ag layer if it is ≤30 nm [114].

4.5 Atomic Force Microscopy

A film thickness calibration is needed if there are any changes in the e-guns source in the MBE. A tooling factor is then calculated by comparing the actual thickness measured with the designed thickness. In this study, film thickness was measured using an atomic force microscope (AFM). AFM was first developed in 1986, Binning *et al.* used an ultra-small probe tip at the end of a cantilever [115]. In the following year, Wickramsinghe *et al.* introduced a vibrating cantilever technique and a light-lever mechanism [116]. The York JEOL JSPM-5200 is a multi-purpose, high resolution scanning probe microscope (SPM). It can be operated as an AFM. The standard AFM can measure critical dimensions and surface roughness 3 dimensionally. A patented drift-free stage is implemented to provide an extremely stable imaging platform.

AFM tapping mode was used in this measurement as it did not damage the surface. A layer of desired material was deposited onto a Si substrate with a stripe mark at the centre as shown in Figure 4.7. The stripe was removed after deposition, leaving a step in the film. The step was then measured by the AFM. Once the thickness of the layer was obtained, it was then compared to the designed thickness and converted as a tooling factor in the thickness monitor in the MBE system.

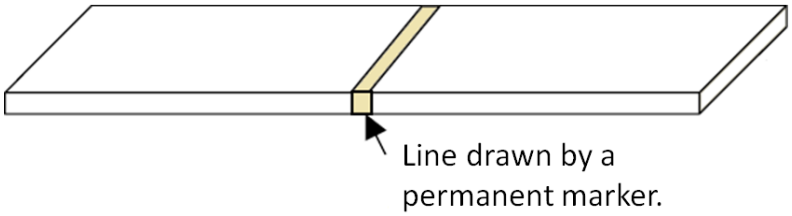

Figure 4.8 Schematic diagram of the sample measured.

4.6 Reflected High Energy Electron Diffraction

RHEED is usually used for investigating surface morphology during thin film growth in an UHV environment. The Eiko HDH-10000 MBE has an integrated RHEED system. By utilising the diffracted electrons from surface atoms, the arrangement of surface atoms and the quality of crystallinity of the grown layer can both be observed. When electrons are emitted from the RHEED gun, they strike the surface of the grown thin film layer or substrate. Then the diffracted electrons are reflected onto the fluorescent screen, forming a diffraction pattern and specular reflection. The nature of the pattern indicates the surface quality. A smooth layer by layer growth surface gives a 'streaky' RHEED pattern while an island growth or rough surface gives a 'spotty' pattern and rings are the indication of polycrystalline surface [117]. By knowing the quality of the grown thin films, decision of further investigation on such sample would be considered.

4.7 X-ray Diffraction

There are several ways to study crystalline materials such as X-ray diffractometer (XRD), and transmission electron microscope (TEM). Both XRD and TEM can be used to determine the size and shape of a unit cell, lattice spacing, the crystalline state of the atoms of the material and the lattice strain. It is more difficult to observe lattice strain in TEM due to sample preparation. Comparatively, XRD is easier to operate and less time consuming. Furthermore, in the XRD X-rays diffracted across a large area and an individual spot can be scanned with a high resolution and studied quantitatively.

X-rays were discovered in 1895 by W. C. Roentgen [119] and X-ray diffraction in a crystal was discovered in 1912 by Friedrich, Knipping and Laue [120]. Since then XRD has been one of the most important characterisation tools used in the study of material's structure. The size of a unit cell, the lattice spacing and the crystalline state of the atoms of the material can be determined and calculated by using Bragg's Law [22]:

$$n\lambda = 2d_{hkl}sin\theta \tag{4.3}$$

$$d = \sqrt{\frac{a^2}{h^2 + k^2 + l^2}} \tag{4.4}$$

where λ is the X-ray wavelength, θ is the angle between the incident beam and the crystal planes, d is the lattice spacing, a is the lattice constant of the material and h,k,l are the Miller indices for cubic crystals , thus equation 4.4 only applies to cubic crystal [22].

The XRD measurements were carried out with two XRD machines, a Rigaku SmartLab XRD and the XRD sysem in the photon factory of KEK in Japan. The Rigaku XRD is equipped with a high intensity 9 kW rotating anode X-ray generator. The maximum voltage and current can reach at 45 kV and 200 mA respectively. The stability of the voltage and current are $\pm 0.005\%$ for a 10% input power variation [121]. This XRD system provides high resolution $\theta - 2\theta$ scans due to its a high resolution ϑ – ϑ goniometer. The ϑ – ϑ goniometer enables the X-ray source and detector to be positioned with an accuracy of 0.001° step size which gives crystallographic information of the sample from the plane perpendicular to the sample normal [121].

A pole figure scan was performed in this study to analyse the sample over a large area. To obtain a full scan, the 2θ angle has to be fixed at the desired angle, then data is collected by changing either angle α or angle β, where α is the tilt angle from the sample surface normal direction and β is the angle around the sample surface normal as shown in Figure 4. 9.

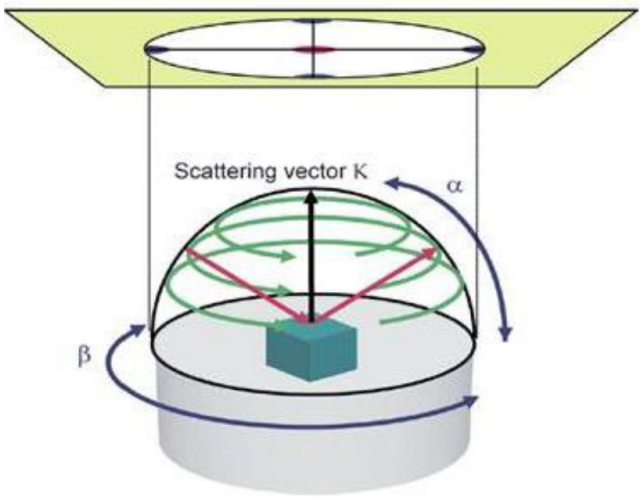

Figure 4. 9 Schematic of pole figure scan configuration [122].

As the $Co_2FeAl_{0.5}Si_{0.5}$/Cr trilayer has overlapping crystallographic data that the Rigaku XRD is not able to identify, these samples were sent to the photon factory at KEK in Japan. The XRD system at KEK in Japan uses synchrotron radiation with energy 6-20 keV. This XRD system has an imaging plate, Weissenberg camera, has a radius of 191.3 mm which can be operated between 10 K and 1000 K and hydrostatic pressure up to 50 GPa.

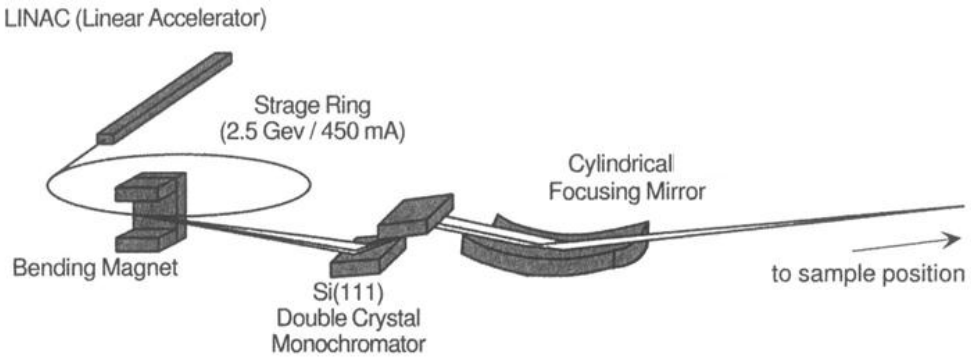

Figure 4.9

Figure 4. 10 Schematic diagram of how the XRD is operated.

Figure 4. 10 Shows how the X-ray beam is made monochromic and focused before hitting the sample. The X-rays are monochromic using a Si (111) double flat monochromater and focused at the sample position by a Rh coated Si mirror. Both reflected and transmitted diffracted X-rays are obtained simultaneously and sensed by the imaging plate which has large dynamic range and larger detector size than a camera [122].

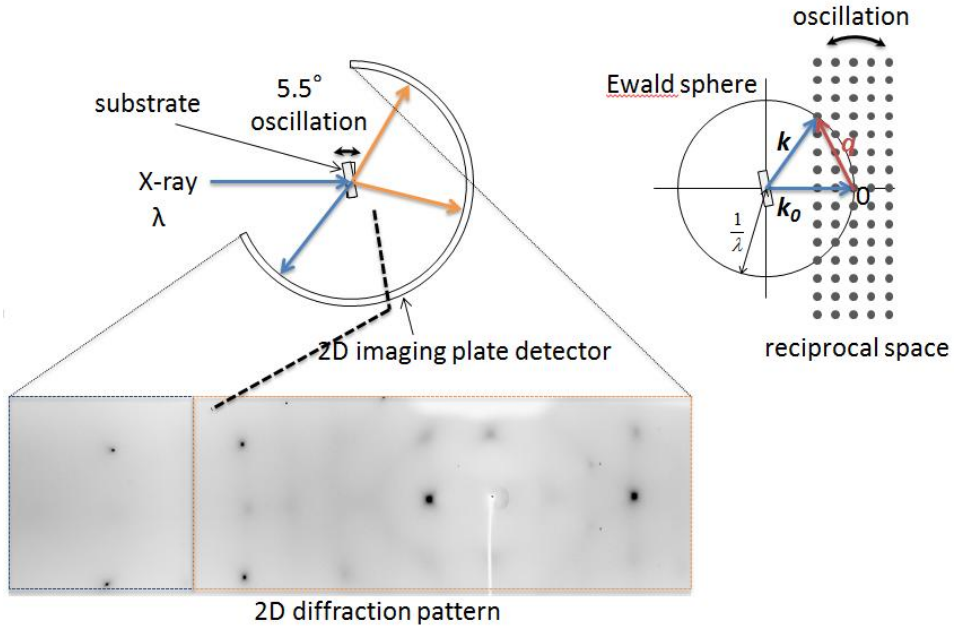

Figure 4.11 Schematic diagram of how the diffracted pattern is created.

The diffracted X-ray beam corresponds to the reciprocal lattice vector which can be understood from:

$$k_g - k_0 = g_{hkl} \tag{4.5}$$

where k_g and k_o are the wave vectors of the scattered and incident X-ray beams respectively and g_{hkl} is the reciprocal lattice vector. By re-writing Bragg's law:

$$2k_0 g_{hkl} sin\theta = {g_{hkl}}^2 \tag{4.6}$$

where $k_0=2\pi/\lambda$, $d_{hkl}= 2\pi/g_{hkl}$ [22].

The diffraction patterns appear on an imaging plate detector and the sample is oscillated during the measurement. When the sample is oscillated in real space, the reciprocal lattice is oscillated around the origin in reciprocal space. The corresponding diffraction spots appear on the 2D imaging plate detector only when the reciprocal lattice points across the surface of Ewald sphere. The Ewald sphere is a geometrical construction used in X-ray crystallography which demonstrates the reciprocal lattice of the crystal [22].

4.8 Transmission Electron Microscopy

Obtaining structural information of materials from XRD is faster and no sample preparation is needed. The benefit from using a JEOL TEM-2011 which has an energy dispersive X-ray spectroscopy (EDS) detector installed that gives a spectrum of the atoms in the material. Therefore, apart from atomic resolution imaging, fundamental compositional information can also be obtained from TEM.

4.8.1 Operation of TEM

The operation of TEM utilises the wave-like properties of electrons which was first proposed by Louis de Broglie in 1925 [123]. Based on de Broglie's theory, the particle momentum can be related to its wavelength, λ, as follows,

$$\lambda = \frac{h}{p} \tag{4.7}$$

where $\boldsymbol{h}$ is Planck constant and $\boldsymbol{p}$ is the momentum. The first electron microscope was proposed by Knoll and Ruska in 1932 [124]. A JEOL TEM-2011 was used in this project and a schematic diagram of the optical arrangement of the microscope is shown in Figure 4.11. Before operating the TEM the sample has to be prepared into a thin specimen, a schematic diagram in section 4.8.3.

The specimen is then placed onto a probe and inserted into the TEM. TEM operates under high vacuum of 10^{-10} mbar, utilising an electron gun to generate electron beam transmit through the specimen. By adjusting lens and apertures, the chemistry and crystallography of the specimen can be accurately determined which makes TEM a very powerful tool for structural material studies.

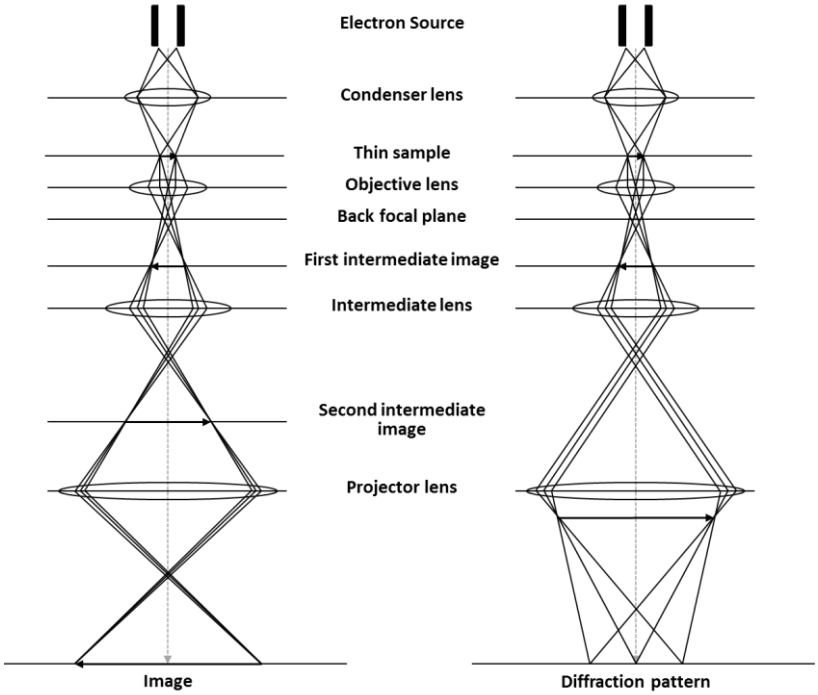

Figure 4.12 Ray diagrams for typical TEM configurations showing mechanism for the formation of images (left) and diffraction patterns (right) [125]

In order to get a good signal out of the specimen, a good electron source is critical. The electron source is a Lanthium hexaboride (LaB_6) filament with a 1μm tip is located at the top of the column which emits electrons through a thermionic process. The electrons are then accelerated through a potential to high energy and equation 4.8 becomes:

$$\lambda = \frac{h}{2m_0 eV^{\frac{1}{2}}} \tag{4.8}$$

However, when the accelerating voltage is at 200keV or above, electron would travel at greater than half the speed of light. Therefore equation 4.9 is modified to give

$$\lambda = \frac{h}{\left[2m_0 eV\left(1 + \frac{eV}{2m_0 c^2}\right)\right]^{\frac{1}{2}}} \tag{4.9}$$

Once accelerated into the microscope column the electrons are focused into a small (2-3 μm) coherent electron beam by the condenser lens. By adjusting electromagnetic lenses and apertures, the intensity and spot size of the beam incident on the specimen can be controlled. The size of the beam can then be further

restricted by a user selectable condenser aperture. This condenser aperture removes higher angle electrons from the beam, increasing the uniformity of radiation illuminating the specimen. These apertures can also be used to limit the beam intensity for imaging of specimens that are highly susceptible to beam damage. Then the high energy beam of electrons interacts with the specimen. Electrons are then scattered by nuclei and orbiting electrons, these can be either elastic scattering or inelastic scattering. Both types of scattering can provide information about the specimen. When the specimen is thin and crystalline, elastic scattering is coherent. Coherent elastically scattered electrons contribute to diffraction patterns and in-elastically scattered electrons contribute to provide chemistry and electronic structure information.

To study the elastically scattered electrons, the objective lens takes the electrons emerging from the exit surface of the specimen, disperses them to create a diffraction pattern in the back focal plane and recombines them to form an image in the image plane. There is no energy lost in this process which is the main difference between elastic scattering and inelastic scattering. Inelastic scattering and EDS are discussed in section 4.9.

4.8.2 TEM Cross-sectional Sample Preparation

In order to have sufficient intensity of transmitted electrons to pass through, a thin sample edge (<100 nm) is needed. This procedure is called cross-section preparation. Two stripes of 2 mm width, 4 mm length were cut from the sample and two 3mm width, 4 mm length slices of Si wafer were cut by a diamond saw. These strips were then glued face-to-face on the film side and sandwiched as shown in Figure 4.13.

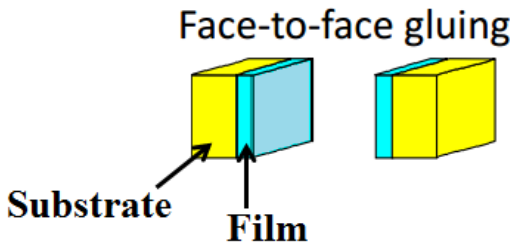

Figure 4.13 TEM specimen preparation.

The plain Si wafer is used to monitor the specimen thickness when the thickness is down to 20-30 μm. The stack was glued with epoxy and resin on a hot

plate. When the glue is set, one side of the specimen is thinned using silicon carbide and diamond papers. During this process, specimen thickness and status was checked by a microscope. When light shines through the specimen with a reddish orange colour, the specimen is 20-30 μm. The specimen was then glued to a copper TEM grid and ion milled as shown in Figure 4.14. The milling was done with Ar ions with energy of 2.5 eV from the above and below at an angle of 6°.

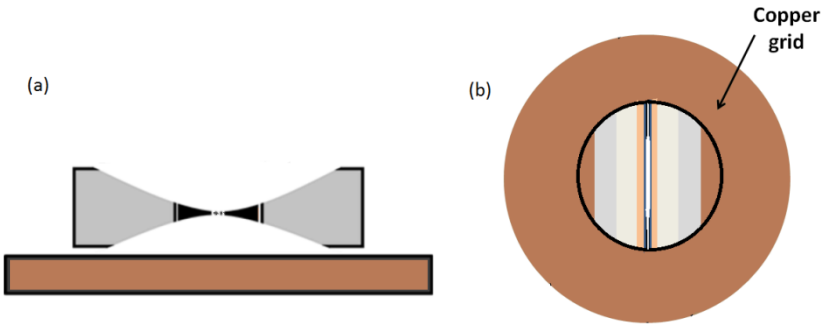

Figure 4.14 Schematic of cross-sectional TEM sample view from (a) the side and (b) below.

A TEM sample is shown in Figure 4.15 which clearly shows the hole, glue, film and substrate. If the sample is too thin then it is usually not possible to obtain such clear image. When the sample is too thick then the image would not show on the screen due to multiple electron scattering.

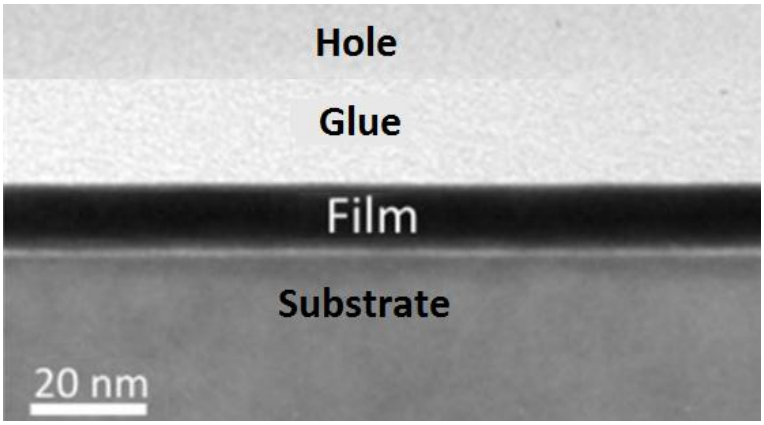

Figure 4.15 An example of sample which is ready for TEM imaging.

4.9 Energy Dispersive Spectroscopy and Inelastic Scattering

The material's structure, phase and crystallographic information can be obtained from elastic scattering of electrons. Apart from elastically scattered electrons, there are in-elastically scattered electrons. Inelastic scattering is always incoherent and when the specimen is thick there will also be backscattered electrons which can also be incoherent as shown in Figure 4.16.

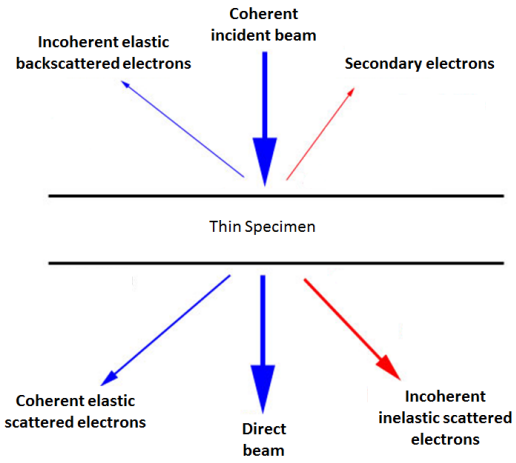

Figure 4.16 Various phenomena that take place during electron interaction with a thin specimen [125]

Usually there are two kind of X-rays produced: characteristic X-rays and Bremsstrahlung X-rays. An EDS detector is one of the applications which utilise characteristic X-rays. Characteristic X-rays result from high-energy electrons of the beam which eject inner shell electrons from atoms in the sample, and the ionized atoms return to their lowest energy states by replacing the missing inner shell electrons by electrons from the outer shells. This process results in either the emission of an X-ray or an Auger electron, whose energy of emission is characteristic of the difference in energy of the two electron shells involved, thereby providing a unique signature to identify the type of atoms present. Sharp peaks corresponding to the characteristic

X-rays emitted by the atoms of the different elements present in the sample will be shown in a EDS spectrum.

4.10 Alternating Gradient Force Magnetometer

An AGFM is a highly sensitive and high resolution with a low noise-base force measurement system, capable of measuring hysteresis properties of samples. It is advantageous to have high sensitivity and mechanical gain.

4.10.1 Theory of AGFM

In the AGFM, a homogenous, well-defined alternating gradient field at an accurately controlled frequency is generated by two high current coils, as shown in Figure 4.17 (a) & (b). And this alternating gradient field and DC variable field are then utilized to exert a periodic force on a magnetic sample. The force is proportional to the magnitude of the gradient field and the magnetisation of the sample. When a magnetic field puts stress on the bimorph, the bimorph changes the stress into an electrical charge which can be detected. As the magnetisation is proportional to the stress, the magnetisation of the sample can then be measured [107].

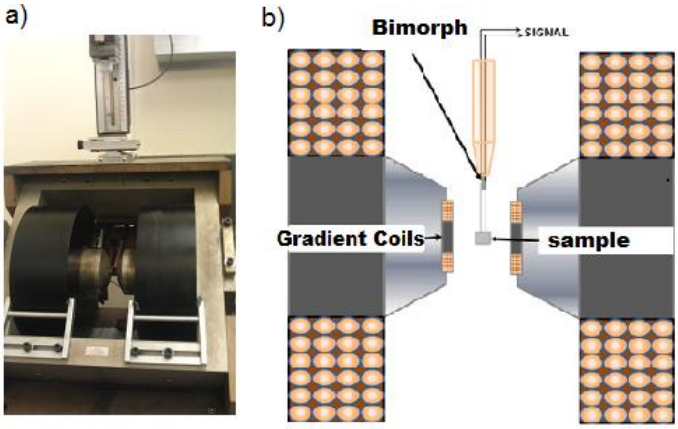

Figure 4.17 a) picture of the actual AGFM; b) Schematic diagram of magnified AGFM with the probe and sample; where A and B are the alternating gradient coils

Before using the AGFM, the sample and probe must be cleaned with isopropanol in an ultra-sonic bath. Making sure the probe and samples are not contaminated, is critical to the reliability for all measurements. The probe must be positioned at the centre of the field so that the field gradient has the largest effect giving the largest signal for detection. After inserting and positioning the probe, a plastic shield was provided to cover up the AGFM as the AGFM is very sensitive to external noise, e.g. mechanical vibration. Once the probe is in place, the AGFM needs to be calibrated and this calibration should be carried out every time before taking any measurement. The program AGFM was generated in the computer, Autofunction from the main menu was selected after the probe was centred in the magnetometer. By pressing the Initial Autotune, the Q factor of the probe was obtained. Then Incremental Autotune was pressed several times which allows the system to tune to adjust the previous tuning more accurately. The field gradient was selected to be 0.1 T/m throughout the whole measurement, as samples which have small coercivity can be demagnetized by applying big field gradient. A typical hysteresis loop can be seen in Figure 4.18.

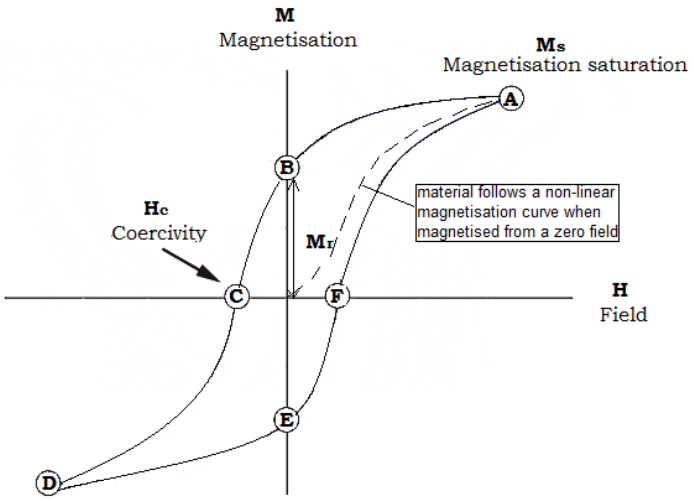

Figure 4.18 Shows a hysteresis loop of the magnetisation of a ferromagnet as a function of applied field.

4.10.2 AGFM Probe

In the AGFM, the sample is attached onto a 3mm x 3mm square glass with two quartz legs which are attached to a bimorph, which is called as a probe. This sensitive quartz probe was used to convert stresses on magnetic samples exerted from the magnetic field into readings of the sample magnetisation. The probe is very delicate and can be broken easily due to the fine quartz legs and size of the square glass.

The probe was built as shown in Figure 4.19 (a) & (b). Gloves must be worn at all times to avoid contamination of the probe. The Q-factor of the probe was used to carry out all the measurements, the average value is 23.14. The Q factor is a factor determining the sensitivity of the resonance peak; therefore, Q must be large enough to enable detection of the moment of small or weakly magnetic samples [126].

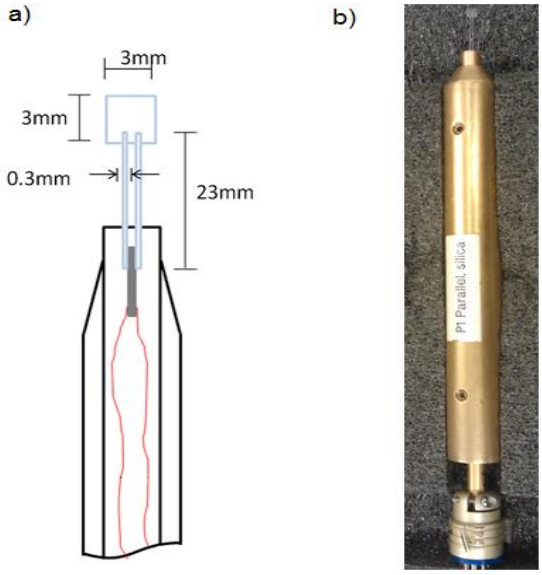

Figure 4.19 (a) Schematic diagram of the sensitive quartz probe;
(b) picture of the actual probe

4.11 Vibrating Sample Magnetometer

A vibrating sample magnetometer (VSM) is a system with a different measurement principle than the AGFM. A VSM is based upon Faraday's law of electromagnetic induction. VSM is first described by Foner in 1959 [127]. Faraday's law of electromagnetic induction states that a change in magnetic flux induces a potential difference across a conductor where the induced e.m.f. is proportional to the rate of change of the field. In a VSM, a magnetic sample is placed on a sample rod and positioned with the holder between two coils (electromagnet) as shown in Figure 4.20. The electromagnet provides an external magnet field while the system physically vibrates the sample which causes a change in magnetic flux from the sample.

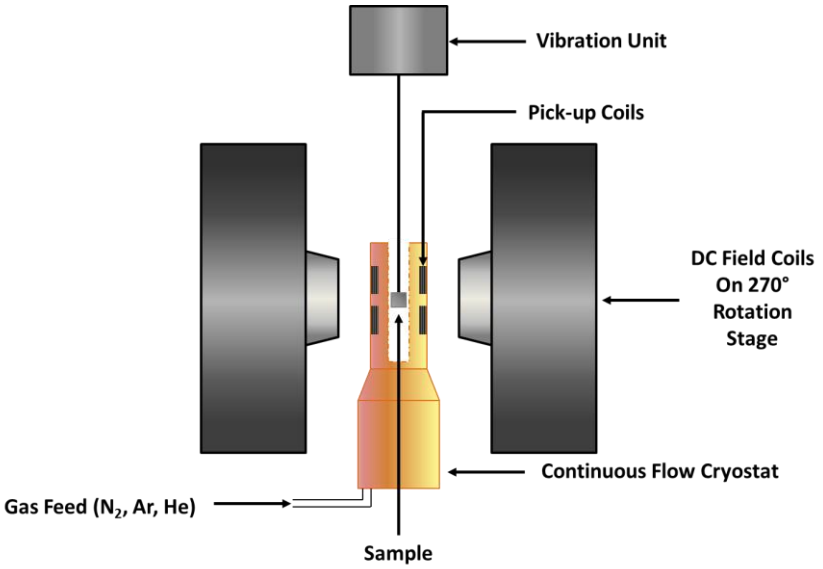

Figure 4.20 Schematic diagram of a VSM

This change in magnetic flux gives a voltage to be measured. The voltage induced in the pick-up coil is measured using a lock-in amplifier. The lock-in amplifier gives a DC output which is proportional to the amplitude of the voltage induced which can be calibrated to give a reading of the moment of the sample. Then a hysteresis loop can be plotted when the VSM is calibrated with a sample of known magnetisation saturation value.

In this project, calibration of both H and moment were carried out before taking measurement to ensure accuracy. H was first calibrated. Two reference points were compared to the reading from an external standard Bell 9900 Gaussmeter: fixed secondary magnetic field and zero-field. Both reference points were tuned to have the same reading with the external Gaussmeter, H was well calibrated. The moment calibration was traditionally measured with a nickel calibration sample due to its low saturation magnetic field. But a calibration should be done with a sample which has a similar moment. Hence a Pauli paramagnet is more suitable to use as a calibration sample in this project. A Palladium foil with the same size and thickness was used as a Pauli paramagnet. The foil was cleaned then was placed between the coils with a sample rod, and then the position of the foil was adjusted to achieve the centred position. When the foil is centred between the coils, the moment calibration is done. Low temperature angular dependence measurements were then carried out in the ADE model 10 VSM.

The main noise of the ADE model 10 VSM is $\sim 5 \times 10^{-3}$ emu which is created from the pick-up coils. When the signal is picked up by the coils, it was then filtered by a digital signal processing lock-in amplifier. With 1 second averaging time, the noise is reduced to 5×10^{-6} emu. Vibrations generated from pumps and magnet are damped by 4 rubber shock absorbers at the bottom of the legs of the VSM. There is another source of noise from the sample rod. It was found that there is a build-up static charge on the sample rod. An anti-static fan was set up behind the rotating magnetic and blown directing to the sample rod. By removing or attenuating all the noises, the noise can reduce to 1×10^{-6}emu.

Since the advantages of using VSM comparing to an AGFM are that

there is no gradient field in the VSM so there will be no demagnetising effect, field angle and temperature dependence measurements can be carried out easily, a rigid sample rod is used in VSM instead of a delicate sample holder used in AGFM. In this project, the sample needs to take measurement at a low temperature (193K) which the AGFM cannot achieve. In this case, a low temperature source was implemented. Liquid nitrogen was constantly applying to the sample holder area to maintain the desired low temperature.

4.12 The York Model Protocol

The York Model of exchange bias was described in detail by O'Grady et al. in 2010 [128], part of this model are based on Fulcomer and Charaps' work which described that AF layer is made of independent single domain AF grains [129, 130]. The York Model describes the behaviour of polycrystalline thin films with grain sizes in the range 5-15nm [128]. The model has also been adapted to describe epitaxial single crystal films. Strong domain wall pinning leads to domain rotation rather than domain wall motion increasing the exchange bias.

In a previous study of Sagar et *al.*, the effect of bias voltage (V_B) in the York model for exchange bias is shown in Figure 4.**21** [132]. This shows that it is possible to control H_{ex} by controlling the grain size of the sample. This theory agrees with a previously published material on conventional magnetic materials [128].

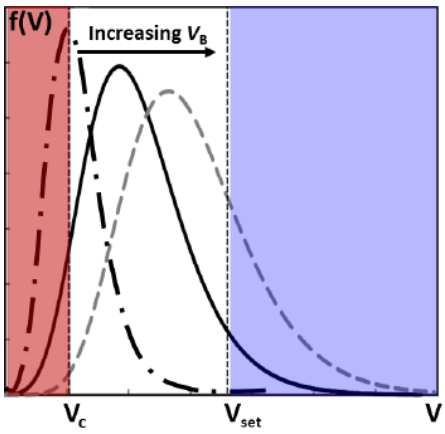

Figure 4. 21 Schematic diagram of effect of V_B in the York model for exchange bias where V is the volume of a grain in the AF layer [132].

In order to observe the exchange bias behaviour, the film has to be cooled through its Néel temperature. If a magnetic field is applied to reverse the F layer, the spins in the AF layer pin the F layer at the interface leading to a shift of the hysteresis loop. The displacement between the origin and the centre of the loop is known as exchange bias, H_{ex}, as shown in Figure 4. 22

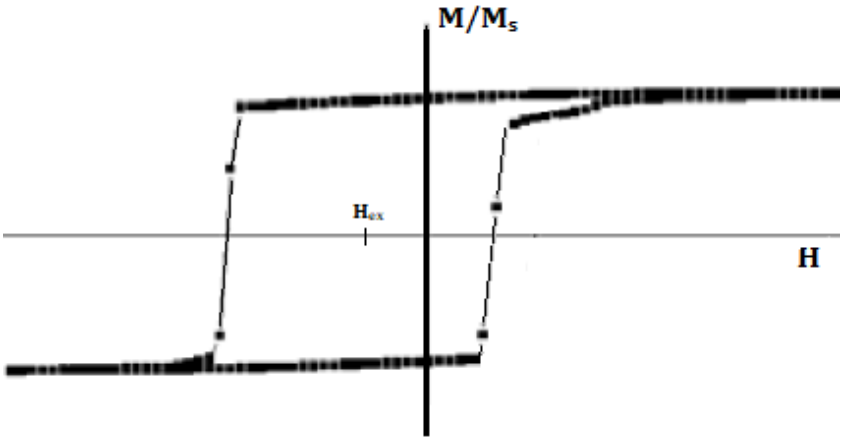

Figure 4. 22 A typical Hysteresis loop of polycrystalline films with exchange bias.

The AF layer in this study is Cr and its Néel temperature, T_N, is 308K. The sample was first set under a saturating applied field of 1kOe at 303K for 30mins, then field cooled to 193K. A low temperature hysteresis loop is then measured. All samples in this study are all set as described to obtain hysteresis loops.

To analyse the anisotropy of the sample, M_r and remanent polar plots are needed. The VSM computer software runs the set measurement recipe as mentioned. Once the desired temperature is achieved, 36 measurements will be taken automatically which is 360° with a 10° step interval for one sample.

4.13 Error and Calibration

The TEM was calibrated by the JEOL engineer and the accuracy of images at 100kV is 0.1nm. The field resolution of the Model 10 VSM is less than $\pm$5Oe in 10kOe and $\pm$10Oe in 1kOe. All hysteresis loops in this study were plotted M/M_s against applied field to avoid any consideration of the sample volume. The typical error in M/M_s for the samples studied is about 2%. The applied field is calibrated by a Hall probe. The error on surface area measurements is $\pm$ 0.25%.

Chapter 5

Seed Layers and Film Quality

5.1 Selection of Applied Bias Voltage

In chapter 3, two Heusler alloys were introduced with XYZ and X_2YZ compositions as half and full Heusler alloys respectively. Both are promising materials for spintronics but the full Heusler alloy films with half-metallic properties, Co_2FeSi and $Co_2FeAl_{0.5}Si_{0.5}$, are the focus of this study. The reason of choosing these Heusler alloys and seed layers are discussed in section 4.4. The relationship between grain sizes and magnetic properties of the samples are discussed in this section.

5.1.1 Sample Fabrication

HiTUS was used to grow all Co_2FeSi samples in this study. The film structure was Co_2FeSi (20nm)/Ru (3nm) which were deposited onto single crystal MgO substrates, as well as carbon coated copper TEM grids. The films were grown with a set of bias voltage of 250V, 500V, 750V and 850V. After the growth, samples and TEM grids were all annealed at 300°C for 3 hours.

5.1.2 Grain Size Analysis

The grain size analysis was done using a Zeiss particle size analyser. The grain sizes of each film were found to fit a lognormal distribution.

$$f(D)dD = \frac{1}{\sqrt{2\pi}\sigma_{\ln D}D}\exp\left(\frac{-\left((lnD) - \bar{x}_{\ln D}\right)}{2\sigma_{lnD}}\right)$$

where D is the measured particle diameter, $\sigma_{\ln D}$ and $\bar{x}_{\ln D}$ are the standard deviation and the mean value of $\ln D$ [7]. The lognormal distribution of the

grain size diameter f(D)dD was plotted as a function of grain diameter as shown in Figure 5. 1. More than 400 grains were counted and a median grain diameter, D_m, and standard deviation, σ, were obtained from the Zeiss computer program.

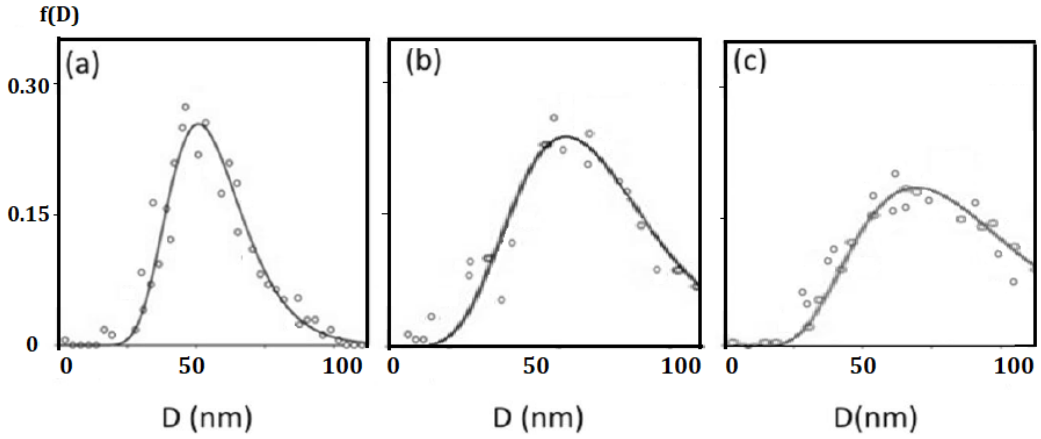

Figure 5. 1 Distribution of grain sizes and corresponding lognormal fits for films grown with V_B (a) 250V, (b) 500V and (c) 750V.

The summary of the grain size analysis is shown in Table 5. 1. It shows that the median grain size of the samples increases with V_B and films grown with 850V has the highest D_m of 135±0.2nm. This trend agrees with a previous study on Co_2MnSi reported by Hirohata et *al*. In that report, it shows that the increase of D_m is due to Si segregation.

V_B (V)	D_m (±0.2nm)	σ (±0.02)
250	59	0.28
500	75	0.34
750	79	0.36
850	135	0.38

Table 5. 1 Summary of the measured grain size distribution.

5.1.3 Magnetic Characterisation

In this section, all hysteresis loops described were measured using the AGFM as described in section 4.10. Hysteresis loops are measured for all samples after annealing for 3 hours. These measurements allow direct comparisons of magnetic properties with different applied V_B. Measurements are mostly shown with normalised moment, M_r/M_s. Table 5. 2 shows magnetic moments and coercivities for the films as a function of bias voltage. The magnetic moment was found to increase with V_B and the largest moment was found in the film grown with 850V.

V_B (V)	M_s ($\pm$10% emu/cm^3)	M_r/M_s ($\pm$ 2%)	H_c (Oe) ($\pm$ 5%)
250	302	0.89	39
500	380	0.93	58
750	440	0.96	80
850	668	0.41	18

Table 5. 2 Summary of magnetic data for Co_2FeSi thin films.

It is shown that H_c increases with increasing V_B except for films grown with 850V. The squareness of the film grown with 850V is 0.41 which is the lowest among all samples. For spintronic devices where fast, coherent, magnetisation reversal is required, a low coercivity is essential, thus applied bias voltage for film growth in HiTUS is set to be 850V.

5.2 Optimisation of Heusler alloy film with a Cr/Ag seed layer

In this section the effects of using a dual seed layer of Cr/Ag on polycrystalline Co_2FeSi and epitaxial $Co_2FeAl_{0.5}Si_{0.5}$ thin films are discussed.

Seed layers were deposited between the substrate and the Heusler

alloy layer. Such a system with a seed layer could find a use in GMR devices. Different thicknesses of the Cr layer were investigated to achieve low coercivity (H_c) and large saturation magnetisation (M_s). Furthermore, it was found that the Ag layer forms islands initially which affects the following layers. Therefore the other purpose of introducing the Cr layer is to achieve a flat surface for the following ferromagnetic layers.

5.2.1 Sample Fabrication of Co_2FeSi

An ordered and flat surface is important for the structural properties of the thin film deposited. Seed layers can provide an ordered and flat surface and also induce the desired crystallographic orientation, such as grain size and grain segregation of the subsequent layers. A good lattice match between the seed layer and the subsequent layer is very important to achieve the desired goal. In 2012 Sagar *et al.* [131] reported the use of several seed layers on a Co_2FeSi film. It was shown that a Ag seed layer improves the properties of a Co_2FeSi film by changing the magnetisation reversal process and giving a low coercivity (H_c) of 10 Oe compared to a previous value of 300 Oe [132]. It was also shown that the Ag layer forms islands and a quasi-continuum on which the Co_2FeSi layer grows [131]. The lattice constant of Si, Ag and Co_2FeSi are 5.43 Å, 4.09 Å and 5.64 Å respectively [71]. The island formation at the interface between the substrate and Ag layer is shown in Figure 5.2 (a). A SiO_x layer with Ag islands formation is likely the result of the Volmer-Weber process [133]. The main reason of this phenomenon to occur is the lattice mismatch between the substrate oxide layer and the Ag layer which is likely to be Ag repellent, analogue to a surface tension effect in a liquid. This island growth affects the texture of the following layer which is shown in the

cross-sectional TEM image shown in Figure 5.2 (b). The Ag layer was grown directly on a Si (100) substrate. However an oxide layer was observed between Ag layer and substrate. The image clearly shows columnar growth with the crystal planes of the Ag at an angle to the perpendicular.

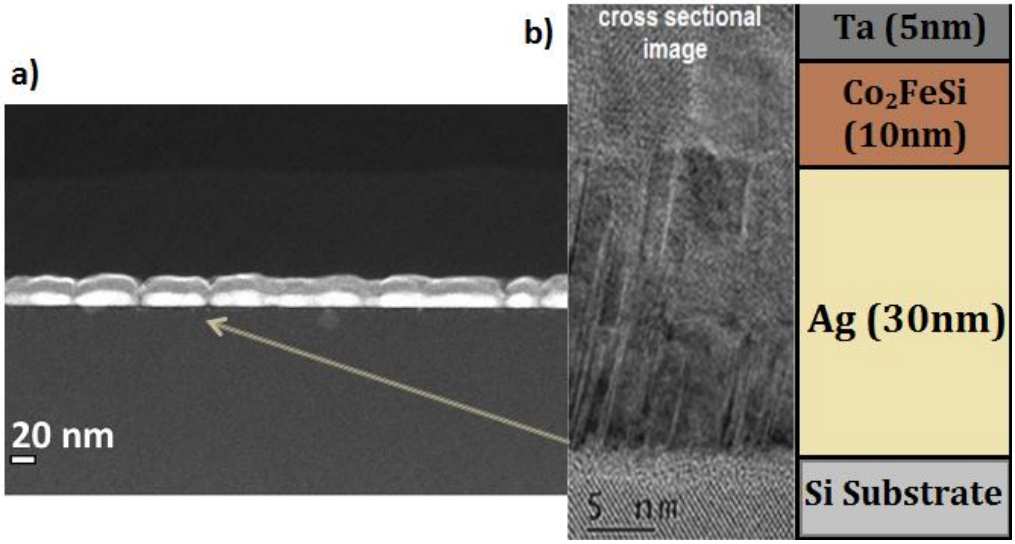

Figure 5.2 (a) Island growth of Ag layer; (b) Column tilt angle growth with Ag seed layer on Si (100) substrate of TEM images.

It was reported that the Ag islands formation leads to the columnar growth in this system minimises the grain sizes of the film. The reduction of grain sizes of the film varies the coercivity and also the domain wall pinning mechanism [131]. In order to avoid this columnar growth, a layer with good adhesion and small lattice mismatch to the substrate is required. Ag was chosen as it can also be used as a contact electrode in device applications.

The objective of this part of study is to avoid the island growth structure shown in Figure 5.2 and to identify the optimum annealing time and thickness of the Ag seed layer in order to optimise the magnetic properties of the Heusler alloy. The films studied were deposited using the HiTUS. Details of the operation procedures were described in section 4.2. An Ar^{+} plasma was generated by an RF field at $3x10^{-1}$ Pa and steered onto the target with bias

voltage of 850V [108, 109, 128].

A total of 3 samples were sputtered with a structure Cr (t_{Cr})/Ag (t_{Ag})/Co_2FeSi (20 nm)/Ta (3 nm) on a Si (001) substrate, where t_{Cr} =1.5, 3 and 4.5 nm and t_{Ag} = 6, 15, 30 nm. The set range of Cr thickness is 5-15 times of one atomic layer of Cr which is necessary to obtain the flatness. For device application, it would require a film thickness of greater than 50 nm and Ag is consider to act as a barrier to Cr diffusion, thus the set range of t_{Ag} is larger than that of Cr. The samples were capped with 3 nm of Ta to prevent oxidation. Samples were then post annealed in an Ar^+-rich environment at 300°C for up to three hours. Bright field images of cross-sectional TEM samples were obtained using a JEOL JEM-2011 TEM to compare the difference between using the Ag seed layer and the dual Cr/Ag seed layer.

5.2.2 Properties of Co_2FeSi Film

The prevention of Ag island growth with a Cr under-layer is confirmed by the TEM images as shown in Figure 5. 3. For a Cr thickness of 1.5 nm, non-uniform growth of the Cr layer was observed which did not provide a flat surface. However, a 3nm thick layer of Cr shows a desirable result. There is a thin layer (~1nm) below the Cr layer which was assumed to be SiO_2.

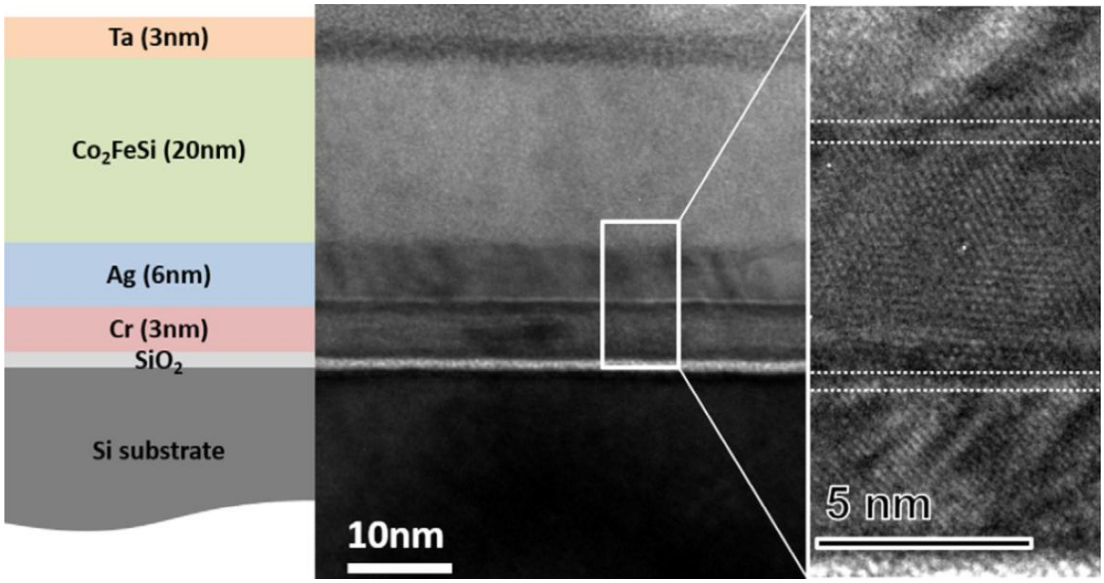

Figure 5. 3 TEM image of sample with Cr under-layer.

The TEM image in Figure 5. 3 clearly shows that the presence of the Cr layer has prevented Ag island growth formation and gives a peak to peak roughness of < 1nm. No columnar growth was observed.

5.2.3 Magnetic Measurements for Co_2FeSi

Magnetisation curves were measured using the AGFM at room temperature before and after annealing samples of Co_2FeSi with and without seed layers. Values of coercivity (H_c), remanence (M_r) and saturation magnetisation (M_s) were obtained. Low values of H_c (<100 Oe) were obtained for all samples which remained unchanged with increased annealing time. A low H_c is required for low field magnetisation reversal. All data shown were normalised for direct comparison.

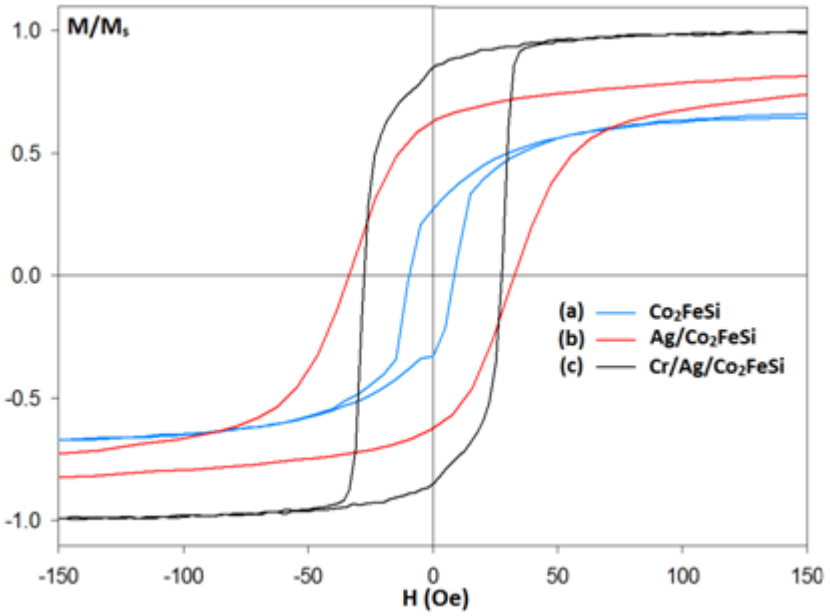

Figure 5.4 Hysteresis loops of HiTUS grown polycrystalline samples on Si substrate after annealing.

Figure 5.4 (a) shows the hysteresis loop of the sample without a seed layer (b) sample with Ag seed layer and (c) sample with dual Cr/Ag seed layer. All samples were grown under the same conditions. The parameters from the loops and the grain size data are shown in Table 5. 3.

	H_c (±2% Oe)	D_m (±2 nm)	σ (±0.02)	M_s (±2% emu/cm^3)	M_r/M_s
No seed layer	14.3	135	0.36	634	0.41
Ag seed layer	33.2	100	0.40	950	0.66
Ag/Cr seed layers	29.4	40	0.33	1010	0.86

Table 5. 3 A summary of magnetic properties of the loops.

For the sample grown without a seed layer, the coercivity is very low (~14 Oe) but the squareness is also very low so that the M_r/M_s is 0.41. It is shown in Table 5.3 that the sample without a seed layer has the largest grains. The coercivity is low because the grains are so large that they divide into

several magnetic domains. There are domain walls inside each grain, the domain walls move easily and generally pin at the grain boundaries. The grains are so large (>100 nm) that the intergranular exchange coupling is strong so that the domain walls can easily cross the grain boundaries. In the sample without seed layer the substrate is almost atomically smooth so that there is little or no pinning at the substrate which leads to the low coercivity. Likewise the squareness is low because the domain walls relax easily when the applied field is removed.

In the case of the sample grown on a Ag seed layer, the island growth creates a rough surface as shown in Figure 5.2 that leads to numerous pinning sites. Therefore the coercivity is higher than that of sample without a seed layer and squareness also increases as relaxation of the domain wall will not occur so easily.

With the dual Cr/Ag seed layer the Co_2FeSi is grown on a much smoother surface and the grain size is significantly reduced (D_m=29.4 nm) so that there will be both single and multidomain grains in the film. Figure 5.3 shows that the Cr layer has created a smooth surface on which there will be less pinning sites at the Ag layer giving a lower coercivity. However the grain size of this sample is small < 40 nm, putting the grains mostly at the single domain size involving reversal over an anisotropic energy barrier. There is also some strong exchange coupling between grains. After the sample is saturated, the single domain grains stay magnetised and, being exchange coupled to the multi-domain grains, tends to keeps them aligned giving a high remanence thus a higher squareness and moderate coercivity. As shown in Figure 5.3 there is some degree of segregation in the films which could be due to oxidised Si either in the powder compound target or occurring during

deposition. However such segregation is not observed in films without a Ag seed layer. Hence the most likely cause of the segregated structure is the island growth of the Ag layer. Voids between the islands will transmit through to the Co_2FeSi and hence the white lines seen in Figure 5.5 are probably voids. Each void does not surround a single grain as can be seen by the variation in contrast within each area. However these voids will limit the RKKY coupling between these regimes. Hence the concept of the reversal being dominated by domain wall processes in exchange coupled granular films remains valid.

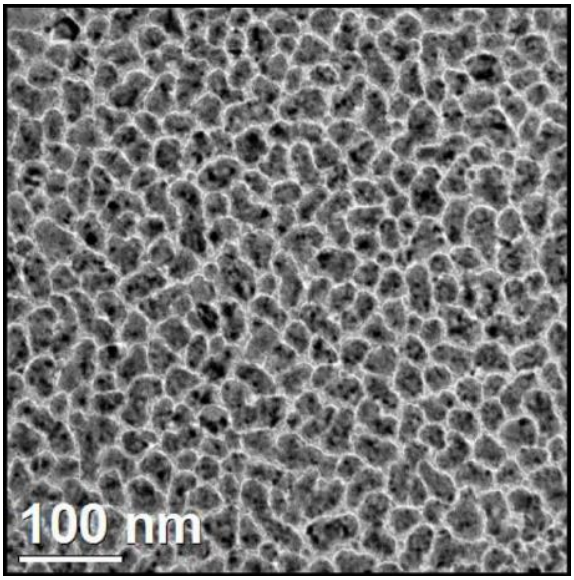

Figure 5. 5 TEM image of film grown on Cr/Ag seed layer.

To evaluate possible Cr diffusion into the Co_2FeSi layer the effect of the thickness of the Ag layer was also examined. As previously discussed, diffusion of Cr is reported to increase the coercivity of Co_2FeSi films [114]. This is due to the atomic mixing at the Cr/Co_2FeSi layer in the Heusler alloy structure [114]. However, in polycrystalline films studied in this work the coercivity is not expected to change since the coercivity of the sample is controlled by the pinning sites created from the rough surface.

Films were grown on Cr using Ag layers of thickness 6 nm, 15 nm and

30 nm to measure the range over which Cr diffusion may occur. The trend with annealing is more important as it would lead to interfacial diffusion [114]. After heating for 1 hour the coercivity of the film with a 6 nm Ag seed layer increased by 10 Oe, whilst the film with a 15 nm layer has a smaller increase of only 2.5 Oe. The film with 30 nm thick Ag seed layer shows a small decrease in H_c. This would suggest that annealing at 300°C encourages some Cr diffusion through the Ag layer but with a thicker layer the diffusion is probably stopped. The annealing was taken up to three hours and the coercivity was unchanged. All the measurements have an error of $\pm$ 2% based on the manufacturers specification.

It is clearly shown in Figure 5.6 that the coercivity of the sample with 30 nm Ag seed layer varies less than 3 Oe throughout the annealing process. This would suggest that with a 30 nm Ag layer, there is no Cr diffusion even after annealing at high temperature.

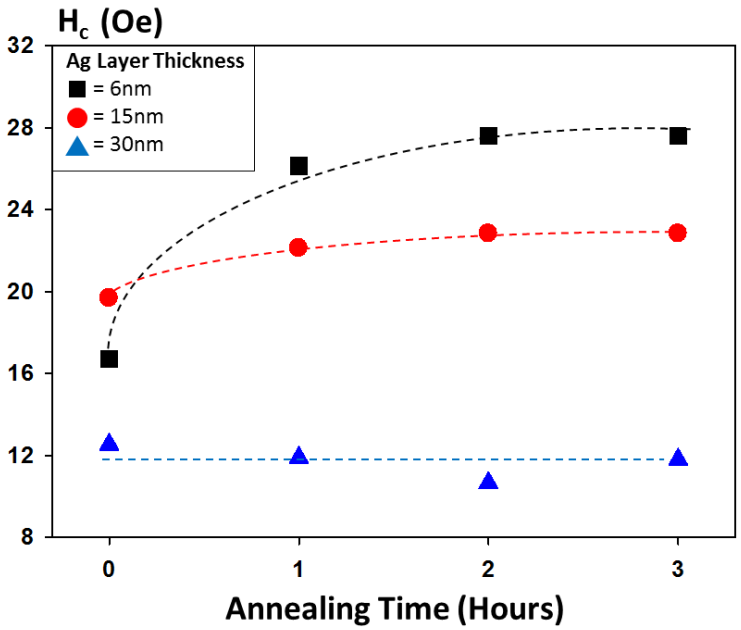

Figure 5.6 Variation of H_c with annealing time for polycrystalline Co_2FeSi films with 3 nm Cr buffer layer and different thicknesses of Ag seed layers.

In summary, the Cr layer reduces island growth of Ag and hence

limited columnar growth was observed. The magnetisation results Table 5.3 shows high value of squareness ratio of the sample with the seed layer(s) compared to the sample with no seed layer. Moreover a 30nm thick Ag seed layer gives a lower value of H_c. Therefore, the optimised structure is Cr (3nm)/Ag (30 nm)/Co_2FeSi (20 nm)/cap.

5.3 Quality of MBE Grown $Co_2FeAl_{0.5}Si_{0.5}$

Room temperature and low temperature VSM measurements have been performed to extract the temperature dependence of M_s. XRD was used to obtain the $Co_2FeAl_{0.5}Si_{0.5}$ structural information. Ferromagnetic resonance (FMR) measurements were carried out to determine the damping coefficient temperature dependence. There are some previous works on Co_2FeAl [133], Co_2FeSi [135] and $Co_2FeAl_{0.5}Si_{0.5}$ [134] but the temperature variation of their key parameters was not reported.

5.3.1 Sample Fabrication

UHV MBE was used to grow the sample. A 30nm thick $Co_2FeAl_{0.5}Si_{0.5}$ layer was grown on single crystal MgO (001) substrate and capped with 5 nm of Au. The growth procedures were discussed in section 4.3. Before deposition the substrate was annealed at 600 °C for 30 minutes in order to remove impurities. After the film growth, the sample was *in-situ* annealed at 350 °C for 1 hour. An annealing temperature of 350 °C is necessary for obtaining $L2_1$ crystal structure [136].

5.3.2 Magnetic and Structural Results

Magnetic measurements were made using a Lakeshore model 10 VSM. Hysteresis loops of the sample were taken in two different planes [100] and [110] and are shown in Figure 5.7. The data shows that [100] direction is the hard axis and [110] is the easy axis. The data shows that the coercivity is the same in both directions. This is because H_c is dominated by domain wall pinning which is independent of the direction of measurement and the form

of the curves and particularly the squareness, show that the [110] direction is the easy asix since M_r/M_s is almost unity in this direction. Reversal then proceeds by nucleation and rapid domain wall motion with domain rotation beyond about -0.7M_s.

In the [100] direction there is significant domain rotation in positive fields due to the higher anisotropy. Some domain wall motion occurs followed by rotation beyond ~ -0.5 M_s. The hard and easy axes of the sample are the only structural information which can be obtained from the magnetic measurements.

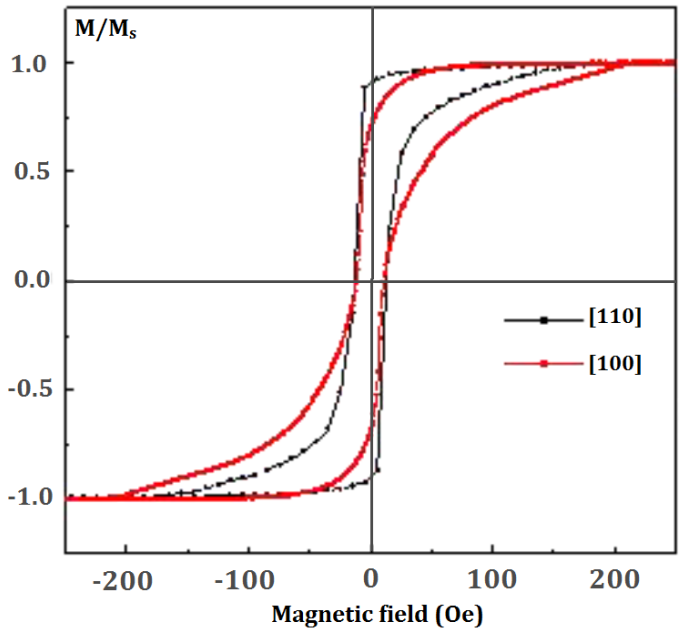

Figure 5.7 Hystersis loops of $Co_2FeAl_{0.5}Si_{0.5}$ film along [110] and [100] direction.

The major difference in the curves shown in Figure 5.7 is that in the easy axis [110] direction reversal proceeds by reverse domain nucleation at ~ 25 Oe followed by strong exchange coupling induced domain wall motion where the loop goes down abruptly. The slow approach to saturation is due to domain rotation over a hard axis and the increasing demagnetising field. The hard axis required >200 Oe to saturate the magnetisation.

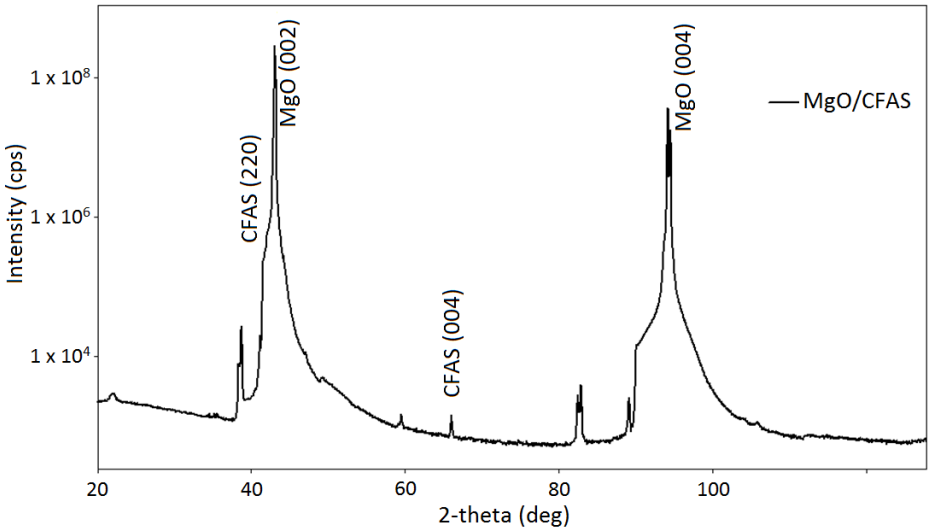

Figure 5.8 θ-2θ scan of the single $Co_2FeAl_{0.5}Si_{0.5}$ layer sample after 1 hour annealing.

In Figure 5.8, the XRD θ-2θ scan was set at the range of 20°-120° to show the $Co_2FeAl_{0.5}Si_{0.5}$ peaks. Two main peaks of MgO substrate at ~43° and ~94°are clearly observed. However, $Co_2FeAl_{0.5}Si_{0.5}$ shows only one peak at 66 ° which is one of the peaks that indicate a *B*2 structure for the $Co_2FeAl_{0.5}Si_{0.5}$ film [135]. The other peak is at ~ 42.8° which overlaps with the shoulder of the MgO ~43° main peak. A pole figure scan can be performed to confirm the presence of *B*2 or $L2_1$ structure of the film which is discussed in the next session.

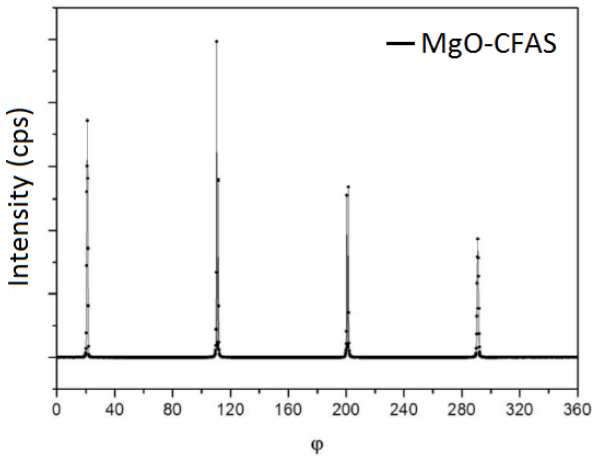

Figure 5.9 Phi scan of $Co_2FeAl_{0.5}Si_{0.5}$ (220).

In Figure 5.9, the Phi scan incident angle was scanned around

$Co_2FeAl_{0.5}Si_{0.5}$ (220) peak. This Phi scan shows the peaks separated 90° from each other. Confirming the four-fold symmetry of the film and the existence of (220) peak.

Ferromagnetic resonance (FMR) measurements were carried out to determine T_c and the damping parameter (α) of the sample. The damping parameter is considered phenomenological because its microscopic origin is not fully understood and is still the subject of research. Furthermore, both exchange coupling between spins and the lattice and spin scattering can contribute to the damping [138].

The following measurements were carried out by L. M. Loong et. *al.* of National University of Singapore. An Agilent N5245A vector network analyser (VNA) was connected to asymmetric coplanar wave guides (ACPWs), and reflection as well as transmission signals were measured to study the FMR. To enable low-temperature measurements, the setup was installed in a cryostat manufactured by Janis Research Company. Background subtraction was performed to obtain the resonance peaks.

In Figure 5.10, it shows that α decreases as temperature increases, in the temperature range of 13–300 K. The value of α was found to be 0.0025 at room temperature, which is approximately 6 times lower than the value of 0.014 at 13 K. This result is consistent with a previous report where the sample was capped with Ta instead of Au [138]. Therefore, it can be assumed that Au capping layer make little or no contribution to the damping in the film.

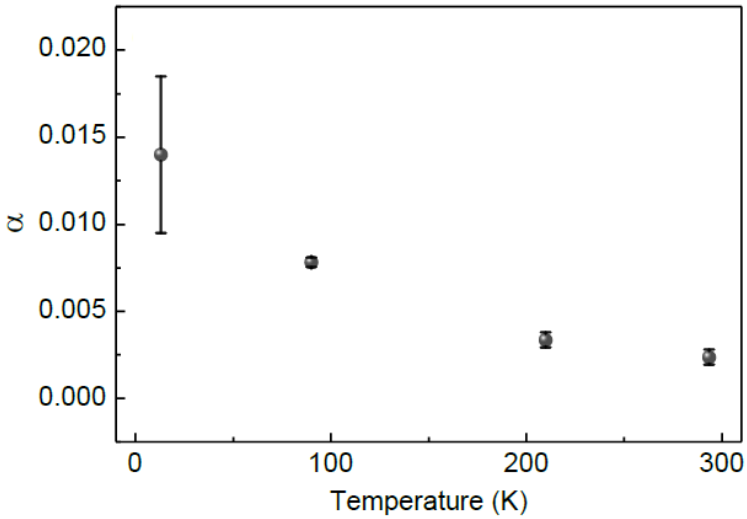

Figure 5.10 α values as a function of temperature.

The Singapore group also measured the Curie temperature (Tc) of the film using the ferromagnetic resonance and plotted the data with Bloch fitting. The value found was ~1000K [138]. The investigation of the magnetic, structural and damping properties of $Co_2FeAl_{0.5}Si_{0.5}$ provides insights for the design and engineering of spintronic devices. It is a promising ferromagnetic material for spintronics applications due to its high T_c, high M_s, low α and well-ordered crystalline structure.

5.4 Effect of Dual Seed Layers on $Co_2FeAl_{0.5}Si_{0.5}$ film

The optimised thicknesses of Cr and Ag for the dual seed layer system were developed for the Co_2FeSi sample. The optimised film thickness has also been used with $Co_2FeAl_{0.5}Si_{0.5}$ on the MgO substrate. Details of the substrate, preparation and in-situ annealing were provided in section 4.3.

Both structures of Cr (3 nm)/Ag (30 nm)/$Co_2FeAl_{0.5}Si_{0.5}$ (20 nm)/Ta (3 nm) and Ag (30 nm)/$Co_2FeAl_{0.5}Si_{0.5}$ (20 nm)/Ta (3 nm) were grown epitaxially on MgO substrates at room temperature under UHV. The film growth process was monitored using RHEED. Two hours annealing was used

for both samples. High quality epitaxial films were grown due to the good lattice match between each layer. The lattice matching between the layers was not taken into consideration in the previous section since the films were not epitaxially grown. The lattice constant of MgO, Cr and Ag are 4.21 Å, 2.88 Å and 4.09 Å respectively [73, 78]. It is well known that films tend to grow on MgO at a 45° in-plane rotation as shown Figure 5.11 which leads to the mismatch ratio of MgO/Cr is 3% and that of MgO/Ag is 31%. By considering the lattice matching, it is clear that Cr is a better candidate for the first under-layer.

Figure 5.11 Schematic representation of the epitaxial relationship of Cr under-layer on MgO substrate.

5.4.1 Structural Characterisation result for $Co_2FeAl_{0.5}Si_{0.5}$ film

In-situ RHEED images were obtained in the UHV MBE system during growth. Structural properties was studied using a 9kW Rigaku XRD system and TEM images were obtained using a JEOL JEM-2011 TEM.

The $L2_1$ or $B2$ ordering of $Co_2FeAl_{0.5}Si_{0.5}$ is important for continued development of this system. A conventional θ-2θ scan was performed as shown in Figure 5.12. The main (002) peaks of MgO at ~43°, (002) peak of Ag at ~44° and (004) peak of $Co_2FeAl_{0.5}Si_{0.5}$ at ~66° which is different from the

angle found in section 5.2.2. The (004) reflection of $Co_2FeAl_{0.5}Si_{0.5}$ is at 65.7° (Figure 5.8) and that obtained from Figure 5.12 is 66.2° which could be due to lattice stretching. The predicted (220) peak of $Co_2FeAl_{0.5}Si_{0.5}$ is not observed in this scan as it is obscured by the (002) peak of MgO. To investigate the ordering of these films a pole figure scan was performed and is shown in Figure 5.13.

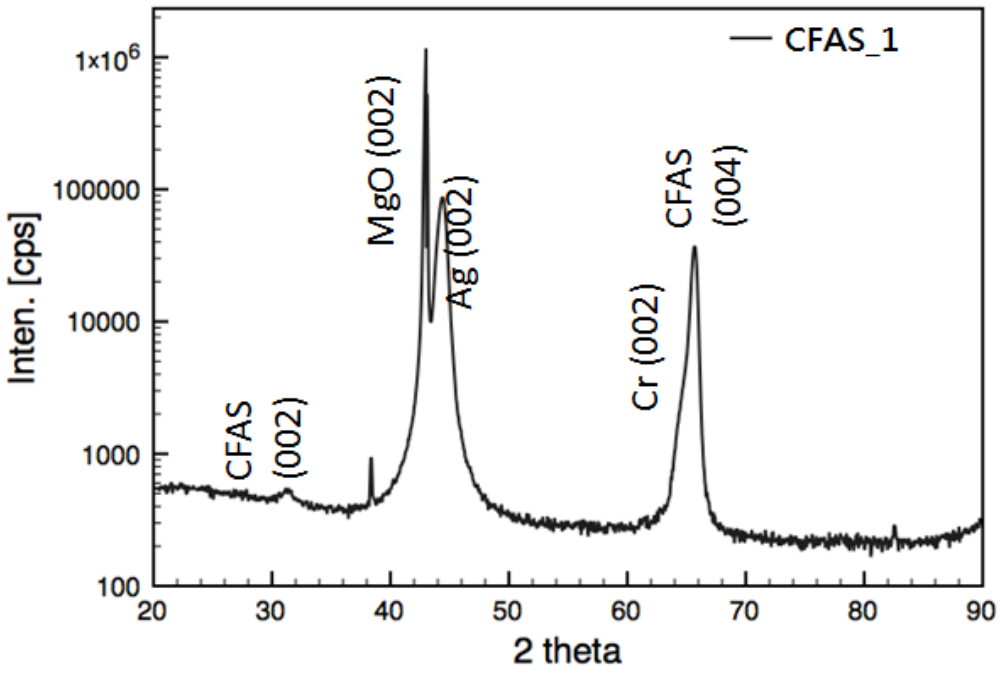

Figure 5.12 θ -2θ scan on $Co_2FeAl_{0.5}Si_{0.5}$ with Cr/Ag dual seed layer sample.

In the previous study on an epitaxial $Co_2FeAl_{0.5}Si_{0.5}$ film, it was found that the presence of (111) reflection $Co_2FeAl_{0.5}Si_{0.5}$ is essential to identify $L2_1$ ordering [132]. Figure 5.13 shows the pole figure scans around the $Co_2FeAl_{0.5}Si_{0.5}$ (111) and (400) peaks. In Figure 5.13 (a), there is a clear inner ring which corresponds to $Co_2FeAl_{0.5}Si_{0.5}$ (111). Figure 5.13 (b) shows a stronger intensity of the inner ring than that in Figure 5.13 (a) which suggests that *B*2 ordering is still the main ordering of the film. However the presence of $L2_1$ ordering is confirmed. A strong set of four-fold symmetry indicates a high

crystalline uniformity as shown in Figure 5.13 (b).

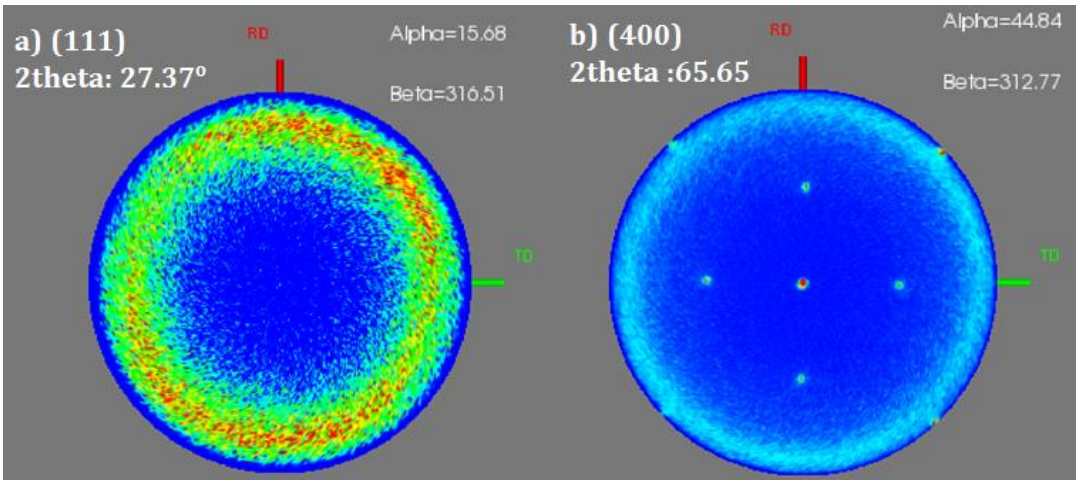

Figure 5.13 Pole figure measurements of the sample at (a) (111) and (b) (400) plane of the $Co_2FeAl_{0.5}Si_{0.5}$ film.

In order to confirm the crystalline quality, RHEED images were obtained. These images were taken in the MBE system as the film was deposited. The technique of obtaining these images was discussed in section 4.6.

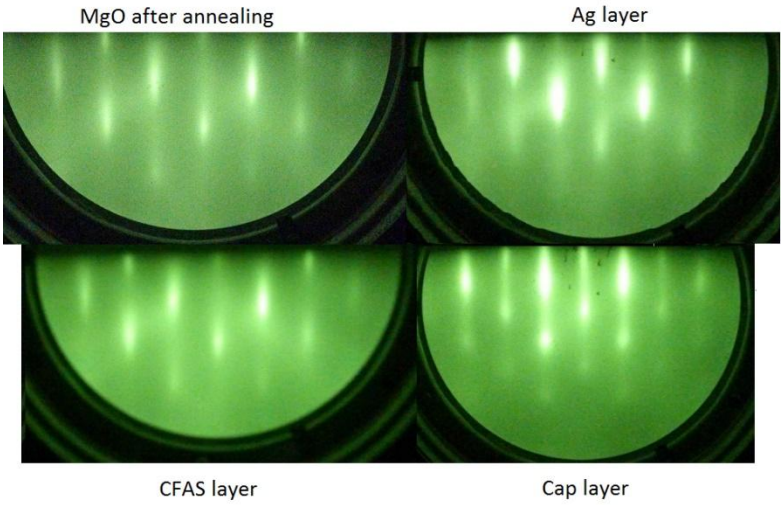

Figure 5.14 RHEED images of sample without Cr under layer.

Figure 5.14 shows RHEED images of sample without a Cr under-layer. After substrate annealing the RHEED image shows a partially streaky and spotty image. After the deposition of the Ag layer, the spotty pattern becomes

more obvious and the streaky pattern fades. After the deposition of the $Co_2FeAl_{0.5}Si_{0.5}$ layer the streaky pattern becomes slightly solid. Finally when the cap layer was deposited, the streaky pattern with strong spots is very clear. The spotty pattern indicates a rough surface or islands formed on the surface whereas the streaky pattern indicates a flat surface.

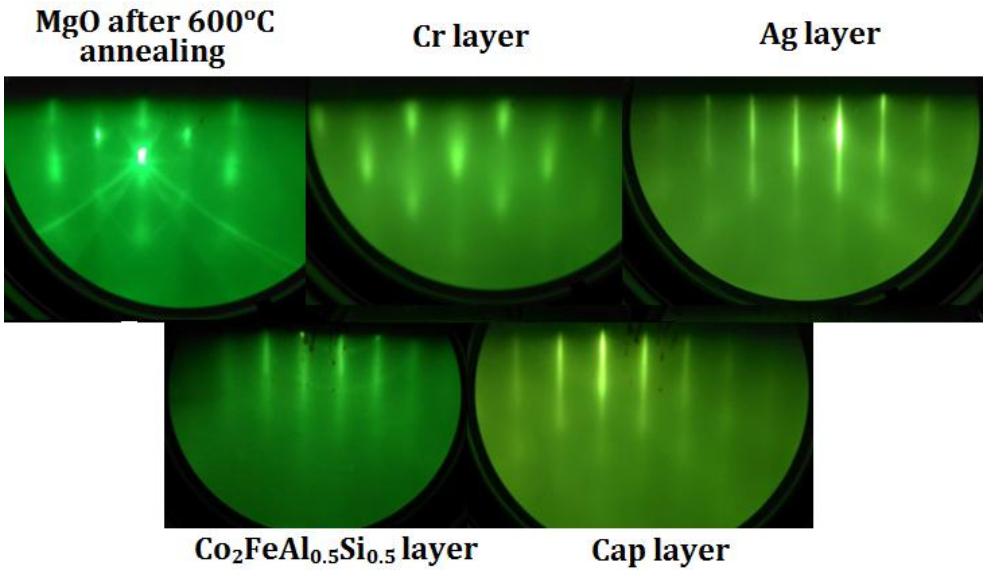

Figure 5.15 RHEED images of sample with Cr under-layer

Figure 5.15 shows RHEED images of a sample with a Cr under-layer. The spotty pattern almost disappears after the deposition of the Ag layer. After the deposition of the $Co_2FeAl_{0.5}Si_{0.5}$ layer only a streaky pattern was found. These RHEED images show that the sample has good ordering and a smooth surface compared to the data in Figure 5.14. This is confirmed by the cross sectional TEM image shown in Figure 5.16.

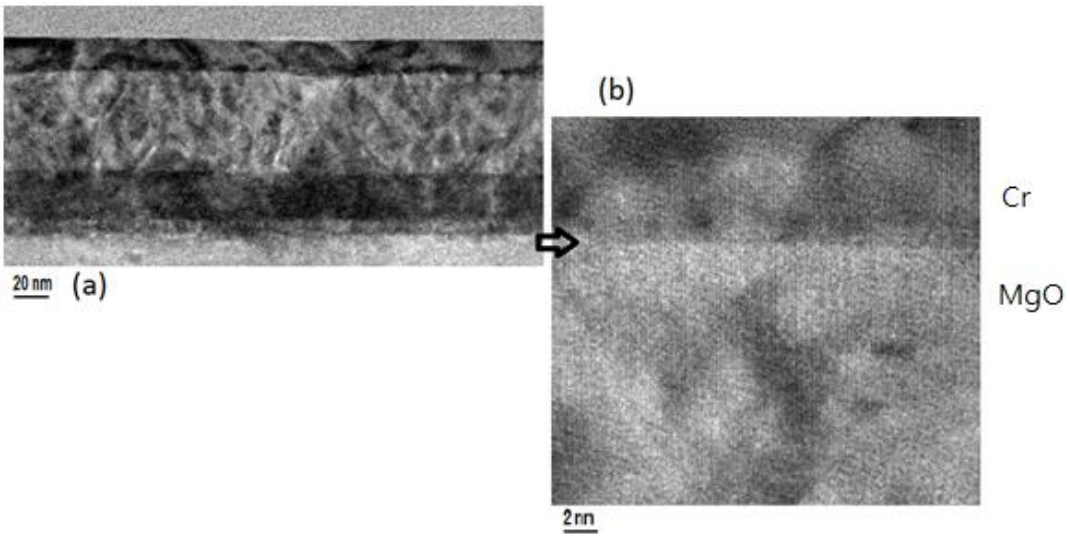

Figure 5.16(a) Cross-sectional TEM image of epitaxially grown samples of $Co_2FeAl_{0.5}Si_{0.5}$ with Cr under-layer; (b) interface of Cr and the MgO substrate

The epitaxial growth of the $Co_2FeAl_{0.5}Si_{0.5}$ films is further confirmed by TEM analysis. Figure 5.16 (a) shows a cross-sectional TEM image of the sample with Cr under-layer and Figure 5.16 (b) shows the interface of the Cr layer and the MgO substrate. It is clear that there is no columnar growth in this sample and Figure 5.16 (b) shows a well textured image reflects the small lattice mismatch between the layers.

From both XRD and TEM observations, $B2$ structure is strongly confirmed to exist. The $L2_1$ structure was only confirmed by the pole figure scan and Phi scan for $Co_2FeAl_{0.5}Si_{0.5}$ (004) as $Co_2FeAl_{0.5}Si_{0.5}$ (004) only occurs when there is $L2_1$ structure. These results all indicate that the films are highly textured with a high degree of ordering with a mixture of $B2$ and $L2_1$ structures.

5.4.2 Magnetic Measurements for $Co_2FeAl_{0.5}Si_{0.5}$

Magnetic measurements on epitaxial $Co_2FeAl_{0.5}Si_{0.5}$ films were made using a VSM at room temperature. It can be seen from the normalised

hysteresis loops in Figure 5.17 that the samples exhibit similar magnetic parameters to the polycrystalline samples described in section 5.2.3, having low coercivity and domain wall pinning. However the seed layers give different values of M_s, M_r/M_s and H_c. The data for both sets samples is gathered in Table 5.4.

	M_s (emu/cm^3)	M_r/M_s	H_c (Oe)
Ag seed layer (HiTUS)	950±19	0.66	33.2±0.7
Cr/Ag seed layers (HiTUS)	1010±20	0.86	29.4±0.6
Ag seed layer (MBE)	934±19	0.53	28.0±0.6
Cr/Ag seed layers (MBE)	1020±20	0.78	29.5±0.6

Table 5. 4 Summary of magnetic data for $Co_2FeAlSi$ polycrystalline and epitaxial thin films.

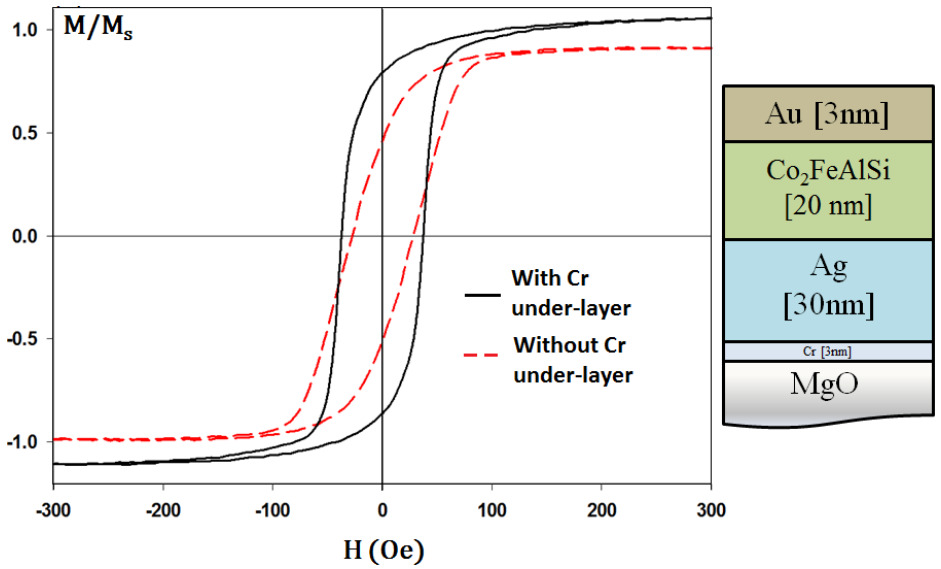

Figure 5.17 Hysteresis loops of MBE epitaxially grown samples with Cr/Ag and without Cr under-layer.

In summary, these results show that the crystal ordering of the films is

a mixture of *B*2 and $L2_1$ ordering. It is also found that the effect of the Ag island growth can be mitigated by a 3 nm Cr underlayer and at the same time gives a reduced roughness of the seed layer. The magnetic properties of the films for both polycrystalline and epitaxial films are also improved using the dual seed layer.

Chapter 6

Exchange Bias in $Co_2FeAl_{0.5}Si_{0.5}$

6.1 Effect of Exchange Coupling in $Co_2FeAl_{0.5}Si_{0.5}$/Cr Films

There have been few reports on exchange bias behaviour of Co-based Heusler alloys, which are half-metallic ferromagnets. Exchange bias is the coupling between F and AF spins at an interface. While the sample is cooled between the Néel temperature and Curie temperature with a presence of an applied magnetic field, the interfacial AF spins are coupled to the F spins. During the magnetisation reversal, the AF layer spins do not follow the applied magnetic field, resulting in a horizontal loop shift [139]. To increase the interfacial exchange bias, thin F/AF layers with their crystalline matching are favourable. The reason is that it is difficult to control several critical parameters such as lattice mismatch, diffusion across the interface and impurities. The largest value of exchange bias at room temperature reported for Heusler alloys were 2520 Oe with a superparamagnetic $Ni_2Mn(Al,Si)$ polycrystalline bulk sample [140] and 250 Oe with a $Co_2FeAl_{0.5}Si_{0.5}$/IrMn polycrystalline film [141]. These works are all based on the conventional exchange coupling induced at the F/AF interfaces.

According to Culbert *et al.* [142], a weak AF Cr ultrathin layer inserted to a $L2_1$ Heusler alloy layer is predicted not to affect its half-metallicity. It was found that a small strain applied to a Heusler alloy can induce a large change, e.g. caused a 30 ^{o} tilt in magnetic anisotropy which is observed and discussed in this chapter.

Antiferromagnetic Cr was selected because it has a relatively good

epitaxial relationship with $Co_2FeAl_{0.5}Si_{0.5}$ which was discussed in the previous section. Trilayers of epitaxially grown $Co_2FeAl_{0.5}Si_{0.5}$/Cr/ $Co_2FeAl_{0.5}Si_{0.5}$ structure was presented by Furubayashi et *al.* [143], however they only show a 90^o exchange coupling. This discrepancy between the theory and experiment may be caused because defects can be induced during the growth due to the lattice mismatch between the $Co_2FeAl_{0.5}Si_{0.5}$ and Cr layers (1.4%) [144, 145].

6.2 Sample Fabrication

In this study exchange anisotropy was intentionally introduced in a $Co_2FeAl_{0.5}Si_{0.5}$/Cr interface to induce exchange bias. The effect of crystalline strain on the exchange bias at the $Co_2FeAl_{0.5}Si_{0.5}$/Cr interface is investigated using a repeated stack of $Co_2FeAl_{0.5}Si_{0.5}$/Cr. Epitaxial growth and precise magnetic measurements with accurate in-plane magnetic field control has allowed a systematic study of the interfacial exchange bias and the induced lattice strain.

Samples with a stack structure of Cr (3)/Ag (30)/[$Co_2FeAl_{0.5}Si_{0.5}$ (t_{CFAS})/Cr (t_{Cr})]$_3$/Au (3) (nm) as shown in Figure 6.1, where $Co_2FeAl_{0.5}Si_{0.5}$ is the F layer and Cr is the AF layer, were grown on a single crystal MgO (001) substrate by UHV MBE at room temperature. The specification of the growth process is given in section 4.3. A series of samples were produced by varying the $Co_2FeAl_{0.5}Si_{0.5}$ thickness in the range 1 nm$\leq$ t_{CFAS} $\leq$ 4 nm and the Cr thickness was 0.3 nm$\leq$ t_{Cr} $\leq$ 1.2 nm. These thicknesses were much smaller than those used in the previous study on a similar system reported in reference [143] and with more $Co_2FeAl_{0.5}Si_{0.5}$/Cr interfaces by repeating the layers. No annealing was performed during and after the deposition to avoid

inter-layer-diffusion of the Cr layer.

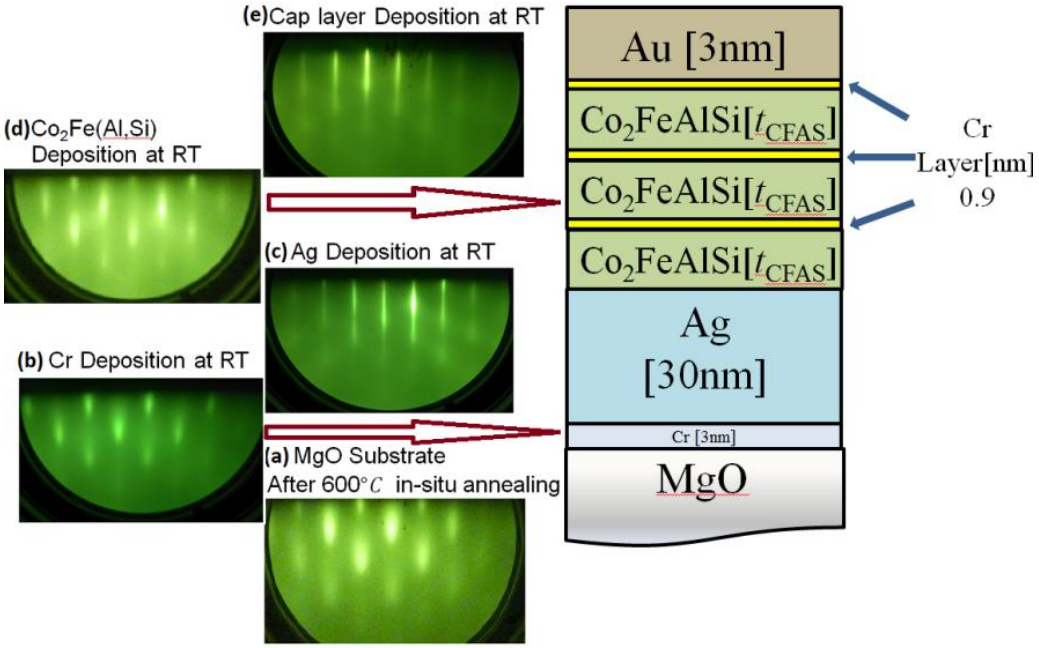

Figure 6.1 Schematic multilayered structure and the associated RHEED patterns taken (a) after annealing the MgO(001) substrate at 600°C for 1 h and after the deposition of (b) Cr, (c) Ag, (d) $Co_2FeAl_{0.5}Si_{0.5}$ and (e) Au layers at RT.

6.3 Structural Data

RHEED images for analysing surface structures were obtained during the MBE growth. Images were taken before and after the growth of each layer as shown in Figure 6.1. The RHEED pattern from the MgO substrate has relatively large spots, indicating that the surface of the substrate exhibited long-range roughness after annealing. Such roughness can be removed by depositing the Cr and Ag buffer layers as confirmed by the streak RHEED patterns. The pattern after the Ag deposition at room temperature clearly shows the formation of the face-centred cubic (FCC) (001) surface, confirming the epitaxial relationship of MgO (001) [110]//Ag (001) [110] with 3.1% lattice mismatch as reported previously [146]. The $Co_2FeAl_{0.5}Si_{0.5}$ deposition is found to make the surface slightly rough as shown by the increase in the

width of the streaks. This is due to initial island-like growth of the $Co_2FeAl_{0.5}Si_{0.5}$ layer. However, the epitaxial growth with the above crystalline orientation is maintained throughout the layer stack up to the Au capping layer.

The crystalline structure of the sample was analysed by XRD at the Photon Factory (PF) in the High Energy Acceleration Organization (KEK) in Japan and JEOL TEM-2011 at York.

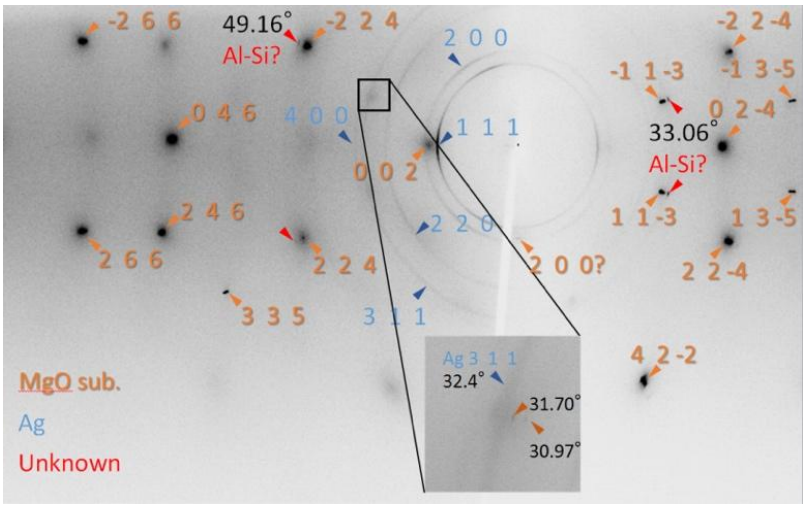

Figure 6. 2 XRD pattern of the [t_{CFAS} = 3 nm/ t_{Cr} = 0.9 nm] sample. The magnified image in the vicinity of 30 ~ 33° is also shown.

XRD patterns were taken for one of the samples with t_{CFAS} = 3 nm and t_{Cr} = 0.9 nm as shown in Figure 6.2. The pattern clearly shows strong spots from the MgO substrate, proving the single-crystalline nature of the substrate. However, the Ag (111), (220) and (200) patterns form a weak ring, indicating that the Ag seed layer has some texture with minor crystalline misalignments in the plane. This may be induced by the long range roughness of the MgO substrate initially observed in Figure 6.1. Additionally rings are seen just outside of the Ag (220) ring in Figure 6. 2, which may represent Au (220) and $Co_2FeAl_{0.5}Si_{0.5}$ (400). Here, Cr (200) may be overlapped with the Au peak, which suggests the lattice contraction of the Cr layer due to the presence of

the $Co_2FeAl_{0.5}Si_{0.5}$ neighbouring layer.

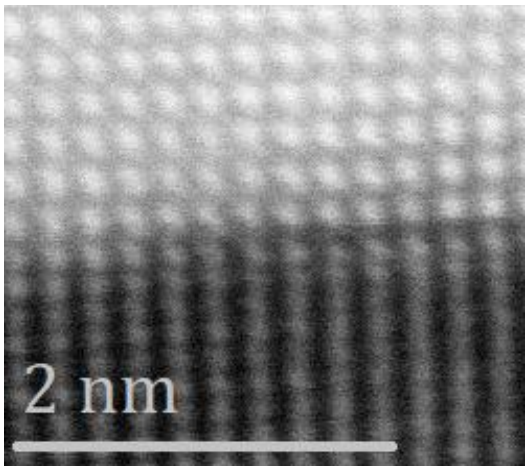

Figure 6. 3 High resolution TEM image of $Co_2FeAl_{0.5}Si_{0.5}$/Cr interface showing the existence of mixing.

Figure 6. 3 shows TEM image for the [t_{CFAS} = 3 nm/t_{Cr} = 0.9 nm] sample, with the sample prepared using the techniques described in section 4.8.3. It can be seen that there is mixing at the interface to approximately 4 atomic layers and some misalignment between the $Co_2FeAl_{0.5}Si_{0.5}$ and Cr films.

In order to confirm this lattice contraction, further experimental work is suggested in the last section. The epitaxial growth of the [$Co_2FeAl_{0.5}Si_{0.5}$/Cr] samples with some in-plane misaligned texture is confirmed by these rings and the high resolution TEM image.

6.4 Magnetic Measurements

The following measurements were all taken by Microsense Model 10 VSM as described in section 4.11. To engineer the exchange bias, the thickness of the Cr layer was first optimised to induce the maximum change on the magnetisation curves of the [$Co_2FeAl_{0.5}Si_{0.5}$/Cr] samples. Figure 6.4 (a) shows the magnetisation curves with t_{CFAS} = 2 nm and 0.3 nm ≤ t_{Cr} ≤ 1.2 nm. The sample with t_{Cr} = 0.9 shows a largest H_c and squareness (0.98) as shown in

Figure 6.5, therefore, $t_{Cr} = 0.9$ nm was selected for further investigation.

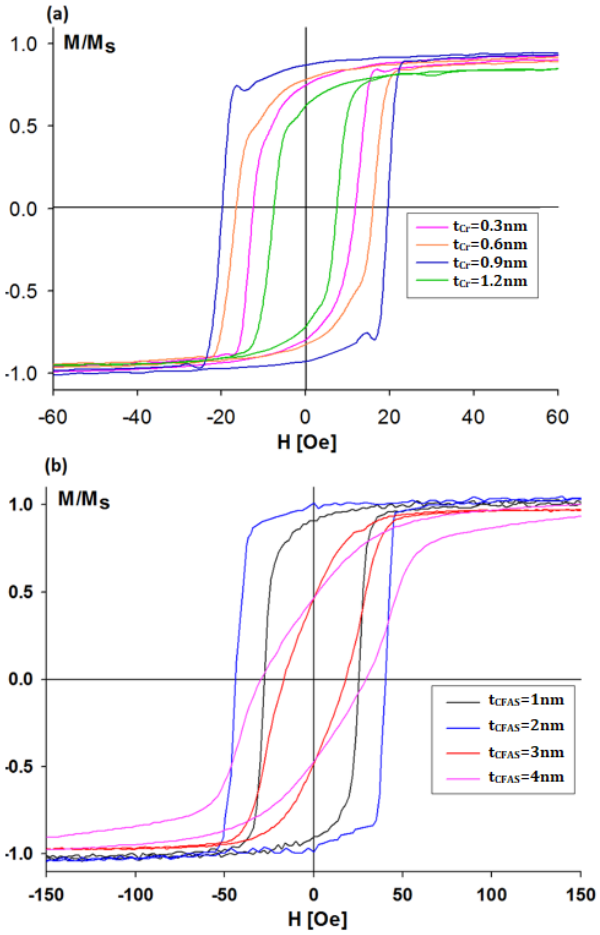

Figure 6.4 Magnetisation curves of the (a) [$t_{CFAS} = 2$ nm/t_{Cr}] with 0.3 nm≤ $t_{Cr} \leq 1.2$ nm measured at RT and (b) [$t_{CFAS}/t_{Cr} = 0.9$] with 1 nm ≤ $t_{CFAS} \leq 4$ nm.

The thickness of the $Co_2FeAl_{0.5}Si_{0.5}$ layer was then optimised by maintaining t_{Cr} of 0.9 nm, as shown in Figure 6.4 (b). By varying the thickness of both Cr and $Co_2FeAl_{0.5}Si_{0.5}$, M_s and H_c vary from 619 emu/cm^3 ($t_{CFAS} = 1$ nm and $t_{Cr} = 0.3$ nm) to 1180 emu/cm^3 ($t_{CFAS} = 2$ nm and $t_{Cr} = 0.9$ nm) and 10 Oe ($t_{CFAS} = 1$ nm and $t_{Cr} = 0.3$ nm) to 80 Oe ($t_{CFAS} = 2$ nm and $t_{Cr} = 0.9$ nm), respectively. Note that there is no loop shift as the samples were not field annealed.

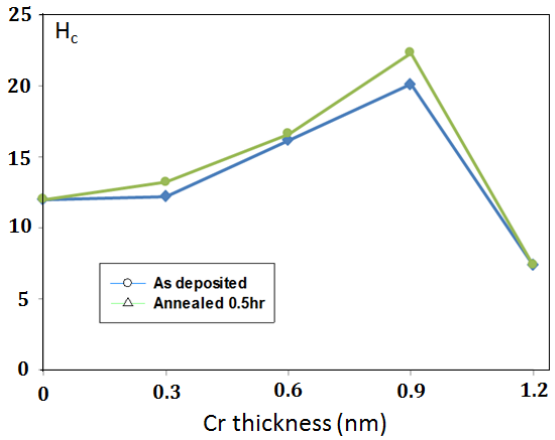

Figure 6.5 H_c as a function of Cr thickness.

The highest coercivity, squareness and saturation magnetisation of (80±2) Oe, (0.89±0.02) and (1180±20) emu/cm^3 were obtained using t_{CFAS} = 2 nm and t_{Cr} = 0.9 nm. Although the sample with 0.9nm Cr and 2nm $Co_2FeAl_{0.5}Si_{0.5}$ has the highest coercivity, but yet is still <100Oe. The objective of this optimisation was to control the coercivity to be less than 100 Oe and maximise the squareness of the thin film sample. Therefore the thickness of 2nm of $Co_2FeAl_{0.5}Si_{0.5}$ and 0.9nm of Cr were used for the rest of the experiment.

The reversal mechanism in the sample with t_{CFAS} = 2 nm and t_{Cr} = 0.9 nm is domain wall pinning with a high value of M_r/M_s due to the exchange coupling. The high squareness of the loop also indicates the exchange coupling between the layers of $Co_2FeAl_{0.5}Si_{0.5}$ across the Cr layer. Hence reversal proceeds via the initial nucleation of one or more domains followed by fairly rapid domain wall motion throughout the sample impeded by weak domain wall pinning.

These samples with t_{Cr} = 0.9 nm were also evaluated by rotating the in-plane fields at 193K. The largest value of squareness (M_r/M_s =0.98) is found to lie at 140° from the MgO [110] axis and the smallest M_r/M_s is 0.34 at

40° in the sample with t_{CFAS} = 2 nm. $Co_2FeAl_{0.5}Si_{0.5}$ has been reported to be cubic and to exhibit fourfold magnetic anisotropy in bulk [69] but the Co-based Heusler alloys are known to show uniaxial anisotropy in thin film form typically <80nm [147].

The magnetic anisotropy is a critically important property of a ferromagnetic film since it determines the easy magnetization directions of the film at low magnetic field. Figure 6.6 shows uniaxial anisotropy in the thinner region ($t_{CFAS} \leq 4$ nm) which is not consistent with the previous report but is similar to an ultrathin Fe film strained by lattice mismatch [148]. In [148], it was shown that the uniaxial anisotropy originated from the Fe/GaAs interface and the effect is inversely proportional to the Fe thickness. It is interesting to note that the maximum uniaxial anisotropy is from the sample with t_{CFAS} = 2 nm. The uniaxial anisotropy is found to be a maximum at ~ 30° from the MgO [110] axis.

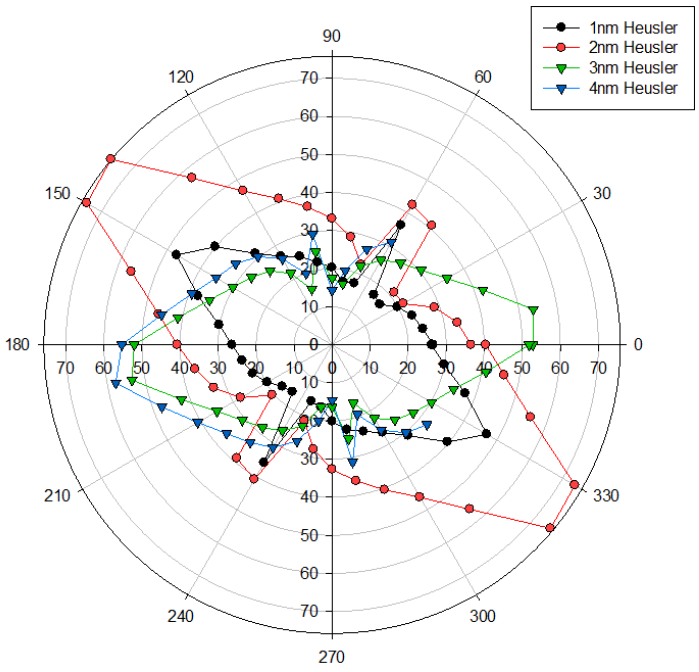

Figure 6.6 H_c polar plot for the 4 samples with 1 nm ≤ t_{CFAS} ≤ 4 nm with t_{Cr} = 0.9 nm.

The origin of the 30° tilt for the samples with 1 and 2 nm of

$Co_2FeAl_{0.5}Si_{0.5}$ is not clear at this stage but it may be induced by interfacial coupling which may also be the origin of the uniaxial anisotropy. Any lattice mismatch may also lead to a strain anisotropy [148]. The direction of this strain has not been investigated.

As the thickness of the Heusler alloy layer increases above 3 nm, H_c is found to decrease, which is the result of emerging bulk like properties of the Heusler alloy layers. It should also be noted that the uniaxial anisotropy changes its orientation along the MgO [110] axis above $t_{CFAS} = 3$ nm. This may indicate that the strong uniaxial anisotropy at ~ 30° induced by the Cr layer is interfacially sensitive and can be relaxed along the MgO [110] axis above five monolayers (~ 3 nm) of the $Co_2FeAl_{0.5}Si_{0.5}$ deposition as previously reported [136].

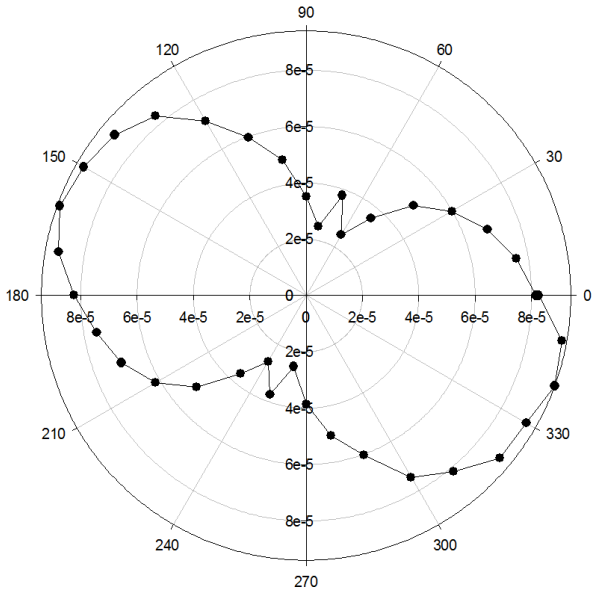

Figure 6.7 A corresponding M_r polar plot of the sample with $t_{CFAS} = 2$ nm.

Figure 6.7 shows the corresponding remanence of the sample with $t_{CFAS} = 2$ nm. This graph also shows the 30° offset from the MgO [110] axis which confirms the existence of the tilt. This offset vanishes by removing the Cr neighbouring layer, *i.e.*, single $Co_2FeAl_{0.5}Si_{0.5}$ layer on MgO (001), as shown

in Figure 6.8 which confirms the 30 offset from the MgO [110] is induced by the Cr layer.

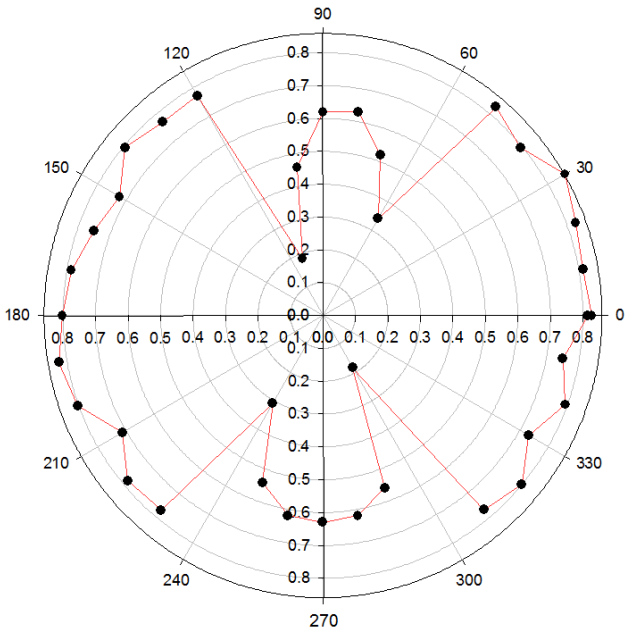

Figure 6.8 Polar plot of the sample with 2 nm thick single $Co_2FeAl_{0.5}Si_{0.5}$ film grown on the MgO substrate.

In the samples with $t_{CFAS} = 2$ nm following field cooling from 303K to 193K in H=1kOe, there is a loop shift of 18 Oe as shown in Figure 6.9. An expanded view is shown in Figure 6.10. This is five times larger than the previously reported value [137]. This proves that exchange bias can be induced even by a weak AF layer by introducing additional interfacial strain in an epitaxial F/AF structure. The loop shift of the 45° curve is asymmetric. This may due to the coupling of the spins at the interface.

Furthermore, the M_s is found to be (1180±23) emu/cm^3 corresponds to 128% of the theoretical value predicted by the generalised Slater-Pauling curve [22]. This may indicate that the magnetic dead layer can be 0.25nm thick at the $Co_2FeAl_{0.5}Si_{0.5}$/Cr interfaces, which is similar to the epitaxial Co_2 Al/GaAs system previously reported [142]. However, the bulk regions of the $Co_2FeAl_{0.5}Si_{0.5}$ layers maintain their magnetic moments as predicted [137].

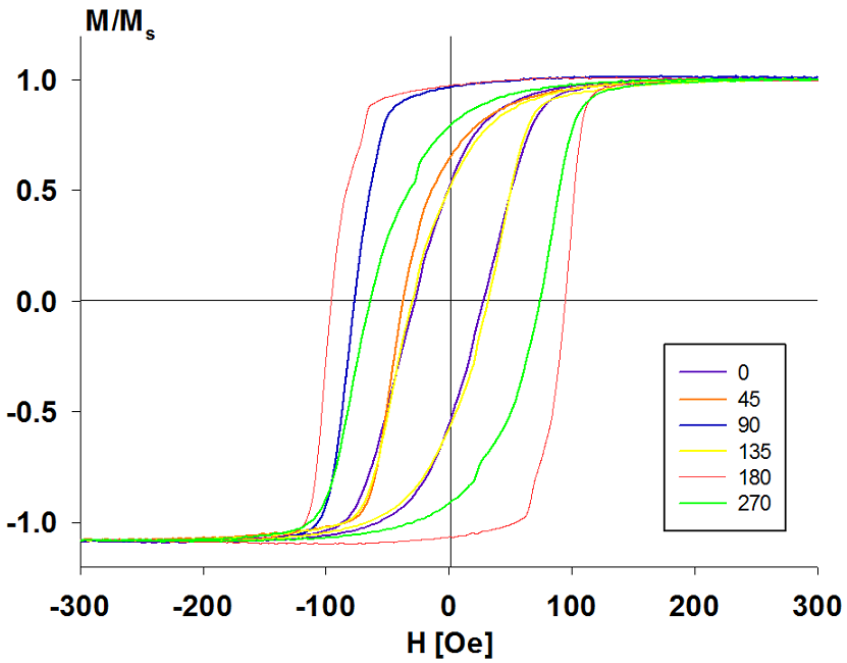

Figure 6.9 Hysteresis loops for the sample with $t_{\mathrm{CFAS}} = 2$ nm.

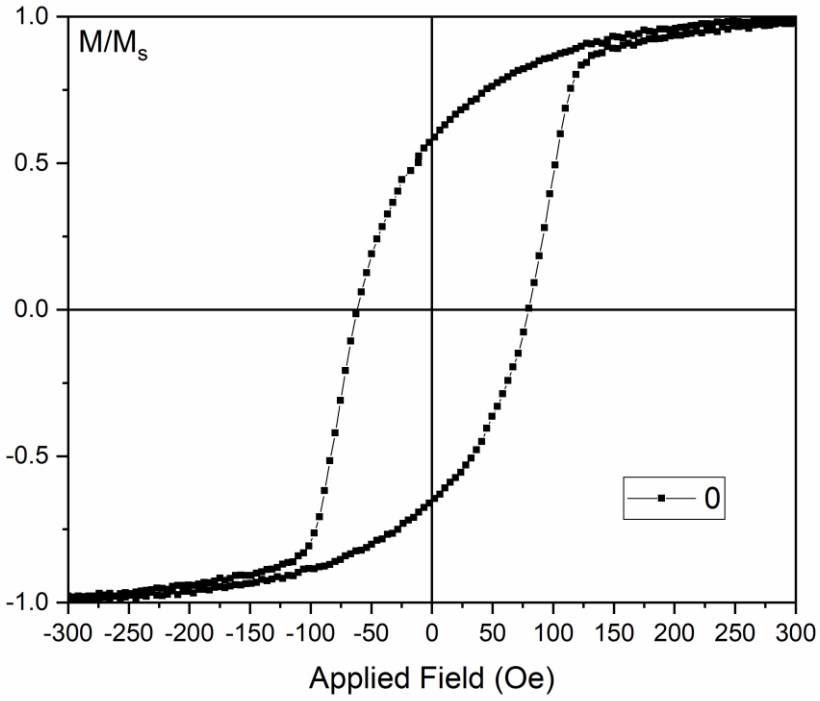

Figure 6.10 An expanded view of Figure 6.9 showing the loop shift.

Chapter 7

Conclusion and Future Work

7.1 Conclusion

In conclusion, the possibility of using CoFeSi and $Co_2FeAl_{0.5}Si_{0.5}$ for spintronic devices are investigated. And the use of seed layers under CoFeSi and $Co_2FeAl_{0.5}Si_{0.5}$ to improve the desired property for spintronic devices are also investigated. The main outcomes and conclusions are reiterated.

There are three main objectives in this work. The first was to investigate the effect of dual seed layer Cr/Ag on $Co_2FeAl_{0.5}Si_{0.5}$ and confirm the possibility of applying this structure as a basis in continued study. The other two were to examine the $Co_2FeAl_{0.5}Si_{0.5}$ film quality and to investigate exchange bias at the interface between $Co_2FeAl_{0.5}Si_{0.5}$ and a Cr layer.

For a low power consumption read/write head, high M_r/M_S and low coercivity are essential. In contrast for low power consumption in high density magnetic recording, low squareness and high coercivity are the key. In this study the elementary properties of both CoFeSi and $Co_2FeAl_{0.5}Si_{0.5}$ on MgO were first investigated.

HiTUS grown Co_2FeSi samples grown with bias voltage 850V was found to have a coercivity of (18 ± 0.9) Oe which is the lowest among all HiTUS grown samples however the squareness of that sample is also the lowest. Therefore MBE growth and the use of a seed layer are introduced to improve these magnetic properties. The MBE grown Co_2FeSi samples with Ag/Cr seed layers was found to have coercivity of 29.4 Oe and squareness of 0.86 which are desired for a low power consumption read/write head.

It was found that both polycrystalline and epitaxial films are improved using the dual seed layer. The $Co_2FeAl_{0.5}Si_{0.5}$ with Ag/Cr seed layer sample has a squareness of 0.78, coercivity of (29.5±0.6) Oe and highest saturation magnetization of (1020±20) emu/cm^3. The crystallinity of these films are studied using XRD, RHEED and TEM. The XRD scans show that there is a strong $B2$ ordering and a weak $L2_1$ ordering in the sample. The RHEED images confirm that the Cr layer provides a flat surface for following layers to grow on, thus streaky RHEED images were obtained. A cross sectional TEM image shows the films are well textured due to the small lattice mismatch between the Cr layer and the MgO substrate.

The investigation of applying this structure into spintronic devices examined using a multilayer exchange bias structure consisting of the $Co_2FeAl_{0.5}Si_{0.5}$. $Co_2FeAl_{0.5}Si_{0.5}$/Cr multilayer stack were studied and a sample ($t_{CFAS} = 2$ and $t_{Cr} = 0.9$) was measured in VSM at 193K showed a loop shift of (18±0.4) Oe, with a high M_s=(1180±23) emu/cm^3 and squareness=(0.89±0.02). A 30° offset from the MgO [110] axis was shown in all H_c and M_r polar plots. The reason of this tilt is not clear. The origin of the minor tilt is not clear at this stage but it may be induced by interfacial coupling. The tilt vanishes when the seed layers are removed as shown in Figure 7. 1.

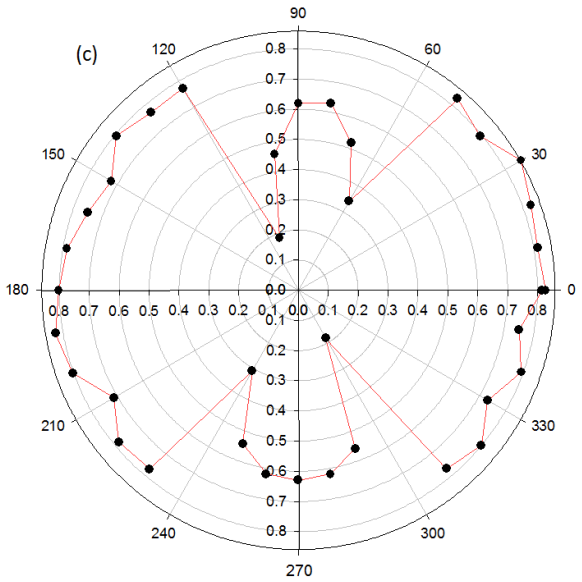

Figure 7. 1 Polar plot of coercive field as a function of the in-plane direction for Co2FeAl0.5Si0.5 (001) thin film.

7.2 Future Work

It is interesting to observe that the easy axis of the uniaxial anisotropy [110] starts to change above a 3nm thickness of the $Co_2FeAl_{0.5}Si_{0.5}$ layer. Moreover, the hysteresis loop shown in Figure 6.9 does not agree with previous findings from Hirohata et *al.* It was shown in the study of Hirohata et *al.* that the ferromagnetic Heusler alloys have uniaxial anisotropy superimposed on the fourfold cubic anisotropy [147]. Both the tilt of the easy axis and the inconsistency of the hysteresis loop findings may be caused by the effect of uniaxial anisotropy induced by the lattice mismatch inducing anisotropic strain.

In order to study this strain, high-angle annular dark-field (HAADF) scanning TEM is needed. TEM is useful for analysing larger areas of a sample, but HAADF-STEM is accessible for analysing the atomic interface structure of a small area of the sample which is the interfacial area between $Co_2FeAl_{0.5}Si_{0.5}$ and Cr layers.

References

1. G. Moore, Proceedings of the IEEE. 86, 82-85, 1998.
2. M. Baibich, J. Broto, A. Fert, F. Van Dau, F. Petroff, P. Etienne, G. Creuzet, A. Friederich and J. Chazelas, Phys. Rev. Lett. 61, 2472-2475, 1988.
3. G. Prinz, Science. 282, 1660-1663, 1998.
4. J. W. Jung, Y. Sakuraba, T. T. Sasaki, Y. Miura, and K. Hono, Appl. Phys. Lett. 108, 102408, 2016.
5. M. Julliere, Phys. Lett. A 54, 225-226, 1975.
6. T. Miyazaki, and N. Tezuka, J. Magn. Magn. Mater. 139, L231-L234, 1995.
7. I. Galanakis, P. H. Dederichs and N. Papanikolaou, Phys. Rev. B 66, 174429 2002.
8. T. Block, C. Felser and J. Windeln, Dig. EE01, Intermag, 2002.
9. G. H. Fecher, and C. Felser, J. Phys. D: Appl. Phys. 40 1582, 2007.
10. T. Furubayashi, K. Kodama, H. Sukegawa, Y. K. Takahashi, K. Inomata, and K. Hono, Appl. Phys. Lett. 93, 122507, 2008.
11. W. Thomson, Proc. Roy. Soc. 8, 546, 1857.
12. S. S. P. Parkin, Phys. Rev. Lett. 71, 1641, 1993.
13. G. Binasch, P. Grünberg, F. Saurenbach and W. Zinn, Phys. Rev. B 39, 4828-4830, 1989.
14. S. Ikeda, J. Hayakawa, Y. Ashizawa, Y. M. Lee, K. Miura, H. Hasegawa, M. Tsunoda, F. Matsukura and H. Ohno, App. Phys. Lett. 93, 082508, 2008.
15. M. Johnson, in Magnetoelectronics, edited by M. Johnson (Academic, New York, 2004.
16. P. Grünberg, R. Schreiber, Y. Pang, M.B. Brodsky, and H. Sower, Phys. Rev. Lett. 57, 2442, 1986

17. M. A. Ruderman, and C. Kittel, Phys. Rev. 96, 99-102, 1954.
18. T. Kasyua, Prog. Theor. Phys. 16, 45, 1956.
19. K. Yoshida, Phys. Rev. 106, 893, 1957.
20. B. D. Cullity and C. D. Graham, 2nd ed. John Wiley and Sons Ltd., Inc., Hoboken, New Jersey, 2009
21. S. Wurmehl, G. H. Fecher, H. C. Kandpal, V. Ksenofontov, and C. Felser , Phys. Lett. 88, 032503, 2005.
22. C. Kittel, Introduction to Solid State Physics, Wiley; 8th edition, 2005.
23. P. I. Good, and J. W. Hardin, Common Errors in Statistics (and How to Avoid Them), Wiley, 2009.
24. W. Gerlach, O. Stern, Z. Physik. 9, 349, 1922.
25. N. F. Mott and H. Jones, The Theory of the Properties of Metals and Alloys, The Oxford University Press, 1936.
26. N. F. Mott, Proc. R. Soc. 153, 699, 1936.
27. T. Valet, and A. Fert, Phys. Rev. B 48, 7099, 1993.
28. M. Karplus and R. N. Porter, Atoms and Molecules, The Benjamin / Cummings Publishing Company, 1970.
29. B. Whyte, IBM DeveloperWorks. (Retrieved July 25, 2014), 2009.
30. S. Dubois, L. Piraux, J. George, K. Ounadjela, J. Duvail and A. Fert, Phys. Rev. B 60, 477, 1999.
31. N. F. Mott, Adv. Phys. 13, 325, 1964
32. J. Bass and W. P. Pratt, J. Magn. Magn. Mater. 200(1-3), 274, 1999.
33. P. Holody, W. C. Chiang, R. Loloee, J. Bass,W. P. Pratt, and P. A. Schroeder, Phys. Rev. B 58, 12230, 1998.
34. W. H. Butler, X. G. Zhang, T. C. Schulthess, and J. M. MacLaren, Phys. Rev. B 63, 054416, 2001.

35. S. Yuasa, T. Nagahama, A. Fukushima, Y. Suzuki and K. Ando, Nat. Mat. 3, 868-871, 2004.

36. S. S. P. Parkin, C. Kaiser, A. Panchula, P. M. Rice, B. Hughes, M. Samant and S. H. Yang, Nat. Mat. 3, 862-867, 2004.

37. S. Yuasa, A. Fukushima, H. Kubota, Y. Suzuki, and K. Ando, Appl. Phys. Lett. 89, 042505, 2006.

38. S. Ikeda, J. Hayakawa, Y. Ashizawa, Y. M. Lee, K. Miura, H. Hasegawa, M. Tsunoda, F. Matsukura and H. Ohno, App. Phys. Lett. 93, 082508, 2008.

39. W. J. Gallagher and S. S. P. Parkin, IBM J. Res. Dev. 50, 5–23, 2006.

40. J. KÄubler, A. R. Williams and C. B. Sommers, Phys. Rev. B 28, 1745, 1983.

41. J. KÄubler, J. Phys. Condens. Mat. 18, 9795, 2006.

42. E. Sasioglu, L. M. Sandratskii, P. Bruno and I. Galanakis, Phys. Rev. B 72, 184415, 2005.

43. W. Nolting, Quantentheorie des Magnetismus, 1986.

44. M. N. Baibich, J. M. Broto, A. Fert, F. Nguyen van Dau, F. Petroff, P. Etienne, G. Creuzet, A. Friederich, and J. Chazelas, Phys. Rev. Lett. 61, 2472, 1988.

45. D. Pescia, D. Kerkmann, F. Schumann, and W. Gudat, Z. Phys. B 78, 475, 1990.

46. S.S.P. Parkin, N. More and K. P. Roche, Phys. Rev. Lett. 64, 2304, 1990.

47. I. Joffe and R. Heuberger, Phil. Mag. 314, 1051, 1974.

48. M. Walker, P. I. Mayo, K. O' Grady, S. W. Charles and R. W. Chantrell, J. Phys. : Condens. Matter 5, 2779, 1993.

49. S.S.P. Parkin, Phys. Rev. Lett. 67, 3598, 1991.

50. S. M. Thompson, J. Phys. D : Appl. Phys. 41, 093001, 2008.

51. S. Trudel, G. Oksana, H. Jaroslav, and H. Burkard, J. Phys. D: Appl. Phys. 43 (19), 193001, 2010.

52. F. Heusler, W. Starck and E. Haupt, Verh DPG 5, 220, 1903.

53. C. Felser and B. Hillebrands, J. Phys. D: Appl. Phys. 40, 2007.

54. Y. Nishino, M. Kato, S. Asano, K. Soda, M. Hayasaki, and U. Mizutani, Phys. Rev. Lett. 79, 1909, 1997.

55. J. H. Wernick, G. W. Hull, T. H. Geballe, J. E. Bernardini, J. V. Waszczak, Mater. Lett. 2, 90-92, 1983.

56. M. König, S. Wiedmann, C. Brüne, A. Roth, H. Buhmann, L. W. Molenkamp, X. L. Qi and S. C. Zhang, Science 318, 766-770, 2007.

57. T. M. Nakatani, T. Furubayashi and K. Hono, J. Appl. Phys. 109, 07B724-723, 2011.

58. H. Sukegawa, W. Wang, R. Shan, T. Nakatani , K. Inomata and K. Hono, Phys. Rev. B 79, 184418, 2009.

59. T. Graf, C. Felser and S. S. P. Parkin, Prog. Solid St. Chem. 39, 50, 2011.

60. S. Wurmehl, G. H. Fecher, H. C. Kandpal, V. Ksenofontov, C. Felser, H. J. Lin and J. Morais, Phys. Rev. B 72, 184434, 2005.

61. H. Huang, J. Tung, and G. Guo, Phys. Rev. B 91, 13, 2015.

62. R. de Groot, F. Mueller, P. van Engen and K. Buschow, Phys. Rev. Lett. 50, 2024, 1983.

63. R. J. Soulen Jr., J. M. Byers, M. S. Osofsky, B. Nadgorny, T. Ambrose, S. F. Cheng, P. R. Broussard, C. T. Tanaka, J. Nowak, J. S. Moodera, A. Barry and J. M. D. Coey, Science 282, 1998.

64. R. J. Soulen Jr., J. M. Byers, M. S. Osofsky, B. Nadgorny, T. Ambrose, S. F. Cheng, P. R. Broussard, C. T. Tanaka, J. Nowak, J. S. Moodera, A. Barry and J. M. D. Coey, J. Appl. Phys. 85, 8, 4589, 1999.

65. S. Ishida, T. Masaki, S. Fujii and S. Asano, Physica B: Con. Matt. 245, 1, 1998.

66. I. Galanakis, P. H. Dederichs and N. Papanikolaou, Phys. Rev. B 66, 174429, 2002.

67. B. Balke, G. H. Fecher, and C. Felser: Appl. Phys. Lett. 90, 242503, 2007.

68. J. C. Slater, J. Appl. Phys. 8, 385, 1937.

69. L. Pauling, Phys. Rev. 54, 899, 1938.

70. T. Kubota, S. Tsunegi, M. Oogane, S. Mizukami, T. Miyazaki, H. Naganuma and Y. Ando, Appl. Phys. Lett. 94, 122504-122503, 2009.

71. C. Felser and A. Hirohata, Heusler Alloys Properties, Growth, Applications, Cham : Springer, 2016.

72. A. Hirohata, M. Kikuchi, N. Tezuka, K. Inomata, J. S. Claydon, Y. B. Xu and G. van der Laan, Curr. Opin. Solid State Mater. Sci., 10, 93, 2006.

73. C. Felser and G. H. Fecher (Eds.), Spintronics: From Materials to Devices, Springer, Heidelberg, 2013.

74. T. Miyazaki and N. Tezuka, J. Magn. Magn. Mater. 139, 231–234, 1995.

75. J. S. Moodera, L. R. Kinder, T. M. Wong and R. Meservey, Phys. Rev. Lett. 74, 3273–3276, 1995.

76. M. Weisheit, S. Fähler, A. Marty, Y. Souche, C. Poinsignon, D. Givord, Science 315, 349, 2007.

77. T. Maruyama, Y. Shiota , T. Nozaki , K. Ohta, N. Toda, M. Mizuguchi, A. A. Tulapurkar, T. Shinjo, M. Shiraishi, S. Mizukami, Y. Ando and Y. Suzuki. Nat. Nano. 4, 158, 2009.

78. B. Balke, G. H. Fecher, H. C. Kandpal, C. Felser, K. Kobayashi, E. Ikenaga, J. J. Kim, and S. Ueda, Phys. Rev. B 74 104405, 2006.

79. Y. Miura, K. Nagao, M. Shirai, Phys. Rev. B 69, 144413, 2004.

80. B. Peters, A. Alfonsov, C. G. F. Blum, S. J. Hageman, P. M. Woodward, S. Wurmehl, B. Büchner and F. Y. Yang, Appl. Phys. Lett. 103, 162404, 2013.

81. M. Vahidi, J. A. Gifford, S. K. Zhang, S. Krishnamurthy, Z. G. Yu, L. Yu, M. Huang, C. Youngbull, T. Y. Chen and N. Newman, Appl. Phys. Lett. Mat. 2, 046108, 2014.

82. M. P. Raphael, B. Ravel, Q. Huang, M. A. Willard, S. F. Cheng, B. N. Das, R. M. Stroud, K. M. Bussmann, J. H. Claassen, and V. G. Harris, Phys. Rev. B 66, 10, 2002.

83. P. J. Brown, K. U. Neumann, P. J. Webster, and K. R. A. Ziebeck, J. Phys. Condens. Matter. 12, 8, 1827, 2000.

84. V. Ksenofontov, S. Wurmehl, S. Reiman, G. Jakob and C. Felser, arXiv preprint cond-mat/0610480, 2006.

85. H. C. Kandpal, G. H. Fecher and C. Felser, J. Phys. D: Appl. Phys. 40, 1507, 2007.

86. W. H. Wang, H. Sukegawa, R. Shan, T. Furubayashi and K. Inomata, Appl. Phys. Lett. 92, 221912, 2008.

87. M. Tsunoda, K. Imakita, M. Naka and M. Takahashi, J. Magn. Magn. Mater. 304 55, 2006.

88. H. C. Kandpal, G. H. Fecher, C. Felser and G. Schönhense., Phys. Rev. B 73, 094422, 2006.

89. W. Kohn, Rev. Mod. Phys. 71, 1253-1266, 1999.

90. G. N. Li, Y. J. Jin, and J. I. Lee, Chin. Phys. B 19, 097102, 2010.

91. W. Wang, H. Sukegawa, R. Shan, and K. Inomata, Appl. Phys. Lett. 93, 182504, 2008.

92. C. Sterwerf, S. Paul, B. Khodadadi and G. Reiss, J. Appl. Phys. 120, 8,

2016.

93. N. Tezuka, N. Ikeda, F. Mitsuhashi, and S. Sugimoto, Appl. Phys. Lett. 94, 162504 (2009)

94. http://edwgrochowski.com/bio.html

95. M. Takagishi, K. Yamada, H. Iwasaki, H. N. Fuke, and S. Hashimoto, IEEE Trans. Magn. 46, 2086, 2010.

96. T. M. Nakatani, T. Furubayashi, S. Kasai, H. Sukegawa, Y. K. Takahashi, S. Mitani, and K. Hono, Appl. Phys. Lett. 96, 212501, 2010.

97. B. M. Chen, T. H. Lee, and V. Venkataramanan, Hard Disk Drive Servo Systems, Springer London, 2013.

98. B. Hoefflinger, Chips 2020: A Guide to the Future of Nanoelectronics. Springer, 2012.

99. M. Joodaki, Selected Advances in Nanoelectronic Devices. Springer, 2012.

100. A. Hirohata and K. Takanashi, J. Phys. D: Appl. Phys. 47, 193001, 2014.

101. Hiroki Koike, Sadahiko Miura, Hiroaki Honjo, Toshinari Watanabe, Hideo Sato, Soshi Sato, Takashi Nasuno, Yasuo Noguchi, Mitsuo Yasuhira, Takaho Tanigawa, Masakazu Muraguchi, Masaaki Niwa, Kenchi Ito, Shoji Ikeda, Hideo Ohno, and Tetsuo Endoh, 2016 IEEE 8th International Memory Workshop, 2016.

102. K. Seshan, Handbook of thin film deposition, 1st ed. Waltham [Mass.]: William Andrew, 2012.

103. M. Ohring, The Material Science of Thin Films, Academic Press, 1992.

104. D. S. Misra and S. B. Palmer, Physica C 176(1-3): 43-48, 1991.

105. W. R. Grove, Philos. Trans. R. Soc. London A 142, 87, 1852.

106. J. L. Vossen and J. J. Cuomo, Thin Film Process, Academic Press Chapt. II-3, 1978.

107. T. Sonoda, M. Ito, M. Kobiki, K. Hayashi, S. Takamiya and S. Mitsui, K. Kondo, J. Saito, et al., J. Cryst. Growth 95, 317, 1989.

108. M. Vopsaroiu, G. Vallejo Fernandez, M. J. Thwaites, J. Anguita, P. J. Grundy and K. O'Grady, J. Phys. D: Appl. Phys. 38, 490-496, 2005.

109. M. Vopsaroiu, M. Thwaites, S. Rand, P. Grundy and K. O'Grady, IEEE Trans. Mag. 40, 4, 2443-2445, 2004.

110. B. A. Joyce, Contemporary Physics 31, 195-197, 1990.

111. G. Dhanaraj, K. Byrappa, V. Prasad and M. Dudley, Springer Handbook of Crystal Growth, 1st ed. Berlin, Heidelberg: Springer Berlin Heidelberg, 2010.

112. N. Tezuka, N. Ikedam, A. Miyazaki, S. Sugimoto, M. Kikuchi, and K. Inomata, Appl. Phys. Lett. 89, 112514, 2006.

113. L. R. Fleet, G. Cheglakov, K. Yoshida, V. K. Lazarov, T. Nakayama and A. Hirohata, J. Phys. D: Appl. Phys. 45, 032001, 2012.

114. M. Oogane, R. Yilgin, M. Shinano, S. Yakata, Y. Sakuraba, Y. Ando, and T. Miyazaki, J. Appl. Phys. 101, 09J501-503, 2007.

115. G. Binning, C. F. Quate and C. Gerber, Phys. Rev. Lett. 56, 930, 1986.

116. Y. Martin and H. K. Wickramsinghe, Appl. Phys. Lett. 50, 1455, 1987.

117. T. C. Schulthess and W. H. Butler, Phys. Rev. Lett. 81, 4516, 1998.

118. J. H. Neave, B. A. Joyce, P. J. Dobson and N. Norton, Appl. Phys. A 31: 1. 1983.

119. W. C. Röntgen, Mc. Clure Magazine, 1896.

120. W. Friedrich, P. Knipping and M. V. Laue, Mathematisch–physikalische Klasse, 303-322, 1912.
121. Rigaku Automated Multipurpose X-ray Diffractometer Instruction Manual.
122. K. Nagao and E. Kagami, X-ray thin film measurement techniques VII. Pole figure measurement, The Rigaku Journal, 27, 2, 2011.
123. L. de Broglie, Annales de Physique 3, 22, 1925
124. M. Knoll and E. Z. Ruska, Physik 78, 318. 1932.
125. D. B. Williams and C. B Carter, Transmission Electron Microscopy, 2016.
126. T. Saito, T. Katayama, T. Ishikawa, M. Yamamoto, D. Asakura, T. Koide, Y. Miura, and M. Shirai, Phys. Rev. B 81, 144417, 2010.
127. S. Foner, Rev. of Scientific Instru. 27, 548-548, 1956.
128. K. O'Grady, L. E. Fernandez-Outon, G. Vallejo-Fernandez, J. Magn. Magn. Mater, 322, 883-899, 2010.
129. E. Fulcomer, S. H. Charap, J. Appl. Phys., 43, 4190, 1972.
130. E. Fulcomer, S. H. Charap, J. Appl. Phys., 43, 4184, 1972.
131. J. Sagar, C. Yu, C. Pelter, J. Wood, L. Lari, A. Hirohata and K. O'Grady, IEEE Trans. Magn., 48, 11, 4006-4009, 2012.
132. J. Sagar, L. R. Fleet, A. Hirohata, K. O'Grady, IEEE. Trans. Magn., 47, 2440-2443, 2011.
133. J. A. Floro, S. J. Hearne, J. A. Hunter, P. Kotula, E. Chason, S. C. Seel and C. V. Thompson, J. Appl. Phys., 89, 4886-4897, 2001
134. E. Wolf, Nanophysics and nanotechnology, 3rd ed., Wiley-VCH, 2015.
135. M. Oogane , R. Yilgin , M. Shinano , S. Yakata , Y. Sakuraba , Y. Ando , and T. Miyazaki , J. Appl. Phys., 101, 09J501, 2007.

136. H. Kijima, T. Ishikawa, T. Marukame, H. Koyama, K. Matsuda, T. Uemura, and M. Yamamoto, IEEE Trans. Magn. 42, 2688, 2006.

137. A. Hirohata and K. Takanashi, J. Phys. D: Appl. Phys. 47, 193001 (2014).

138. L. M. Loong, J. H. Kwon, P. Deorani, C. N. T. Yu, A. Hirohata and H. Yang, Appl. Phys. Lett., 104, 232409, 2014.

139. W. H. Meiklejohn, J. Appl. Phys. 33, 1328, 1962.

140. R. Singh, B. Ingale, L. Varga, V. Khovaylo, S. Taskaev, and R. Chatterjee, J. Magn. Magn. Mater. 394, 143, 2015.

141. A. Hirohata, K. Izumida, S. Ishizawa, J. Sagar, and T. Nakayama, J. Appl. Phys. 115, 17D725, 2014.

142. C. A. Culbert and W. H. Butler, J. Appl. Phys. 103, 07D707, 2008.

143. T. Furubayashi, K. Kodama, H. Goripati, Y. Takahashi, K. Inomata and K. Hono, J. Appl. Phys. 105, 07C305, 2009.

144. M. Bass, Handbook of Optics II, New York: McGraw-Hill, 1995.

145. G. V. Samsonov, Handbook of the Physicochemical Properties of the Elements, New York: IFI/Plenum, 1968.

146. J. Sagar, C. N. T. Yu, L. Lari and A. Hirohata, J. Phys. D: Appl. Phys. 47, 265002, 2014.

147. A. Hirohata, H. Kurebayashi, S. Okamura, M. Kikuchi, T. Masaki, T. Nozaki and K. Inomata, J. Appl. Phys. 97, 103714, 2005.

148. G. Wastlbauer and J. A. C. Bland, Adv. Phys. 54, 137, 2005.